Fatigue Crack Growth Behaviour of Nitrogen Bearing Austenitic Stainless Steel and its Weld: Analysis using Unified Approach

By

MATCHA NANI BABU

Enrolment No. : ENGG02201504004

Indira Gandhi Centre for Atomic Research, Kalpakkam

A thesis submitted to the

Board of Studies in Engineering Sciences

In partial fulfillment of requirements

for the Degree of

DOCTOR OF PHILOSOPHY

of

HOMI BHABHA NATIONAL INSTITUTE

OCTOBER, 2019

Homi Bhabha National Institute[1]

Recommendations of the Viva Voce Committee

As members of the Viva Voce Committee, we certify that we have read the dissertation prepared by **Matcha Nani Babu** entitled " ***Fatigue Crack Growth Behaviour of Nitrogen Bearing Austenitic Stainless Steel and its Weld: Analysis using Unified Approach*** " and recommend that it may be accepted as fulfilling the thesis requirement for the award of Degree of Doctor of Philosophy.

	Signature with date
Chairman - **Dr. S. Murugan**	S. Murugan 17.12.2020
Guide / Convener - **Dr. G. Sasikala**	Sasikala 17.12.2020
Co-guide - (if any) : N/A	
Examiner - **Dr. S. Tarafder**	S Tarafder 17 Dec 2020
Member 1- **Dr. C. K. Mukhopadhyay**	17 Dec 2020
Member 2- **Dr. V. S. Srinivasan**	V.S. Srinivasan 17/12/2020
Member 3- **Dr. Raghu V Prakash**	Raghu Prakash 17 Dec 2020

Final approval and acceptance of this thesis is contingent upon the candidate's submission of the final copies of the thesis to HBNI.

I/We hereby certify that I/we have read this thesis prepared under my/our direction and recommend that it may be accepted as fulfilling the thesis requirement.

Date: 17-12-2020

Place: IGCAR-Kalpakkam

17.12.2020

Signature

Guide

[1] This page is to be included only for final submission after successful completion of viva voce.

SUMMARY

Fatigue crack growth (FCG) properties of SS 316L(N), a major structural material for nuclear, chemical, automobile and cryogenic industries are required for damage tolerant design and integrity assessment of components subjected to cyclic loading during service. Extensive studies in literature show that these properties are influenced by test conditions (such as temperature, load ratio, frequency, environment etc) and material conditions (such as cold work and residual stresses in forming and welding, and ageing in service). Also, it is observed that growth of short cracks cannot be predicted using data obtained from long cracks. ***There are two fundamental issues yet to be resolved (1) effect of load ratio on fatigue crack growth and (2) the reason for higher crack growth rate for short cracks when compared to long crack. Attempts have been made in this thesis to address these two fundamental issues through characterizing the FCG behaviour of SS316LN base, weld and cold worked material.*** In the process, effect of nitrogen content, test temperature and frequency on the FCG behaviour has been examined.

FCG behavior of SS316L as a function of nitrogen has been evaluated incorporating the crack closure effects at ambient and elevated temperatures. The results obtained from constant K_{max} test, i.e., in closure free condition differ from those incorporating the crack closure effects. The improved FCG resistance in the intermediate temperatures manifested as a plateau or increase in the effective threshold with temperature and overlapping of FCG curves in the range 623 - 773 K is attributed to dynamic strain ageing (DSA). The activation energy values 90± 2 kJ/mol (623-723 K) which is corresponding to the activation energy for the carbon diffusion, and 160±5 kJ/mol (773-823 K) for nitrogen diffusion determined from the temperature-dependence of FCG properties indicate that the diffusion of interstitial solute elements is responsible for the DSA. The dormancy of crack at low frequency and at high temperature is associated with blunting of crack tip due to creep and/or oxidation and not because of crack closure.

Further analyses were carried out using the Unified Approach to provide a physically more meaningful and self-consistent approach to address a) the load ratio effects, b) the short crack problem and c) role of residual stresses due to welding and cold working. The role of nitrogen in FCG behaviour has been examined considering three concentrations in this study. FCG rates as a function of *R*-ratio were determined. The results were analyzed using the two-parametric approach involving ΔK and K_{max} parameters. Crack growth trajectory maps were constructed, and the effect of nitrogen on the crack growth trajectory has been established in this study. It is shown that deformation-induced martensitic transformation (DIMT) is the K_{max} dependent process that mainly causes the deviation of the crack growth trajectory from the pure fatigue line (45^{o} line). The increased crack growth resistance in these alloys is due to transformation toughening. The presence of DIMT was confirmed by Magnetic Atomic Force Microscope (MAFM). The contribution from the compressive residual stresses in welds is demonstrated to be more dominant at low *R*-values than at high *R*-values. It is shown that the Unified Approach provides a self-consistent analysis of the role of residual stresses introduced during welding. The results of cold worked material show that the increase in the cold work improved the FCG resistance though deformation induced martensite transformation up to 10 % cold work, beyond which there is no further improvement.

On the basis of Griffith's equation or Orowan equation, the shorter the crack, the higher are the stresses needed for its growth. The short crack growth data in literature, however, appears to grow at smaller ΔK than that found for long cracks. Hence, similitude break down was proposed for short cracks. Extensive literature on fatigue damage analysis in the endurance limit indicate that the large numbers of cycles at these levels lead to formation of intrusions and extrusions, dislocation slip bands, dislocation pile-ups, and deformation bands which contribute to local internal stresses with stress-gradients. The incipient cracks form in the presence of these internal stresses which are augmented by the remote applied stresses. Fracture mechanics does not take these internal stresses explicitly into consideration in computing actual crack tip driving forces. Recognising this, a modified Kitagawa diagram was developed that connects the short crack growth behavior with that of long crack growth by considering these internal stresses. The Unified Approach provides a simple methodology to compute the required minimum internal stresses needed in addition to the applied stresses for the short cracks to grow. This approach is adopted to describe the differences in growth behaviour of short cracks and long cracks in SS316L(N) to show that there is no need to invoke similitude breakdown if one considers the total crack tip driving force that includes applied and internal stresses. The modified Kitagawa-Takahashi diagram was also used to evaluate the contribution of environment-induced chemical driving forces to the crack tip stress fields.

CONTENTS

Title		Page No
	SUMMARY	ix
	LIST OF FIGURES	xvii
	LIST OF TABLES	xxiv
	NOMENCLATURE	xxv
CHAPTER 1: INTRODUCTION		**1**
1.0	Introduction	1
2.0	Objectives of the Work	5
3.0	Layout of the Thesis	6
CHAPTER 2: LITERATURE SURVEY		**7**
2.0	Introduction	7
2.1	Fracture mechanics approach to fatigue crack growth	7
2.2	Fatigue Crack Growth Curve	9
	2.2.1 Threshold Regime –I	10
	2.2.2 Intermediate Region of Crack Growth (Regime II)	11
	2.2.3 High growth rate regime (Regime III)	13
2.3	Crack closure	14
	2.3.1 Plasticity induced crack closure	14
	2.3.2 Oxide induced crack closure	15
	2.3.3 Phase transformation induced crack closure	16
	2.3.4 Roughness-induced crack closure	16
2.4	High-temperature fatigue crack growth	18
2.5	Fatigue crack growth studies in Austenitic stainless steels	20
2.6	Effects of Nitrogen on Mechanical behavior of Austenitic stainless steels	22
	2.6.1 Role of nitrogen in the Austenitic Stainless Steels	22

2.6.2 Deformation induced martensite formation in Austenitic Stainless steels 24
2.6.3 Effects of nitrogen on the mechanical properties of Austenitic Stainless steels 25
2.6.4 Effects of nitrogen on Fatigue crack growth in Austenitic Stainless steels 26
2.7 Effect of cold work 31
2.8 Fatigue Crack growth behaviour of stainless steel welds 32
2.9 Short crack growth behaviour 34
2.9.1 Classification of short cracks 35
2.9.2 Similitude breakdown 36
2.10 Fundamental problems associated with the conventional fatigue crack growth analysis 36
2.11 Two-parameter approach to Fatigue crack growth 38
2.12 Scope of the work 38

CHAPTER 3: EXPERIMENTAL DETAILS 39
3.0 Introduction 39
3.1 Materials and specimen preparation 39
3.1.1 Materials 39
3.2 Sample fabrication 44
3.2.1 Base material specimens 44
3.2.2 Weld material specimens 45
3.3 Crack growth measurement 46
3.4 Fatigue Pre-Cracking 51
3.5 Fatigue crack growth testing 52
3.6 Crack closure measurement 54
3.7 Optical measurement of crack size 56
3.8 Characterization techniques used 57
3.8.1 Optical Microscopy 57
3.8.2 Scanning Electron Microscopy 58
3.8.3 X-Ray diffraction technique (XRD) 58

3.8.4 Transmission electron Microscopy 59
3.8.5 Magnetic measurement 59
3.8.6 Residual stress measurement 59
3.9 Short fatigue crack growth measurement 60

CHAPTER 4: EFFECT OF TEMPERATURE ON THE FCG BEHAVIOUR OF SS316L(N) 62
4.1 Introduction 62
4.2 Fatigue Crack Growth Studies of SS316LN at room temperature 62
4.3 Fatigue Crack Growth Studies of SS316LN at high temperature 68
4.3.1 The Paris regime 68
4.3.2 The threshold regime 74
4.4 Change in crack closure mechanisms with temperature 80
4.5 Effect of Dynamic strain ageing on FCG 82
4.5.1 Effect of dynamic strain ageing on fatigue damage 83
4.5.2 Mechanism of dynamic strain ageing 86
4.6 Effect of test frequency on the fatigue crack growth 88
4.7 Conclusions 93

CHAPTER 5 : ROLE OF NITROGEN ON THE FATIGUE CRACK GROWTH BEHAVIOR OF AUSTENITIC STAINLESS STEELS AND ANALYSIS USING UNIFIED APPROACH 95
5.0 Introduction 95
5.1 Background 95
5.2 Effects of Load Ratio on the FCG behavior 101
5.2.1 The Two-parametric Approach for FCG Analysis 102
5.2.2 Estimation of Crack Tip Driving Forces 104
5.3 Fatigue crack growth analysis of SS316LN using unified approach 107
5.4 Analysis of FCG data for other Austenitic Stainless Steels: 117
5.5 Comparison with other Published data on 316 Stainless Steels 120
5.6 Microstructural analysis 122
5.7 Conclusions 128

CHAPTER 6 : FATIGUE CRACK GROWTH BEHAVIOUR OF SS316(N) WELD AND COLD WORKED SS316L(N) – ANALYSIS USING THE UNIFIED APPROACH **130**

6.0 Introduction 130

6.1 Back ground 130

6.2 Fatigue crack growth behaviour of SS 316 (N) weld 131

6.2.1 Hardness Measurement 132

6.2.2 Fatigue crack growth behaviour of SS316(N) weld 133

6.3 Analysis of Crack Growth Rates using the Two-parametric Approach 135

6.3.1 The application of L-shaped curves for Friction Stir Welds in Al-alloys 137

6.3.2 Two-parametric representation of the FCG in the SS316 (N) weld metal 138

6.4 Two-parametric representation of the FCG in other weld materials 142

6.4.1 Low carbon steels 143

6.4.2 Aluminum alloys 144

6.4.2.1 5083 H32 Alloy 144

6.4.2.2 6061-T651 Alloy 146

6.4.2.3 Al-Li Alloy 2195-T8 147

6.4.3 25Cr2Ni2MoV steel 148

6.5 Effect of cold work on the fatigue crack growth behaviour of SS316LN steel 151

6.6 Conclusions 155

CHAPTER 7 : MODIFIED KITAGAWA-TAKAHASHI DIAGRAM FOR SHORT CRACK GROWTH AND ENVIRONMENTAL EFFECTS **157**

7.0 Introduction 157

7.1 Background 157

7.1.1 The Kitagawa-Takahashi Diagram 157

7.1.2 Short crack behaviour 158

7.2 Growth behaviour of long fatigue cracks in air and vacuum 161
7.3 Short and Long fatigue crack growth measurement in vacuum chamber of SEM 166
7.4 Fatigue crack growth analysis of short crack and long crack in vacuum 167
7.5 Short crack initiation mechanism 175
7.6 Conclusions 178

CHAPTER 8: SUMMARY AND SCOPE FOR FUTURE WORK 179
8.1 Summary 179
8.2 Future Work 183

REFERENCES 185

LIST OF FIGURES

Figure 1.1	Different damage modes in PFBR components [7]	3
Figure 2.1	A sinusoidal cyclic loading pattern with the load parameters	9
Figure 2.2	Schematic presentation of fatigue crack growth curve	10
Figure 2.3	Shear slide model for formation of striations on the fracture surface [52]	13
Figure 2.4	Schematic presentation of crack closure correction for effective crack tip driving force	18
Figure 3.1	Microstructure of all three nitrogen variants (a) 8N, (b) 14N and (c) 22N	40
Figure 3.2	Schematic drawing of tensile specimen	41
Figure 3.3	Schematic view of weld pad along with CT blank embedded	42
Figure 3.4	Image of Weld metal shows the different layers of weld beads	43
Figure 3.5	General compact tension (CT) sample drawing for FCG tests	45
Figure 3.6	Schematic of CT specimen with DCPD leads	46
Figure 3.7	Correlation between crack lengths normalized by CT sample dimension W and	50
Figure 3.8	Resonance based pre-cracker and FCG test system.	52
Figure 3.9	(a) Servo-Hydraulic FCG test system with (b) high temperature COD slot	54
Figure 3.10	High temperature COD gage mounted on to CT sample	54
Figure 3.11	(a) Schematic presentation of the load cycle indicating the different parameters, (b) Load – Displacement data for crack closure load measurement	55
Figure 3.12	(a) Travel stereo microscope (b) Macro view of the fracture surface showing different regions of crack extension	56

Figure 3.13	Hole drilling methods employed on the CT sample made from weld	60
Figure 3.14	Mechanical stage for FCG test attached to SEM for in situ observation of crack growth	61
Figure 4.1	FCG behaviour of SS316LN without and with crack closure correction	65
Figure 4.2	Effect of Kmax on the FCG behaviour of SS316L(N) in ΔK decreasing test. The solid symbols are the data from constant R (= 0.1), in which both K_{min} and K_{max} decrease as the test progresses. The open symbols are for K_{max} constant test in which K_{min} and R increase as the test progresses.	67
Figure 4.3	Effect of test temperature on the FCG behaviour of SS316L(N)-8N without crack closure correction	69
Figure 4.4	Effect of test temperature on the FCG behaviour of SS316LN (8N) after crack closure correction	69
Figure 4.5	Effect of temperature on the Paris parameters for SS 316LN (8N)	71
Figure 4.6	Effect of test temperature on the FCG behaviour of SS316LN after normalization with Young's modulus.	73
Figure 4.7	Effect of test temperature on the FCG behaviour of SS316LN after normalization with yield strength	73
Figure 4.8	FCG results of SS 316LN-8N at different temperatures in the range 300-823 K	74
Figure 4.9	FCG results of SS 316LN-8N after crack closure correction at different temperatures in the range 300-823 K.	75
Figure 4.10	FCG thresholds at different temperatures	76
Figure 4.11	FCG results of SS 316LN-8N, (a) ΔK, (b) ΔK_{eff} normalized with yield strength in the temperature range 300-823 K	79
Figure 4.12	FCG thresholds normalized with yield strength at different temperatures	80

Figure 4.13	Crack path deviations with temperature (a) 300 K, (b) 623 K and (c) 823 K	81
Figure 4.14	Schematic diagram of plastic strain (ε_p) response during stress control fatigue test for the low ($\varepsilon_{p,low}$) and high ($\varepsilon_{p,high}$) work hardening material.	85
Figure 4.15	Arhenius plot of crack tip strain rate for the temperature range 623 - 823 K corresponding to ΔK at which DSA vanishes	88
Figure 4.16	FCG behaviour of SS316LN-8N at 75Hz and different temperatures	90
Figure 4.17	Effect of frequency on the threshold behaviour of SS316LN-8N different temperatures frequency 75 Hz in the figure	91
Figure 4.18	Comparison of FCG behaviour of SS316LN-8N at 673 K and different frequencies.	92
Figure 5.1	Effect of nitrogen on fatigue crack growth resistance of SS 316LN at room temperature	96
Figure 5.2	Effect of nitrogen on fatigue crack growth resistance for 304L and 304LN at RT and 77K.	99
Figure 5.3	Comparison of FCG resistance for 304 and 316 austenitic stainless steels.	100
Figure 5.4	Schematic procedure to arrive at the two Crack-tip driving forces. a) FCG curves as a function of the R-ratio. b) ΔK-R bilinear curves for selected crack growth rates. c) The L-shaped ΔK-K_{max} curves generated using data extracted from figure b), for the selected crack growth rates. The L-shaped curves define the limiting values ΔK^* and K_{max}^* at each crack growth rate. d) Fatigue crack growth trajectory path depicting the material resistance to crack growth.	104
Figure 5.5	Fatigue crack growth rates of 8N alloy at various R-ratios as a function of a) ΔK and b) K_{max}.	108

Figure 5.6	a) ΔK vs R for selected crack growth rates for 8N alloy showing a bilinear behavior. b) ΔK vs K_{max} curves for selected crack growth rates. The L-shaped behavior is shown with limiting values in terms of ΔK and K_{max} for each crack growth rate.	109
Figure 5.7	Crack growth trajectory map for 8N alloy, in terms of the limiting values ΔK^* and K_{max} * for increasing crack growth rates.	110
Figure 5.8	Crack growth rates for 14N alloy for various R values in terms of a) ΔK and b) K_{max}.	110
Figure 5.9	a) ΔK-R curves and b) ΔK -K_{max} curves for the N14 alloy for selected crack growth rates. Limiting Values ΔK^* and Kmax* for each crack growth rate are shown. c) ΔK - K_{max} curves for the N14 alloy at higher crack growth rates. d) Crack growth trajectory map for the N14 alloy.	112
Figure 5.10	Crack growth rates for the 22N alloy for various R values in terms of	113
Figure 5.11	ΔK-R plots for 22N alloy. Within the limited data, the figure shows that ΔK levels	114
Figure 5.12	ΔK-K_{max} curves for the 22N alloy a) at low crack growth rates and b) at higher crack growth rates.	114
Figure 5.13	Crack growth trajectory map for the 22N alloy.	115
Figure 5.14	Crack growth trajectory maps for different nitrogen 316L stainless steels. The Kmax dependent processes including DIMT make the trajectory to deviate from the pure fatigue line.	116
Figure 5.15	Crack growth rates in 304 Stainless steels as function of Kmax, reported by Mei and Morris [142, 143].	116
Figure 5.16	Plots of ΔK - R bilinear curves for selected (a) low and (b) high crack growth rates from Fig. 15. Bilinear curves are drawn through the limited data by extrapolation to high R values and a constant ΔK value at $R \geq 0.7$.	118

Figure 5.17 a) ΔK-K_{max} curves for 304L alloy at some selected crack growth rates, b) crack growth trajectory path for the alloy at 77 K, using Mei & Morris data. 119

Figure 5.18 Comparison of trajectory maps of 8N, 14N and 22N, 316L alloys with that of 304L at 77 K where transformation induced toughening is known to occur. 119

Figure 5.19 Comparison of present 316 SS data with those of Vogt et al., but tested at 77 K [148]. 14N, and 22N 121

Figure 5.20 Grain size distributions in the three-nitrogen containing 316L stainless steels. 122

Figure 5.21 a) Fracture surfaces of 8N (left) and 14N (right) alloys. Crack growth from top to bottom. b) Fracture surfaces of 22N Steel. Crack growth direction is from top to bottom (high crack growth rate da/dN > 10-6 mm/cycle). 124

Figure 5.22 TEM images of FCG tested samples –(a) 8N (b) 14N and (c) 22N. 125

Figure 5.23 Typical magnetic domains obtained using MAFM for (a) 8N, (b) 14N, (c) 22N, all corresponds to ΔK of 15 MPa.m0.5. Fig. d corresponds to ΔK ~ 5 MPa.m0.5 and the domain sizes are small, and the densities are similar for all the three alloys. 126

Figure 5.24 The fraction of the martensite colonies observed as a function of the distance from the crack tip for ΔK ~ 5.5 and 15 MPa.m$^{0.5}$. 127

Figure 6.1 Hardness profile across the weld 133

Figure 6.2 (a) Crack growth rate as functions of (a) ΔK, (b) K_{max} and (c) comparison of base and weld metal at low and high R values 134

Figure 6.3 (a-c) Effect of compressive residuals stresses on the amplitude, $\Delta\sigma$ and maximum stress σ_{max} and their effects on fatigue crack growth rate. a) and b) correspond to crack length constant during the three cycles shown. 135

Figure 6.4	Effect of residual stresses on the ΔK-K_{max} threshold curve in 2024 and 6013 alloys from 'John et al. 2003 [161]	138
Figure 6.5	ΔK-R curves at low (a) and high (c) crack growth rate with the corresponding ΔK - K_{max} curves (b) and (d) respectively	140
Figure 6.6	(a) Crack growth trajectory (ΔK^*-K_{max}^*) at low and high da/dN values (b) comparison of trajectories of base and weld metals, (c) ΔK_{res} in the weld metal as a function of crack growth rate	142
Figure 6.7	(a) Hardness of weld strip in comparison to base metal of A36 (b) crack growth rate at low R (=0.05) in the base steel (A36) and two weld materials A5.18 and A5.28 [227]	144
Figure 6.8	(a) FCG behaviour of 5083 H32 Al alloy at low and high R-values of base and FSW weld metals (b) Crack growth trajectories (c) ΔK_{res} contribution to the crack growth resistance [161]	145
Figure 6.9	(a) Crack growth results of 6061-T651 Al alloy base and FSW metal at R-values of 0.1 and 0.8, (b) Crack growth trajectory	147
Figure 6.10	(a) FCG results at R= 0.1 for base and 8 mm thick FSW weld of Al-Li alloy with different weld sizes, (b) the variation of ΔK_{res} with crack growth rate and weld size [229]	148
Figure 6.11	(a) Crack growth rate (b) ΔK-R, (c) ΔK-K_{max} of 25Cr2Ni2MoV steel base metal	149
Figure 6.12	(a) Crack growth rate (b) ΔK-R, (c) ΔK-K_{max} of 25Cr2Ni2MoV steel weld metal [225, 231]	150
Figure 6.13	Crack growth trajectories of 25Cr2Ni2MoV steel extracted from Figs.6.11 and 6.12	150
Figure 6.14	FCG results at room temperature for SS316L(N) (14N) (a) 5% (b) 10% and (c) 15% cold worked material at different load ratios	151
Figure 6.15	L-Shape curved SS316L(N) (14N) for (a) 5% (b) 10% and (c) 15% cold worked material at room temperature.	153

Figure 6.16	Crack growth trajectories of SS316LN (14N) for different cold worked conditions	153
Figure 6.17	XRD results reveal the presence of deformation inducedmartensite	154
Figure 7.1	Kitagawa-Takahashi diagram [232] for different materials as presented in [234]	158
Figure 7.2	FCG results of SS304 in vacuum and air	162
Figure 7.3	Environment contribution on FCG resistance of SS304. This includes any secondary contribution due to DIMT	163
Figure 7.4	FCG results of SS316 in vacuum and air environment	164
Figure 7.5	Environment contribution on FCG resistance of SS316LN. This includes any secondary contribution due to DIMT.	165
Figure 7.6	Comparison of the effects of environment on the crack growth resistance for SS304, SS316 and SS316LN	166
Figure 7.7	Crack growth as a function of number of cycles for short and long cracks in vacuum.	168
Figure 7.8	Crack growth rate as a Kmaxfor the long and short crack in vacuum	169
Figure 7.9	The variation in the internal stress profile as a function of crack length	173
Figure 7.10	Modified Kitagawa-Takahashi diagram connects the short and long crack growth behaviour and the behavior of a smooth specimen.	175
Figure 7.11	(a) Short crack nucleation & growth (b) Long crack growth after pre-cracking	177
Figure 7.12	Formation of deformation-induced martensite ahead of short crack as marked	177

LIST OF TABLES

Table 2.1	Chemical composition of different N alloyed stainless steels	29
Table 3.1	Chemical composition of different N alloyed 316L stainless steels	40
Table 3.2	Tensile properties of SS 316L of different nitrogen levels	41
Table 3.3	Details of the preparation of weld pads	43
Table 3.4	Chemical composition (wt%) of the base and weld metals	43
Table 3.5	Yield strength and UTS of SS316 (N) weld of 8N	43
Table 3.6	Variation of V/Vr with a/W for different constant currents and temperatures	49
Table 4.1	Paris parameters at different temperatures for 8N steel using ΔK and ΔK_{eff} for correlating	70
Table 4.2	Tensile properties of SS 316L(N) at different temperatures	71
Table 4.3	Transition point in the FCG curve at different temperatures	87

CHAPTER 1: INTRODUCTION

1.0 Introduction

Austenitic Stainless steels are an important class of alloys. Their importance is apparent in different applications such as from low-end applications, like utensils and furniture, to very sophisticated industrial equipment and body implants. Hence, the use of stainless steels is indispensable. In fact, the omnipresence of stainless steels in our daily life makes it impossible to enumerate their applications [1]. Several types of stainless steels are available for different applications. One of the important classes of these AISI type 316 stainless steel (SS316) that is used worldwide for high temperature structural applications in chemical, biological, agriculture, defence, aerospace and nuclear industries. These steels possess a combination of adequate high-temperature mechanical properties, corrosion resistance and ease of fabrication due to good weldability. However, these steels are prone to sensitization when exposed to temperatures in the range from 673 to 1073 K. This is due to precipitation of chromium rich carbides, preferentially along the grain boundaries causing local depletion of Cr to levels much lower than the 11.5mass%[2,3] that is required to make the steel corrosion resistant. The thermal cycles experienced by the material, while welding leads to sensitization. The welded components when stored in coastal environment undergo intergranular stress corrosion cracking (IGSCC) in presence of residual stresses due to the welding and chloride environment.

To minimize this problem, low-carbon (< 0.03 mass%) versions of this steel (SS316L) have been developed, so that the carbide precipitation and the consequent removal of Cr from solid solution are reduced. However, reduction in Content leads to loss of strength, and N additions have been recommended leading to the development of SS316LN to compensate for the carbon stringing effect [4]. SS 316LN is used worldwide in the nuclear industry as a high-temperature structural material for fast breeder reactors due to the combination of good high-temperature mechanical properties, compatibility with coolant liquid sodium, good weldability, and resistance to intergranular stress corrosion cracking (IGSCC). Nitrogen, while improving the solid solution strengthening, also a) stabilizes the austenite phase b) causes grain-refinement thereby contributing to additional strengthening, and c) leads to increased toughness via strain-hardening. It also improves the resistance to corrosion like pitting, crevice corrosion, and intergranular stress-corrosion by inhibiting the carbide formation near the grain boundaries. Hence, nitrogen is considered as one of the essential elements for industrial applications of austenitic stainless steels [5].

Based on the international experience and in house R&D, it has been chosen for the high-temperature structural components of the 500 MWe, prototype fast breeder reactor (PFBR), which is in an advanced stage of commissioning at Kalpakkam [6]. A schematic of the PFBR is given in Fig. 1.1[7], with the SS316L(N) components marked. Many of these components are subjected to cyclic thermo-mechanical loading, which induces different kinds of damage like creep [8], fatigue [9], creep-fatigue interaction [10], etc. The flow-induced vibrations and thermal fluctuations can cause high cycle fatigue and thermo-mechanical fatigue damage within the frequency range 0.5 to 100 Hz [11]. Hence, for the defect tolerant design and integrity assessment of the components, in addition to creep, fatigue and fracture toughness data, FCG data is required.

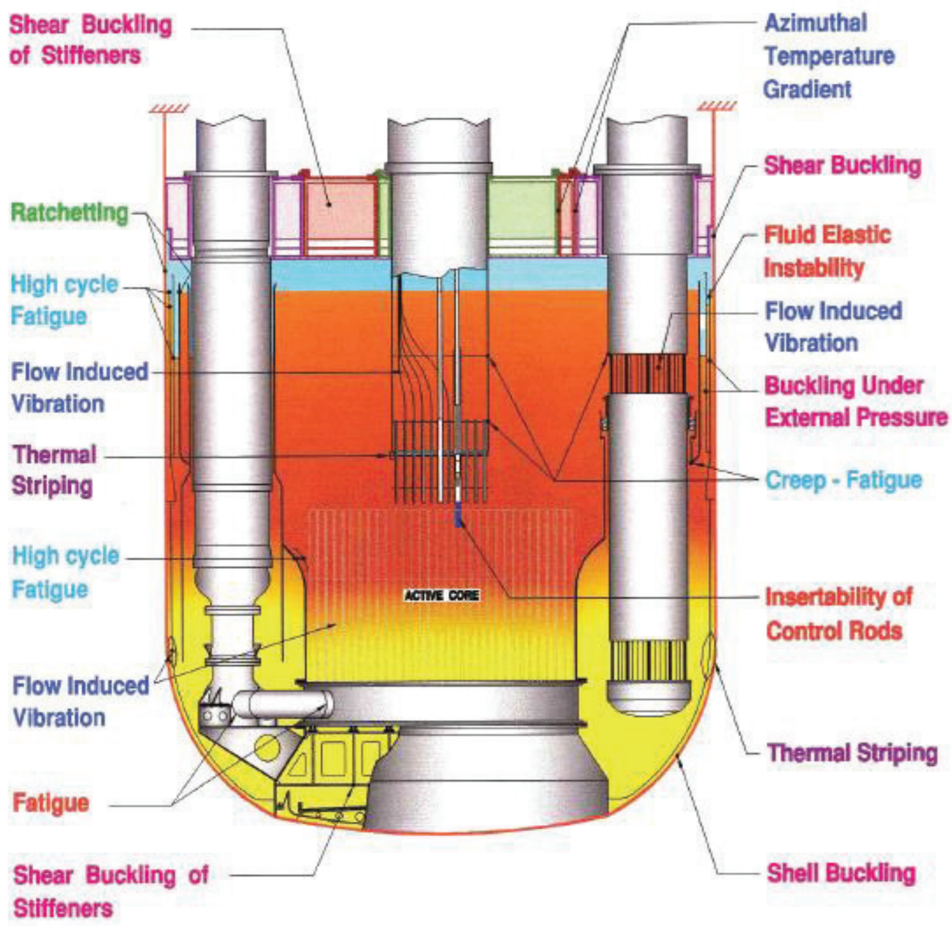

Figure 1.1 Different damage modes in PFBR components [7]

Fabrication of these components invariably involves welding [12]. Hot cracking is a major problem in welding of fully austenitic stainless steels [13]. A small amount of δ-ferrite, if present can minimize the hot cracking susceptibility of the steel, since δ-ferrite has high solubility for the elements such as S, P, Si and Nb which cause hot cracking by forming low-melting eutectics during welding [14]. However, long-term exposure to high temperature in the range 823 to 1073 K leads to transformation of δ-ferrite to brittle sigma phase, thereby decreasing the creep ductility. Therefore, by adjusting the chemical composition of the consumable electrodes, the weld metal of this steel is ensured to contain 3 to 7% δ-ferrite which helps to balance between resistance to hot-cracking during welding and embrittlement of the weld metal during prolonged service exposure at elevated temperatures [14]. The welds are potential sites for defects and the integrity of the component is decided by that of the weld. Hence, in addition to tensile, creep, and fatigue data required for conventional high temperature design, the defect tolerant design and integrity assessment of welded components requires fracture toughness, fatigue crack growth (FCG) and creep crack growth (CCG) data for the welds.

Austenitic stainless steel welds normally are not subjected to any post-weld heat treatment before they are deployed in service. The room temperature FCG resistance of these welds is influenced by the presence of (a) a duplex microstructure, (b) a high dislocation density and precipitates formed during the cooling, and (c) residual stresses introduced during welding. Presence of compressive residual stresses can also influence the mechanical behaviour of the weld metal in comparison to that of the base metal.

A campaign was initiated for development of SS316LN with increased N contents in order to improve the creep properties of the material to achieve extended operating lives for the future reactors. Towards this, four variants of nitrogen-enhanced steel with 0.08, 0.11, 0.14, and 0.22 mass % of N, were chosen after initial assessments to understand the effect of nitrogen on various important properties for long-term high temperature applications. Tensile and creep properties have been found to have improved with the addition of nitrogen [15, 16]. However, preliminary investigations indicated better low cycle fatigue [17] resistance for the variant with 0.14 mass % of N out of 0.08, 0.14 and 0.22 wt%. On the other hand, the creep-fatigue interaction resistance was found to decrease with increase in the nitrogen content [18] due to the extensive intergranular cracking.

Different extents of cold work are introduced into the material while the components are fabricated. The effect of cold work on mechanical behavior of materials has been a topic of extensive research. Some studies on the effect of prior cold work on the fatigue behaviour have been carried out on SS304L(N) and SS316L(N). It has been shown that the effect of cold work is to improve the fatigue resistance at low strain amplitudes [19, 20]. In addition to an increase in the dislocation density, attendant changes in the microstructure and damage tolerance of the material can significantly influence the FCG behavior.

2.0 Objectives of the Work

1. Evaluation of fatigue crack growth behaviour of SS316LN at different temperatures and frequencies in the conventional way which included the crack closure analysis and its comparison with the literature data.
2. Analysis of FCG data on nitrogen alloyed stainless steel (SS316LN) at different load ratios in order to understand the role of nitrogen through unified approach.
3. Understanding the FCG behaviour of SS316LN welds and cold worked material through unified approach.
4. Evaluation of short crack growth behaviour through unified principles

3.0 Layout of the Thesis

The present thesis work aims to evaluate and understand the fatigue crack growth behaviour of SS316LN at different temperatures and frequencies through conventional analysis. However, some fundamental issues cannot be evaluated through conventional approach. Hence, the unified approach developed by Sadananda and Vasudevan [21] was invoked to explain the load ratio effects and short crack growth behaviour. Literature available on FCG behaviour of different austenitic stainless steels have been briefly reviewed in Chapter 2. The chemical composition of the materials used, experimental methods, data analysis procedures and characterization techniques used are described in Chapter 3. Chapter 4 deals with the evaluation of FCG behaviour at different temperatures and frequencies using conventional analysis. In Chapter 5, the effect of nitrogen content on FCG behavior of SS316LN and influence of the deformation induced martensite transformation has been examined through the unified approach. Further, in chapter 6, the unified approach was applied to describe the FCG behaviour of SS316(N) weld and cold worked SS316LN base material. The short crack growth behaviour of SS316LN analysed through unified principles is discussed in Chapter 7. Summary of the present thesis work and the scope for further research is presented in Chapter 8.

CHAPTER 2

LITERATURE SURVEY

CHAPTER 2: LITERATURE SURVEY

2.0 Introduction

In this chapter, a survey of literature on the following is presented (a) Fatigue crack growth (FCG) in metals and alloys including at elevated temperatures, and the crack growth mechanisms (b) Austenitic stainless steels and its applications, (c) FCG behavior of different austenitic stainless steels (d) effects of nitrogen in austenitic stainless steels and their significance with respect to the mechanical behavior, including crack growth, (e) effects of cold work (f) crack growth behavior of welds (g) growth of short cracks and (h) inadequacies associated with conventional FCG analysis. On the basis of this, scope of the present work has been put in perspective.

2.1 Fracture mechanics approach to fatigue crack growth

Fatigue is the process of progressive permanent structural changes due to the cyclic loading leading to the crack nucleation and growth culminating in failure. Hence, the total fatigue life comprises the initiation and propagation lifes. Generally, the initiation life is covered under the high cycle fatigue (HCF) analysis. HCF life is typically > 10^4 cycles, occurs under elastic loading and is controlled by crack initiation while low cycle fatigue (LCF) involves significant plasticity and crack propagation decides the life. The fracture mechanics approach to FCG is adopted to describe the growth of pre-existing cracks or crack-like defects, in the vicinity of which the applied stress is amplified and leads to faster crack growth than expected. There are two types of approach (a) Linear Elastic Fracture mechanics and the other is (b) Elastic-Plastic Fracture mechanics (EPFM).

Linear Elastic Fracture Mechanics (LEFM) calculates the stress field near the crack tip is using the theory of elasticity assuming that the material is isotropic and linear elastic. The LEFM parameter, viz., stress intensity factor (*K*) is defined correlating with the far-field stress and the crack length. When the *K* exceeds the material fracture toughness (K_c, the critical value), the crack will grow. The basis of LEFM is Griffith's [22] pioneering work on the application of thermodynamic concepts to crack propagation under cyclic or monotonic loading conditions. Crack extension will occur when the elastic strain energy released in the system is equal to the energy required to create the new surfaces. While this concept is well applicable for the brittle solids, it may not be directly applicable for metallic materials, which are ductile in nature. The extension of Griffith concept by Orowan [23] to metals by simply supplementing the surface energy term with plastic energy dissipation made it possible to apply this for metallic and non-metallic materials. Further, for subcritical crack growth under cyclic loading conditions, the pioneering work of Paris-Erdogan [24] related the crack growth rate to the scalar quantity called stress intensity factor range (ΔK) for the remotely applied load [24,25]. Thereafter, several papers were published [26-38] on the crack growth analysis for many engineering materials under different conditions. More recently, some attempts to relate crack growth rate to the EPFM parameter ΔJ. have been reported [39-42]. Since, in this thesis, the LEFM framework is adopted, this aspect has not been further discussed.

2.2 Fatigue Crack Growth Curve

Before going in to a detailed literature survey on FCG studies, different parameters of cyclic loading are introduced. Different types of cyclic loading conditions such as Tension-Tension, Tension-Compression, and Compression-Compression are possible with different waveforms such as sinusoidal, triangular, trapezoidal and combination thereof. To explain the loading parameters, a typical sinusoidal fatigue loading in tension-tension mode is presented in Fig 2.1 since most of the studies have adopted this kind of loading condition for practical purposes. The loading parameters assigned are P_{max} : maximum or peak load, P_{min} : minimum load, ΔP: Load range (P_{max}–P_{min}) with the load ratio $R(= P_{min}/P_{\max})$.

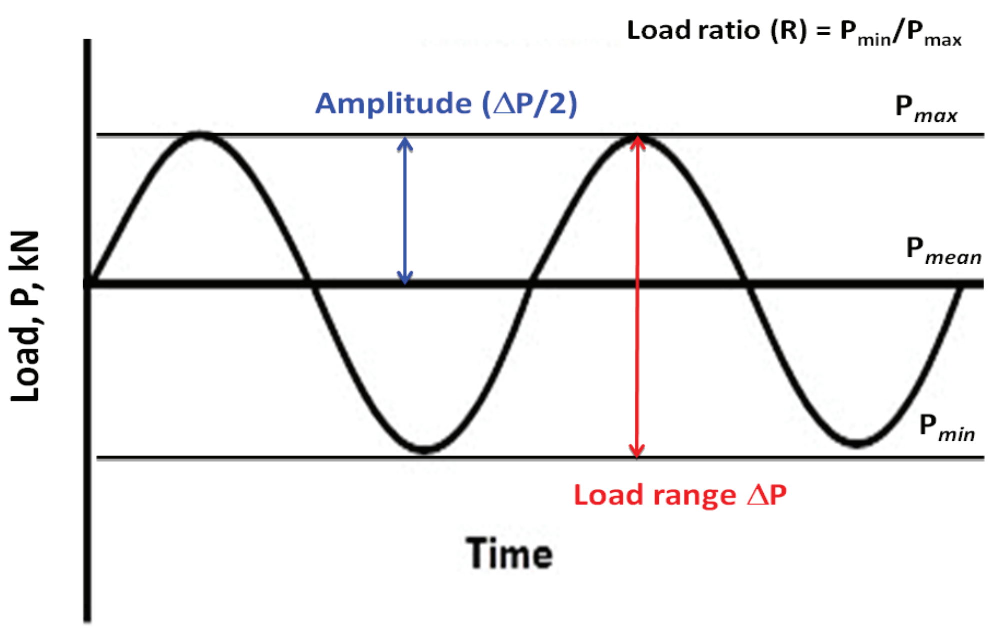

Figure 2.1 A sinusoidal cyclic loading pattern with the load parameters

Considerable research has been carried out to establish FCG relations [23-25] between the crack growth rate *da/dN* and the driving force, viz., the stress intensity factor range ΔK, (i.e., K_{max}–K_{min} where K_{max} and K_{min} are the maximum and minimum stress intensity factors corresponding to P_{max} and P_{min} respectively) for varieties of materials. Schijve has classified different stages of fatigue, starting from the crack initiation to growth and final failure [38]. For the crack growth analysis, FCG sigmoidal curve is important which consists of three regimes, namely, region I- threshold regime , region II- Paris regime and region III- fast fracture regime, as shown in Fig. 2.2. The different regimes of FCG, their importance and characteristics have been discussed in detail in the following for the sake of clarity.

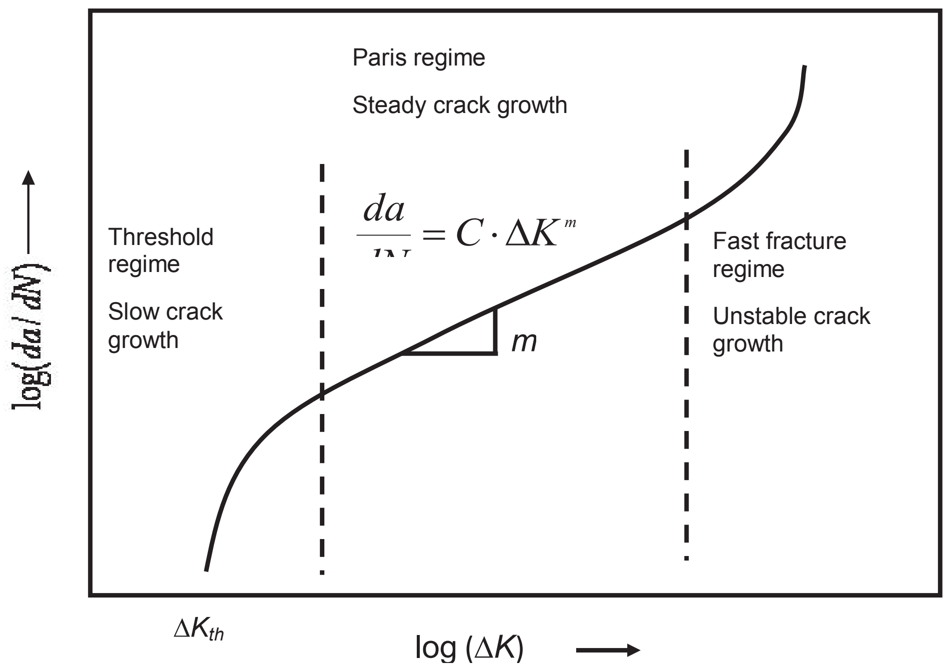

Figure 2.2 Schematic presentation of fatigue crack growth curve

2.2.1 Threshold Regime –I

From Fig 2.2, in the regime I, FCG is limited by the threshold stress intensity factor range ΔK_{th}, below which crack growth rate is negligible for any practical purpose [43]. Generally, in the threshold regime, crack growth is by single slip process, and is referred as stage I. Thus, the crack growth is significantly influenced by microstructure. Crack interaction with microstructure dictates the crack growth rate [44-50]. The crack propagation rate during stage I is in the order of atomic distance per cycle and produces a practically zigzag type crack path and faceted fracture surface. When duplex or multiple slips get activated, it can lead to the crack growth transition from stage I to stage II mode and the overall crack plane becomes perpendicular to the principal stress, and the crack enters stage II. Experiments for the threshold measurement are conducted usually through load shedding procedure, where the ΔK is gradually reduced until the crack growth rate reaches a very small value, usually of the order of 10^{-9} m/cycle or less. The FCG rate in the threshold regime is more sensitive than the other regimes not only to the microstructure, but also to testing conditions such as temperature, R (load ratio), environment, frequency of loading etc.

2.2.2 Intermediate Region of Crack Growth (Regime II)

Paris regime: At intermediate ΔK levels, the crack growth rate da/dN is correlated to the driving force ΔK by the well-known Paris equation or steady state crack growth regime discussed below, since it has practical significance.

$$da/dN = C(\Delta K)^m \qquad ---(1)$$

where the da/dN is the crack growth rate, ΔK is the stress intensity factor range, coefficient, C and the exponent, m, are material constants. The Paris regime is generally considered to be less sensitive to microstructure, environment and R (= $K_{\min}/K_{\max}$) when compared to threshold regime. Paris regime of fatigue crack growth in engineering alloys has been the subject of most extensive research, due to its potential use in life prediction. While for most engineering alloys, m is found to be in the range 2 and 4. It is known that the crack growth rate is proportional to crack tip radius, which is a function of $\left(K|\sigma_{ys}\right)^2$ and hence the m is supposed to be around 2. However, the higher value of m stems from the dislocation shilelding at the crack tip generally observed for the high hardening materials as explained in detail

in [51].

The microscopic mechanism of FCG in this regime has been explained [52] based on the formation of striations as presented schematically in Fig 2.3. At the start of the loading cycle the crack tip is sharp (Fig. 2.3(a)), and as the loading part of the cycle progresses (Fig. 2. 3(b)), slip is concentrated at the crack tip along planes at 45° to the plane of crack. As the crack widens to the maximum extension, i.e., peak load, it grows longer by plastic shearing and at the same time its tip becomes blunt as in Fig. 2.3(c). When the load reverses, the slip direction in the end zones is reversed (Fig. 2.3(d)). The crack face is crushed together Fig. 2.3(e), and the new crack surface created in tension is forced into the plane of the crack where it is partially folded by buckling to form a re-sharpened crack tip 2.3(f). The re-sharpened crack is then ready to advance in the next stress cycle. The rates of FCG are influenced by several concurrent and mutually competitive mechanistic processes involving the microstructure, mechanical load variables and environment as well as by crack closure effects discussed later in this chapter. Fatigue fractures generated during regime II fatigue exhibit crack marks known as fatigue striations

[49]. Generalized crack growth relations between FCG rate and the driving force ΔK, in this regime have been established in the literature [53].

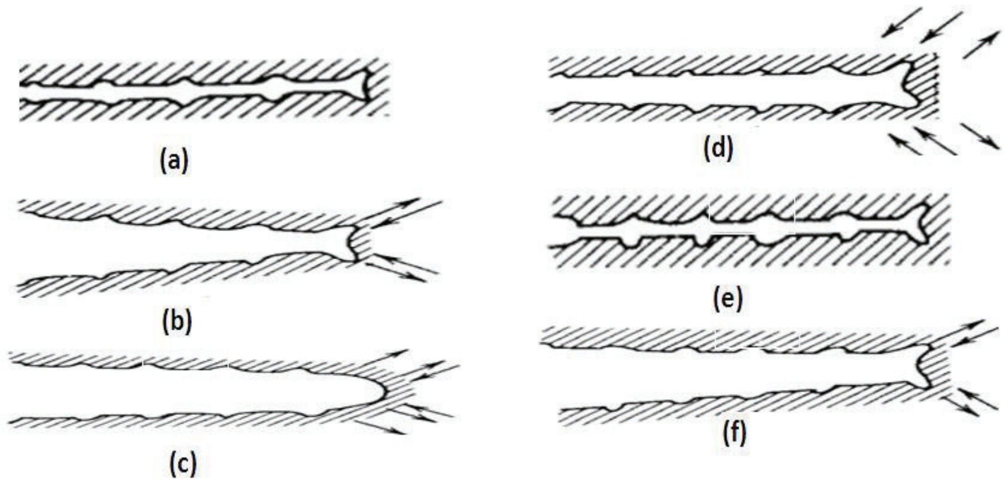

Figure 2.3 Shear slide model for formation of striations on the fracture surface [52]

2.2.3 High growth rate regime (Regime III)

At very high ΔK values, the FCG rates are significantly higher than those observed in the Paris regime. The sensitivity of crack growth to microstructure, load ratio and stress state (i.e., plane stress and plane strain loading) is also very pronounced. However, crack propagation rates are too rapid to be affected strongly by the test environment. The maximum stress intensity factor value for the fatigue cycle, K_{max} approaches the fracture toughness of the material, K_c (or K_{Ic}, in mode I - opening mode- plane strain). It should be noted that at high values of ΔK in ductile solids, the plastic zone dimensions become large in typical laboratory test specimens. Consequently, LEFM characterization of FCG may become invalid as K_{max} become K_{Ic}. At high ΔK levels approaching fast fatigue fracture, static fracture modes, such as cleavage, intergranular separation, and fibrous failure occur in addition to striation growth. The K_{Ic} obtained from cyclic loading is more in the case of ductile materials when compared to monotonic loading due to the crack tip blunting or losing the plain strain condition, while for the brittle materials it is nearly the same [29,54]. Johnson et al. reported that the thickness effects are significant when crack growth approaches the unstable regime due to net section plasticity [55].

2.3 Crack closure

The concept of crack closure has been introduced to explain several anomalous observations during FCG studies on different materials. Notable among them are the R ($=K_{min}/K_{max}$) effects, temperature and environment dependence of FCG rate. The various mechanisms proposed for crack closure for different materials and test conditions are described in this section.

2.3.1 Plasticity induced crack closure

Elber [52-58] argued that during application of constant amplitude cyclic loading, a plastic zone is formed around the crack tip in the loading portion of the cycle, which leads to a compressive stress in the wake of the crack tip in the unloading part. This causes an attendant reduction in crack opening displacement range and partial crack closure during some part of the load cycle, leading to a reduction in the driving force (ΔK) experienced by the crack tip. There are several numerical studies on the plasticity induced crack closure available in the literature [59-62]. Some reports indicated that the plasticity-induced closure is important and some others suggest that it may not be a major contributing factor under plane strain condition where the crack growth is very low [63, 64]. Based on the dislocation theory of the crack growth, plasticity does not contribute to the crack closure behind crack tip [65, 66].

2.3.2 Oxide induced crack closure

Oxide induced crack closure is assumed [44, 46, 49] to be predominant at high temperatures and in different oxidizing environments, and is dependent on the load ratio (R), ΔK and frequency. During propagation of the crack, the presence of moist atmosphere leads to oxidation of the freshly formed fracture surface and leads to premature contact of the mating surfaces under low ΔK (in the near-threshold region), or low R conditions causing a reduction in the crack-tip driving force. Continuous breaking and forming of oxide scale behind the crack tip occurs leading to fretting. This mechanism can lead to the build-up of oxide layer, up to 0.2µm, which is 20 times more than that formed on a freshly prepared smooth surface in low strength steel. Oxide debris or other corrosion products form wedges between the crack faces. The oxide-induced crack closure is minimal at the near-threshold regime for aluminum alloy inpeak-aged condition and depends on the chemical composition [**67**]. The comparison of FCG behaviour of varieties of steels in different heat treatment conditions and tested at different frequencies revealed that the crack closure effects depend on the alloy chemistry, ageing treatment and testing frequencies [67].On the otherhand,an increase in the threshold intensity factor range (ΔK_{th}) has been observed in vacuum for tempered steel [68, 69], aluminum [70, 71], and titanium [72]. Also, it has been observed that in some aggressive environments, the crack growth rate in A470 and A471 materials in the threshold region was lower than in inert atmosphere [73]. Thus, in the threshold region, fatigue crack propagation is very sensitive to the environment.

2.3.3 Phase transformation induced crack closure

Stress or strain-induced martensitic transformation generally reduces crack growth rates, increases the ΔK the extent of which depending on the extent of martensite [75, 76]. This was attributed to the transformation induced crack closure promoted by the constraint of the surrounding elastic material on the deformed region at the crack tip. Transformation of the entire specimen would not result in appreciable crack face contact. For this reason, transformation induced closure is strongly influenced by the size and geometry of specimen and of the fatigue crack. During cyclic loading, martensitic transformation occurs in the metastable austenitic stainless steel, which lowers the crack growth rate. The transformation from γ to α′ martensite greatly enhances work hardening rate, tensile strength, fracture toughness, ductility, and formability, [77], which most likely influence FCG in 316 and 316L. However, at high temperature, deformation-induced martensitic transformation in metastable austenitic stainless steel is not likely. Moreover, some studies in ceramics [78] and other class of steels [79] have also noted the beneficial effect of the transformation toughening on the crack growth resistance due to the phase transformation at the crack tip.

2.3.4 Roughness-induced crack closure

Crack closure due to roughness of crack faces is fully based on microstructure because crack path deviations should occur in order to create a rough crack face. Crack deflection and branching occurs near the threshold regime causing an increase in roughness-induced closure levels for the relatively low roughness crack faces reducing the ΔK level experienced at the crack tip. In aluminum alloys with underaged structure, roughness induced crack closure is observed, which results in better FCG resistance, specifically in the near-threshold region [80-83].Several numerical simulation techniques have been adopted to rationalise the FCG behaviour near threshold regime due to the roughness induced crack closure effect [84-86]. The increased crack closure effect in copper was attributed to the serrated crack path, which promotes the roughness induced crack closure [87]. Moreover, mode II displacements due to crack path deviations influenced by the microstructure promote roughness induced crack closure at the threshold level [88-89]. However, at high temperature, this crack closure mechanism is less effective.

Thus, it appears that the phenomenon of crack closure is important and its effects need to be incorporated in the FCG data. The ASME and RCC-MR codes recommend this practice [90-91] in determining the FCG properties to be used for the damage tolerant design. The closure measurement and determination of closure-free FCG parameters are also required for FCG-based life prediction. A schematic figure to explain the effective (or closure-free) ΔK, i.e., ΔK_{eff} is presented in Fig 2.4.

In addition to the crack closure effect, several other mechanisms have been proposed such as intrinsic and extrinsic toughening at the crack tip under cyclic or monotonic loading which can contribute to the crack growth resistance. These toughening mechanisms have been classified in different ways [29]. These classes involve crack tip shielding from (a) crack deflection and meandering, (b) inelastic or dilated zones surrounding the wake of the crack, termed zone shielding, (c) wedging, bridging and/or sliding between crack surfaces, termed contact shielding, and (d) combined zone and contact shielding. Any or all of these can contribute to the crack tip shielding.

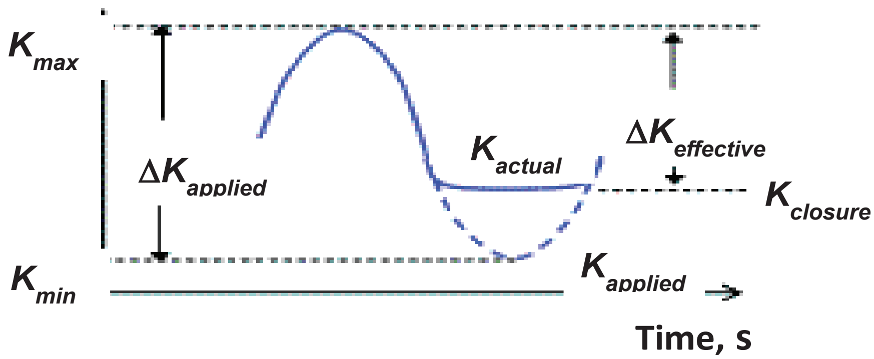

Figure 2.4 Schematic presentation of crack closure correction for effective crack tip driving force

After the crack closure correction, the effective stress intensity factor range, ΔK_{eff} is considered as the driving force for FCG. In ceramics, intermetallics, and composites, improved crack growth resistance due to crack tip stress shielding by various phenomena like bridging, interlocking and branching of the cracks has been observed. In such cases, the crack tip stress intensity factor range ΔK_{tip} that takes into account the shielding effects, rather than ΔK_{eff}, is considered to be more appropriate as the driving force for crack growth. Mutoh et al have examined the effect of crack tip stress shielding on the FCG behaviour of a duplex structural steel and ferritic steels with different microstructure [92-93].

2.4 High-temperature fatigue crack growth

High temperature components experience fatigue loading conditions due to temperature fluctuations, flow induced vibrations etc. Under such conditions, any preexisting defects or those generated insitu tend to grow. Hence, the crack growth studies at high temperature are important for structural integrity assessment. Several extensive studies on high temperature FCG have been carried out on steels [94-98] and nickel based alloys [99]. In addition, there have been attempts to apply EPFM parameters for characterization of high temperature FCG [99,100].At high temperature, crack growth is controlled by various factors such as frequency, type of slip and deformation mechanism. The crack growth mechanism changes with change in the slip character. For example, the crack growth at room temperature follows the preferred slip planes leading to the relatively more tortuous crack path than at high temperature where slip is more homogeneous resulting in straight crack path. However, these mechanisms depend on the crack tip strain rate and temperature. Moreover, at high temperature, the mechanisms responsible for FCG become time-dependent rather than cycle dependent, because thermal activation allows dislocations to climb out of their original slip planes. Climb is aided by diffusion of vacancies, which is a time-dependent phenomenon, and hence frequency and strain rate [101-103] and wave form [104] become important parameters in high-temperature fatigue. In general, the time-dependent processes that control FCG at high temperature are creep and environmental effects. At high temperature for time-dependent FCG, the stress intensity factor range is still the controlling factor as long as the crack tip plastic zone size is smaller than the crack length and uncracked ligament. At high temperature, the material is not metallurgically stable; thermally activated microstructural changes occur, which alter the dislocation sub-structure by strain aging, recovery, and precipitation. In type 316 stainless steel, fatigue-induced precipitate formation on dislocation cell boundaries at 650ºC has been reported [97].

The mechanisms responsible for the inception of fatigue flaws at high temperature can be generally grouped into the following categories: (i) cracking induced by cyclic slip, (ii) grain boundary cavitation, (iii) grain boundary sliding and the attendant development of wedge cracks, (iv) nucleation and growth of voids at inclusions and precipitates, and (v) oxidation and corrosion [98]. Of these, (ii), (iii) and (iv) are damage mechanisms in creep. Apart from the above mechanisms, another metallurgical phenomenon plays a significant role in fatigue and FCG. Dynamic strain ageing (DSA) affects the FCG and its role has been examined for ferritic steel [105] and nickel base alloy [106]. It is found that DSA exerts a beneficial influence on the FCG resistance. On the other hand, the effect of DSA is detrimental under low cycle fatigue testing conditions. Since DSA is a strong function of temperature and crack tip strain rate, variations in temperature and frequency lead to changes in the DSA mechanism and thus the fatigue properties. The influence of DSA under different loading conditions have been examined for different classes of steels [103, 107].

2.5 Fatigue crack growth studies in Austenitic stainless steels

Austenitic stainless steels being an important material for high temperature structural components, their FCG behavior has been studied extensively in literature. A number of studies have been made on different grades of austenitic steels to investigate the influence of several parameters such as temperature [98, 108-111], cyclic frequency [111], surrounding environment [112-115], specimen size [116, 117], microstructure [118, 119], cyclic load ratio [120], neutron irradiation [121, 122] etc on FCG behaviour. Generally, with increase in test temperature, the FCG resistance decreases. However, in the intermediate temperature (673 K to 823 K) regime, it was found that DSA enhances the crack growth resistance [105]. The crack tip strain rate depends on the cyclic frequency and is found to alter the crack growth behaviour with temperature [105]. The fatigue crack propagation characteristics in air at room temperature and at elevated temperatures in sodium and vacuum are evidence that the thermally activated component of crack propagation observed in air is an environmental effect [112-115]. Further, FCG results of SS304 in hydrogen, argon and moisture indicated that the material is sensitive to the hydrogen atmosphere. Partial intergranular and transgranular fracture was observed at the fracture surface of the material tested under argon, while only transgranular fracture was observed for both the hydrogen and moist air environment. However, in the hydrogen environment promoted the hydrogen embrittlement resulted in the low threshold value when compared to the other two environmetal conditions [112]. The effect of specimen size on the fatigue crack growth rate behavior of annealed AISI Type 304 stainless steel was studied at two stress ratios at an elevated temperature and the results show essentially equivalent crack growth behavior over the entire range of data overlap for different thicknesses, regardless of whether the remaining ligament criterion of ASTM E647-78T is satisfied or not. The results of this study also indicated that the flow stress criterion is more appropriate for strain-hardening materials such as austenitic stainless steels [116]. The FCG behavior of 316L processed by selective laser melting was found to be drastically affected by solidification and resulting microstructure [88]. Columnar grains preferentially oriented in building direction are present in as-processed and heat treated conditions. Depending on the relation of crack growth direction and grain long axis, different FCG rates, especially in the near threshold regime and at higher ΔK values, are observed. Variations in microstructure and mean stress do not lead to significant changes in the crack-propagation rate in the intermediate crack growth regime of FCG curve. For example, Paris exponent *m* was found to be between 2.5 and 2.7, consistent with the ductile striation mechanism. At high growth rates, crack propagation rates become sensitive to microstructure and *R* consistent with the occurrence of static fracture modes during striation growth. At near-threshold regime, significant effects of *R* and microstructure rates on the crack growth rates were observed; the maximum sensitivity to *R* occurs in lower-strength material and the maximum sensitivity to microstructure occurs at low *R* [43-46, 120]. Neutron irradiation influences the FCG resistance of SS 304 and SS 316; at low temperature these effects are lower for SS304 than in SS316, but at 1073 K these effects are found to be negligible for SS316 when compared to SS304 [121, 122]. The above studies bring out the importance of different variables in the FCG behavior of austenitic stainless steels. It is also seen that the influences of these parameters depend on the chemical composition.

2.6 Effects of Nitrogen on Mechanical behavior of Austenitic Stainless Steels

2.6 1 Role of nitrogen in the Austenitic Stainless Steels

Nitrogen in steels is basically an austenite phase stabilizer. It improves the solid solution strengthening, leads to finer grain size, and increases the coefficient of work hardening [15, 123]. It is known that nitrogen atoms occupy the interstitial site in the crystal lattice and is a strong solid solution strengthener. First reported in 1926 [124, 125], interstitial atoms are now central to diverse disciplines within materials science. A very small volume fraction of interstitials can have a tremendous influence on material behavior, be it steel strengthened by interstitial carbon [126], strain ageing phenomena promoted by interstitial solutes, [127] or irradiation-induced defects [128]. The phenomena of interstitial-dislocation interaction and interstitial-grain boundary interaction necessitate mesoscale and macro-scale investigations. This was demonstrated by the beneficial effects of nitrogen addition to austenitic stainless steels. Prominent is the high degree of solid solution strengthening due to nitrogen [5]. This cannot be explained on the basis of conventional interstitial-dislocation interactions since N atoms in octahedral sites of FCC could cause symmetric distortions, and thus, may not be able to bind screw dislocations in the manner C does in the BCC matrix of carbon steel [129]. Instead, it is found that asymmetric distortions occur due to the formation of Fe-N complexes. This phenomenon of complex formation is due to the unique electronic configuration of N, a feature that also results in short-range ordering (SRO)[130], secondary strengthening [129] of N-containing austenitic steel and affects the stacking fault energy (SFE). At elevated temperatures, N-containing austenitic stainless steels have a good combination of strength, ductility, and toughness. These are attributed to the influence of N on SFE as well as grain boundary strengthening [129, 130]. It is also reported that increasing nitrogen promotes strong slip localization due to the decrease in SFE [131]. Increased nitrogen content leads to significant increase in the passive film stability leading to better corrosion resistance [132].

The potential use of nitrogen alloying is due to the low cost of the process. Nitrogen enhanced steel can be manufactured in the open air (electric arc and induction furnace, electro slag remelting) by adding Nitride ferrochrome agent [133, 134]. The other route is by purging of nitrogen gas under pressure in pressurized induction furnace, pressure electroslag remelting (PSER) [134]. Apart from these powder metallurgy, surface treatment routes are also possible [134, 135].

2.6.2 Deformation induced martensite formation in Austenitic Stainless steels

It is known that Austenitic stainless Steels (300 series) are prone to stress or strain-induced martensite formation [136], especially at ambient and lower temperatures which can influence the mechanical and corrosion behaviors. Nitrogen additions can stabilize the austenite and hence can inhibit its stress-induced transformation to martensite, thereby exerting additional influence on mechanical properties. During plastic deformation transformation of austenite (γ) into martensite of hexagonal close-packed (strain-induced ε), or body-centered cubic (stress-induced α') crystal structures occur. Such transformations during plastic deformation is advantageous as it imparts a good combination of strength and toughness to austenitic stainless steels. For example, deformation-induced toughening is one of the important mechanisms to consider in the materials for structural applications. This kind of toughening is predominant in the 300 series stainless steels. Hence the potential applications of these steels have been realised recently in many ways. There are several parameters such as strain rate, temperature, and state of stress, which influence the transformation during deformation. Apart from these parameters, the alloying elements can also play a significant role in the deformation-induced martensite formation [137] through their effects on the γ-phase stability.

2.6.3 Effects of nitrogen on the mechanical properties of Austenitic Stainless steels

Botshekan et al [138] studied the tensile and low cycle fatigue behaviour of SS316LN steel at 300 and 77 K. The tensile and low cycle properties were obtained and analysed in terms of the influence of testing temperature on the plastic deformation processes and the formation of strain induced martesnite. The martensite content was analysed using measurements of the magnetic saturation. No α′- martensite was observed at 300 K under either monotonic or cyclic straining. On the contrary, at 77 K, strain-induced martensitic transformation was found to occur which is responsible for the higher elongation in tension and the secondary hardening observed on hardening/softening curves in low-cycle fatigue. The deformation induced martensite content during the tensile deformation is examined as a function of strain. A constitutive model has been developed considering the state of stress on the deformation induced martensite [139]. In low-cycle fatigue, it is a function of the applied strain amplitude and the accumulated plastic strain. For a given total strain amplitude, the plastic strain amplitude is lower at 77 K than at 300 K. Also, at lower temperature planar slip may be prevalent leading to enhanced fatigue life. The higher cyclic peak stress at 77K, due to an intermediate ageing at room temperature (300K) is related to pinning of initially free dislocations resulting from nitrogen diffusion during isothermal holding at room temperature. This results in a reduced fatigue life due to formation of short cracks due to strain localization. The strengthening, work hardening and stress corrosion cracking characteristics of high nitrogen austenitic stainless steel (0.8 mass %) have been investigated [140] and the improved mechanical properties, viz., very high yield strength and good toughness discussed with reference to the nitrogen and cold work levels. Another study [141] discussed the improved strain hardening results in terms of the formation of second order twin and glide interaction, and established formation of different types of defects under monotonic loading in stainless steel with nitrogen content of 0.04 mass %. All these studies reveal that nitrogen has a significant role on the improved mechanical properties through deformation induced martensite, in addition to other factors. It is a function test temperature, alloy chemistry and strain rate/applied stress.

2.6.4 Effects of nitrogen on Fatigue crack growth in Austenitic Stainless Steels

Chemical compositions of different N alloyed stainless steels from literature on the effect of N on the FCG properties are presented in Table 2.1. Mei et al. [142, 143] proved that nitrogen suppresses the formation of transformation induced martensite by stabilizing the austenite. Fracture and FCG data for SS304L and SS 304LN with and without cold work were generated at room temperature at two load ratios. It was clearly brought out that the conjoint effect of cold work and nitrogen at low temperature enhanced the fatigue crack growth resistance due to the formation of deformation-induced martensite. It is also interesting to note that FCG of SS304L and SS304LN at room temperature was not influenced by the deformation-induced martensite, though the extent of martensite formation was relatively higher in SS304L. Based on these observations, it can be inferred that the crack closure effects due to the transformation is insignificant. However, FCG tests at 77 K revealed a profound influence of N on the crack growth due to the extensive formation of martensite for SS 304L when compared to the SS304LN. This suggests that N plays a significant role on suppressing the martensite transformation which can be correlated with the effect of N on temperatures for martensite start (M_s) on cooling and for deformation-induced martensite formation (M_d). Hallberg et al. [144] have shown that the phase transformation occurring in the crack tip region gives rise to increase in fracture toughness of the material whereby the resistance to crack initiation, as well as the macroscopic material response are strongly altered by the presence of a martensitic phase.

Now, the FCG results of SS316L with different N contents from a preliminary study in the author's lab [131] are compared with the data by Turan and Koursaris [145] on different N variants of SS310. It is known that these classes of steels are generally used in the aerospace applications at cryogenic temperature owing to the good toughness even at sub-zero temperatures. In this case, presence of N in the range 0.15 to 0.5 mass% enhanced the FCG resistance. Comparison of the data for these variants with those of Nani Babu et al [131] on SS316LNshows that these steels are much superior to SS316LN in terms of FCG resistance. SS 310 has higher contents of chromium (Cr) and Nickel (Ni) and Silicon (Si) than SS316LN. Chromium and Silicon are ferrite stabilizers, and Ni is an austenite stabilizer. The Cr and Ni equivalents play a role on the deformation-induced martensite formation and thereby influence transformation toughening. Murayama et al.[146] suggested that short range ordering (SRO) caused by the combined effect of N and Mo, rather than the slip planarity, resulted in the improved resistance to crack growth. It may be noted that Mo is not present in SS310, however, the FCG resistance was enhanced. It shows that even in the absence of SRO, nitrogen has a significant effect on enhancing the FCG resistance.

Maeng and Kim [147] reported FCG data for SS 316L (N: 0.038 mass%) and SS316LN(N: 0.14 mass%). They attributed the increase in the crack growth resistance for the nitrogen bearing steels to the enhanced planar arrays aided by the lowering of stacking fault energy, in addition to the deformation-induced martensite formation. The extent of martensite formation was found to be same in both the steels. Vogt et al [148] performed a rough estimation of α′ martensite with X-ray diffractometry (Co tube) on a surface taken from the bulk of specimens tested at 77 K under low cycle fatigue condition at a total strain amplitude of 2.5%. Approximately 66% α' martensite was found in 316L alloy, while only approximately 4 % was found in 316LN alloy. This demonstrates the effect of nitrogen, which suppresses the formation of α' phases during cyclic straining. However, it is also obvious that even 0.23 mass % of N does not completely inhibit the formation of martensite. In addition to the above, a close look at the FCG data for SS316L from the study of Maeng and Kim [147] and from an earlier study in the author's lab [131] on three variants with different nitrogen contents indicates that the FCG data are comparable in the Paris regime and differ only in the near-threshold regime. It can be inferred that the enhanced planarity of slip and grain size refinement due to the presence of nitrogen improve the threshold for SS316LN (0.14%). Based on these observations, it is clear that the influence of deformation induced martensite varies with applied stress, temperature and chemical composition [142, 143].

Table 2.1 Chemical composition of different N alloyed stainless steels

Designation	C	N	Mn	Cr	Mo	Ni	Si	S	P	Fe
SS316LN[10]	<0.03	0.16	<2	17.2	2.50	13.5	<1	<0.03	<0.045	Bal
SS304L[144]	0.024	0.074	1.63	18.70	-	8.64	0.51	0.010	0.021	Bal
SS304LN[144]	0.021	0.139	1.77	18.54	-	9.55	0.78	0.009	0.014	Bal
SS310[145]	0.036 0.064	0.016 0.525	1.41 1.68	24.70 26.60	-	18.47 19.40	0.33 0.45	0.001 0.011	0.024 0.032	Bal
SS316L[147]	0.020	0.038	1.86	17.38	2.36	11.21	0.51	0.0054	0.027	Bal
SS316LN[147]	0.018	0.14	1.67	17.58	2.79	11.23	0.46	0.0008	0.021	Bal
SS316L[148]	0.024	0.033	1.60	17.40	2.139	13.58	0.53	0.013	0.010	Bal
SS316LN[148]	0.023	0.235	1.518	17.22	2.223	13.69	0.534	0.012	0.01	Bal

Although the comparison indicated that the FCG resistance of SS316LN is inferior to that of SS310 tested at 77 K, the FCG trend shows that the role of N content (0.04 to 0.52 mass %) in both the steels is the same. Examining the data of Turan and Koursaris [145] on FCG of SS310 indicated that the crack growth resistance increases with N content, which was attributed to enhanced planar slip during deformation promoted by reduced SFE. From a comparison of the chemical compositions of SS310, SS304LN, and SS316LN, it can be seen that the highest N content is in SS310, which shows the best crack growth resistance, indicating that nitrogen enhances the fatigue-resistance. In SS316LN, the Cr and Ni contents are higher than in SS304LN and SS310. Even in the absence of Mo in SS304L and SS310 show better FCG resistance than SS316LN, which means there is no role of Mo, *per se*, on the improved FCG resistance. Thus, the role of Mo alone on FCG resistance can be ruled out. In another study on the combined effect of Mo and N on FCG of austenitic stainless steel, it was observed that the Mo-N pair is much stronger than Cr-N or Ni-N [146]. Thus, there is a change in the dislocation structure predominantly due to the Mo-N pairs [146] which promotes the SRO. Thus, for the overall improvement of the FCG resistance, the nitrogen content is to be optimized to have the beneficial effects of toughening by deformation-induced martensite and increased resistance to crack initiation by enhancing planar type dislocation structure. Detailed investigations need to be carried out on the SS316LN steel with varying nitrogen concentrations towards this, and to ascertain the mechanism which is responsible for improved FCG resistance of nitrogen-bearing austenitic stainless steels.

2.7 Effect of cold work

Lee and Taylor [140] presented results on crack growth curves for high nitrogen stainless steels (HNSS) with about 0.85% nitrogen, in the annealed as well as 28% and 50% cold-worked conditions in air and in 3.5% NaCl solution. In both the environments, the FCG curves for all the three material conditions nearly overlap with each other. However, the cold-work appears to accelerate slightly the fatigue crack growth, reduce the ΔK_{th}, and shorten the fatigue crack growth life compared to the annealed material. This trend is more obvious for the higher level of cold-work. Since the stress-life curves show that the total fatigue life under a given maximum applied stress is longer for the material with higher cold-work level (in spite of the fact that it had exhibited a slightly higher FCG rate), the fatigue-crack initiation life must be longer for the cold-worked specimen. In other words, cold-work extends the fatigue-crack initiation life and the total fatigue life, but shortens the fatigue crack growth life of HNSS. Threshold regime can be affected by the yield stress, which in turn depends on the grain size; data shows that ΔK_{th} decreases with increase in yield stress which can be partly due to reduced grain size and/or decreased environmental sensitivity [149]. Moreover, the slip planarity in this HNSS introduces tortuous crack path and enhances crack-growth resistance by enhancing the mode II loading at the crack tip, resulting in decrease in the mode I component of ΔK experienced by the crack tip. The effect of the roughness of the crack surface (causing partial crack closure) is a secondary effect but not the main cause for increased thresholds [149-151].

2.8 Fatigue Crack growth behaviour of stainless steel welds

The fatigue crack growth behaviour of welds is generally different from the base material due to their inherent microstructural and mechanical heterogeneity. Microstructural heterogeneity arises from the dendritic structure due to the rapid cooling and heating cycles of the weld material during welding. Also, duplex nature of the microstructure, for example in stainless steel welds with austenite and δ-ferrite, in addition to the inclusions, precipitates and high dislocation density contribute to the heterogeneity. The δ-ferrite is normally introduced in stainless steel welds in order to avoid hot cracking by adjusting the chemical composition of the weld electrode. Any crack growing in the material encounters different kinds of interfaces such as grains, phase boundaries, inclusion and weld beads due to the multipass welding and the growth will be temporarily retarded. Further growth of the crack may require a crack path deviation. Preliminary results from the author's lab [152-153] and previous literature [152-154] on welds reveal fluctuations in the crack growth rate at room temperature presumably due to the frequent changes in the crack path. The most important factor which influences the FCG of welds is the presence of residual stresses, which lead to mechanical heterogeneity. The residual stresses arise in the weld because of the rapid cooling of weld pool, and the nature of residual stresses changes across the weld. Generally, weld centre may have compressive residual stresses and towards the base metal these residual stresses can be tensile or compressive in nature depending on several factors such as the microstructure [155-159], chemical dilution [160], weld geometry [161] and heat treatment [155,156]. These residual stresses gets redistributed during the crack growth under cyclic loading [161]. Hence, in order to understand the contributions from microstructural heterogeneities such as duplex structure, grain size variations etc and mechanical heterogeneities such as varying magnitude and nature of residual stresses, FCG behavior of welds needs to be examined.

A study on the evaluation of tensile and FCG behavior of stainless steel narrow gap welds shows that the tensile strength with in the fusion zone did not show spatial dependency. However, there were variations in the FCG properties which were attributed to the dendritic microstructure and compressive residual stresses developed during the weld process [159]. The poor FCG resistance of the MIG weld metal of stainless steel when compared to base and HAZ has been attributed to the large tensile residuals stresses in the weld. Moreover, factographic morphology revealed the large size striation with shallow dimples indicating the low plasticity [162]. The effect of welding processes like submerged arc welding (SAW), flux-cored arc welding (FCAW), shielded metal arc welding (SMAW) on the FCG properties has been discussed extensively in the literature. It was found that the SAW welds have better FCG resistance than the others. The favorable results obtained by SAW are probably due to a deep penetration on the first layer with favorable HAZ material properties and small initial discontinuities. There may be benefits to gain from this observation in design practice if the welding process is carefully controlled [163]. From a study on the effect of post weld treatments on the FCG behaviour, a compressive stress induced by post-weld treatment was found to eliminate the tensile residual stresses and generate compressive residual stresses, which improves fatigue strength and FCG threshold, ΔK_{th} [164]. Influences of chemical dilution and the number of weld passes on residual stresses in a multipass low-transformation-temperature (LTT) weld were investigated experimentally and compared with the finite element modelling. A coupled thermal-metallurgical-mechanical (TMM) model that took into account the chemical dilution effect on the residual stress contribution was validated by good agreement between the predictions and experimental measurements [160]. All these studies indicate that the weld properties depend on several factors which need to be given more attention during the evaluation of welds for their mechanical properties in general, and for fatigue crack growth analysis in particular.

2.9 Short crack growth behaviour

The importance of understanding the initiation and the growth kinetics of an incipient crack before it becomes long enough for detection from the point of diagnostics, and of quantifying for fatigue life of a component for prognostics cannot be overemphasized. There is considerable evidence that the growth rates of short cracks are significantly higher than those of long cracks, when expressed in terms of the applied crack-tip driving force ΔK. Cracks, being high energy defects, must invariably initiate either at pre-existing or in-situ generated stress concentrations. In many cases, the initiation of an incipient crack and its growth to a detectable size takes a considerable fraction of fatigue life to the extent that, often, the usefulness of a component in service is defined by the crack initiation life. By definition, a crack is assumed to have been initiated when it is '0.01 inch-long' based on its detectability, and therefore it involves inception and growth of a short crack to the experimentally detectable limit. Even for a smooth specimen at endurance, ten million cycles or more are required to cause the needed fatigue-damage in terms of dislocation-plasticity, slip band intrusions and protrusions, etc., for crack initiation and growth to cause failure. There seems to be an apparent dichotomy in terms of a) the large number of cycles required for an incipient crack to form and grow as in the case of a smooth specimen and b) the perceived higher growth rates observed for short cracks in relation to large cracks when the growth rates are expressed in terms of the applied stress-intensity factor range, ΔK. Recognising its importance, there has been considerable work done in the analysis of the short crack growth behavior in metals and alloys in terms of its characterization and in developing predictive relations. Many reviews on the topic have been presented in the past [165-175].

2.9.1 Classification of short cracks

A simple definition of a short crack is that its growth kinetics are different from that of a long crack when the applied crack tip driving force is expressed in terms of ΔK. Long cracks are those whose growth rates (da/dN) are independent of the specimen geometry and crack length. Hence, by definition, the growth rates of short cracks are higher than those of long cracks and they vary with crack length. This behavior has been characterized as the 'breakdown of similitude' for short cracks. Short cracks have been classified [168] as a) mechanically, b) microstructurally, c) physically and d) chemically short. Mechanically short-cracks are those that initiate in the stress field of well-defined pre-existing stress concentrations. Microstructurally short cracks [171] are those whose length scales are comparable to microstructural parameters such as grain size, etc. Physically short cracks are sufficiently long in relation to the microstructurally short cracks but are small enough that their growth rates differ from those of long cracks. Finally, chemically short cracks are those which grow at significantly higher rates than the long cracks due to the overpowering chemical crack-tip driving forces present at the crack-tips [169-173].

2.9.2 Similitude breakdown

The underlying assertion and the associated analyses in almost all published papers on short cracks are that there is a breakdown of similitude in terms of short crack growth kinetics. Similitude can be simply stated as 'equal crack tip driving forces cause equal crack growth rates' if a) material-microstructure and test environment remains the same, and b) crack growth mechanism remain the same. The similitude forms the very basis for the life prediction of a component in service using the experimental crack growth rate data. In the case of long cracks, for a given crack tip driving force expressed in terms of ΔK, the crack growth rate remains the same irrespective of the specimen geometry and crack length. Since for short cracks, (i) the growth rates vary with crack length for the same ΔK, and are much higher than those of the long cracks, and (ii) the thresholds are dependent on crack length, and are much lower than that of long cracks, it has been postulated that there is a breakdown of similitude [176-186].

2.10 Fundamental problems associated with the conventional fatigue crack growth analysis

As already described in the previous sections, from the inception of the empirical relation (Paris law) between the steady-state fatigue-crack growth rate (da/dN) and applied stress intensity factor range (ΔK) [24, 25], several models for the crack growth have been proposed in the literature for the prediction of life of a component subjected to cyclic loading. In many of these models, the *R*-dependence of FCG rates in both the Paris and the threshold regimes were considered as an anomaly. As already mentioned in Section 2.3, to account for the observed *R*-dependence of crack growth rates, Elber [56-58] proposed the crack-closure effect. In essence, the crack closes prematurely during unloading due to crack wake plasticity. Hence the effective amplitude is less than the applied amplitude, particularly for low *R*-values. Budiansky and Hutchinson [185] have provided a theoretical model showing that crack closure can occur under the plane-stress conditions due to the inflow of material from the sides into the crack. Empirically, the concept was later extended to plane-strain conditions. In addition, several empirical models were developed by incorporating the crack closure effects into the crack growth analysis [49, 168]. Crack closure, thus, is an extrinsic factor brought into account for the *R* effects. There are several publications on the crack closure effects on FCG from 1970 to 1987, which thereafter leveled off [187, 188]. As already detailed in Section 2.3, besides the plasticity induced crack closure, many other forms of crack closure mechanism have been proposed [49, 168]. Some, such as oxide-induced crack closure, are very specific and arises when the material in the crack-wake gets oxidized, reducing the crack opening. The ASTM round robin test programme pointed to several uncertainties to the plasticity-induced crack closure and its estimation [188]. In addition, short cracks were found to grow at stress intensity factor ranges well below the long crack growth thresholds, exhibiting higher crack growth rates. To address this issue, the similitude break-down was invoked. The similitude, which forms the fundamental basis for the use of fracture mechanics in service using the laboratory-generated data, requires that equal crack tip driving force causes equal crack growth rates. The similitude breakdown in the short crack growth regime implies that applicability of LEFM in the short crack growth regime becomes questionable.

2.11 Two-parameter approach to Fatigue crack growth

FCG is normally represented by da/dN vs ΔK for different R values. A unified approach was developed to show that the fatigue crack growth for several materials can be uniquely analyzed using two parameters, ΔK and K_{max}, without invoking an extrinsic factor, the plasticity induced crack closure [189-193**]**. If crack closure is present, then it forms an additional factor that needs to be considered in the analysis of FCG, but it is not a substitute for the two-parametric requirement. For FCG, ΔK and K_{max} form the two required parameters since thresholds in terms of both can be easily defined. It appears that the two-parameter approach or unified approach is fundamental in nature and hence it is an appropriate tool to evaluate the intrinsic resistance of the fatigue crack growth of metallic or non metallic materials. Very recent studies also show that the variation in the crack growth with load ratio is not because of the crack closure effects [194]. The two-parametric approach may prove to be useful for a fundamental understanding of the FCG behaviour.

2.12 Scope of the work

Based on the above brief history, it has been realized that *there are two fundamental issues yet to be resolved (1) effect of load ratio on fatigue crack growth and (2) the reason for higher crack growth rate for short cracks when compared to long crack. Attempts have been made in this thesis to address these two fundamental issues through characterizing the FCG behaviour of SS316LN steel, base, weld and cold worked materials*. In the process, effect of nitrogen content, test temperature and frequency effects have been studied

CHAPTER 3

EXPERIMENTAL DETAILS

CHAPTER 3: EXPERIMENTAL DETAILS

3.0 Introduction

This chapter presents the details of the materials used in the study, specimen fabrication including welding and cold working, sample preparation for fatigue pre-cracking and fatigue crack growth (FCG) testing. Procedure for calibration of Direct Current Potential Drop (DCPD) for crack depth measurement at different temperatures, machines used for the pre-cracking and FCG testing, testing procedure and standards, data acquisition and analysis procedure are outlined. The characterization techniques used for hardness measurements, microstructural and fractographic examination, the instruments used for evaluation of deformation induced martensite and substructural changes during the deformation are also described in this chapter.

3.1 Materials and specimen preparation

3.1.1 Materials

The materials used in this study are 316L stainless steel with 0.08, 0.14 and 0.22 mass % of nitrogen designated as 8N, 14N and 22N in the form of plates of 30 mm thickness in the solution annealed condition. The commercial scale heats of 316LN SS were produced through double melting process as described below. Primary melting of the steel was carried out in an air induction melting furnace of 2.5 ton capacity. The charge consists of pure raw materials in order to achieve close control on the chemical composition of the heats. Nitrided ferrochrome was used to achieve the required amounts of nitrogen in the different heats. Other major and minor elements were controlled to the same level in all the heats. Secondary melting was carried out by electroslag refining process in order to produce the steel with very low inclusion content. The electroslag refining ingots were hot forged into slabs and the slabs were subsequently hot rolled into plates. The hot rolled plates were given a final solution annealing treatment between 1323 and 1423 K, followed by water quenching. The chemical compositions of these three variants are presented in Table 3.1. The optical microstructure of 8N, 14N and 22N are presented in Fig. 3.1 (a-c). All the three materials in the solution annealed condition had an equiaxed grain structure and average grain sizes as measured by linear intercept method as per the ASTM standard ASTM E112-12. [197]. The average grain size found to be in the range 70-80 μm for 8N, 14N and 22N variants, further discussed in the Chapter 5.

Table 3.1 Chemical composition of different N alloyed 316L stainless steels

Designation	C	N	Mn	Cr	Mo	Ni	Si	S	P	Fe
8N	0.027	0.08	1.70	17.53	2.49	12.20	0.22	0.0055	0.013	Bal.
14N	0.025	0.14	1.74	17.57	2.53	12.15	0.20	0.0041	0.017	Bal.
22N	0.028	0.22	1.70	17.57	2.54	12.36	0.20	0.0055	0.018	Bal.

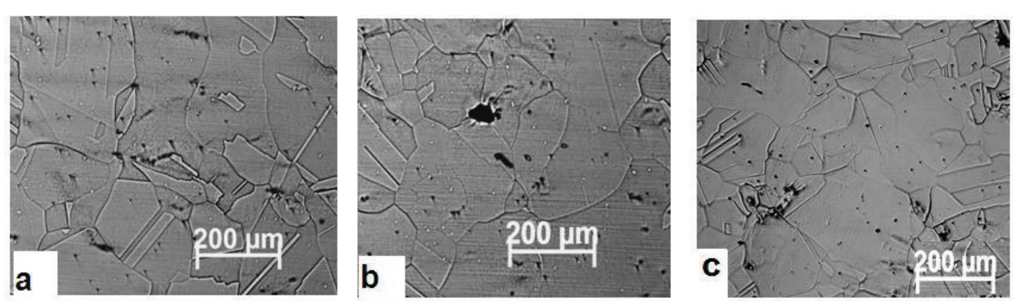

Figure 3.1 Microstructure of all three nitrogen variants (a) 8N, (b) 14N and (c) 22N

Tensile specimens of 4 mm gauge diameter and 28 mm gauge length along the rolling direction were machined [Fig 3.2] from the solution annealed material available in the form of plates. Tensile tests were conducted as per ASTM E8 [198] at a constant strain rate of $3x10^{-3}s^{-1}$ using tensile testing machine, 100 kN capacity with high temperature accessories. Tests were conducted at 300, 653 and 823 K for all three nitrogen variants which cover the FCG testing temperature range. The test temperature was controlled to ±2 K. The tensile test results are presented in Table 3.2.

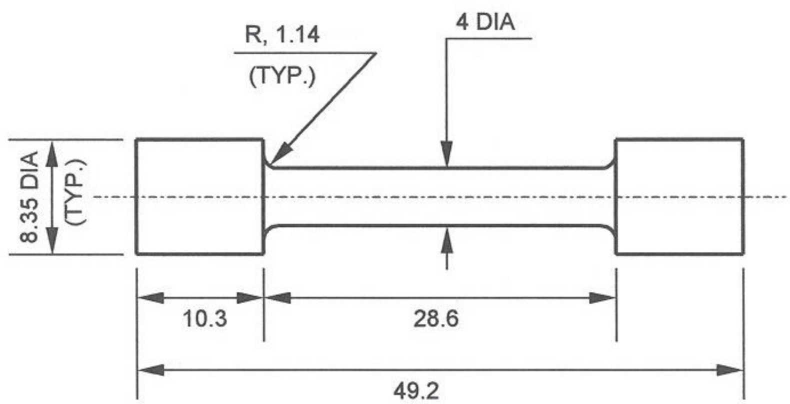

Figure 3.2 Schematic drawing of tensile specimen

Table 3.2 Tensile properties of SS 316L of different nitrogen levels

Nitrogen content (wt%)	Test temperature (K)	Yield strength (MPa)	Tensile strength (MPa)	Uniform elongation (%)	Total elongation (%)
0.08	298	290	595	53.0	66.0
	653	147	450	27.0	34.0
	823	146	417	24.0	32.0
0.14	298	328	670	40.0	57.0
	653	164	500	31.5	40.5
	823	150	463	27.0	35.0
0.22	298	369.	714	33.0	46.0
	653	218	580	32.0	38.0
	823	186	510	31.0	36.0

The 8N plates were used for the study on FCG behavior of welds. Weld pads of dimensions 500x400x30 mm^3 were fabricated by manual metal arc welding (MMAW) using indigenously developed electrodes. The schematic of weld pads and the orientation of test samples are presented in Fig. 3.3. The welding parameters are given in Table 3.3. The chemical composition of the weld deposit is given in Table 3.4. Since the carbon content in the weld is about 0.05 wt% (to match the creep strength of the weld with that of the base), which is higher than the limit (<0.03 wt%) for low carbon grade, it is designated as SS 316(N) weld. The image of the weld presented in Fig 3.4 shows the different weld passes and it generally consists of about 6 FN δ-ferrite of vermicular morphology distributed uniformly in the γ matrix. X-ray radiography of the weld was carried out to ensure that the welds are free from detectable defects like microcracks, porosity, and slag inclusions. The tensile properties of welds are presented in Table 3.5.

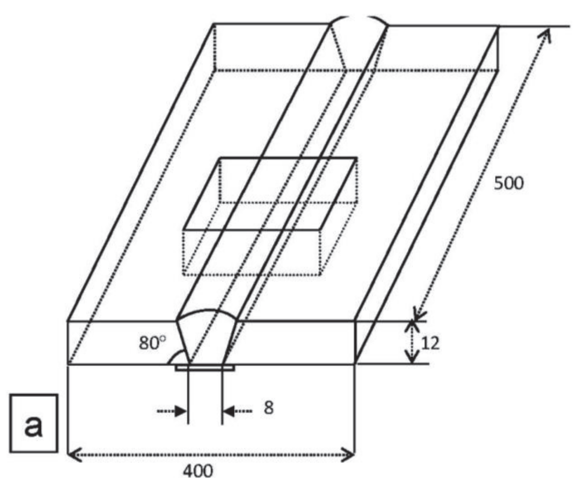

Figure 3.3 Schematic view of weld pad along with CT blank embedded

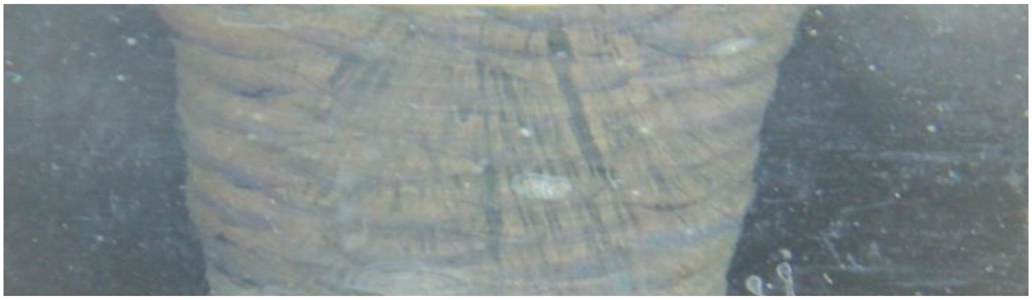

Figure 3.4 Image of Weld metal shows the different layers of weld beads

Table 3.3 Details of the preparation of weld pads

Consumable	SS 316(N) Electrode ϕ 3.2 mm Basic coated	**Inter-pass temp.**	393-423 K
Process	Shielded Metal Arc Multi passes (~30)	**Arc characteristics**	110-120A, 22-24 V
Joint Design	10°Single V-groove	**Travel Speed Heat input rate**	2.75-3.0 mm/s 0.84-1.04 kJ/mm

Table 3.4 Chemical composition (wt%) of the base and weld metals

Designation	C	N	Mn	Cr	Mo	Ni	Si	S	P	Nb	V	Fe
SS 316L (N) Base metal	0.027	0.08	1.70	17.53	2.49	12.20	0.22	0.0055	0.013	-	-	Bal.
SS 316 (N) Weld metal	0.05	0.08	1.4	18.5	1.9	11.15	0.46	0.006	0.025	<0.07	0.075	Bal.

Table 3.5 Yield strength and UTS of SS316 (N) weld of 8N

Test temperature (K)	Yield strength (MPa)	UTS (MPa)
298	466	658
653	299	481
823	228	428

The variation in hardness along weld root, cap side and longitudinal of the plate was examined. Vicker's hardness measurements were done in the transverse direction across the base and the weld region covering both the cap side location (C-L) and the root side locations (R-L). Several measurements were made along the length of the weld using a microhardness tester (Model EW-423 DAT) having a capacity of 0.01-2.0 kgf. Vickers hardness of the specimen was measured by using 0.5 kg load for 10 s. The results are presented in the running chapters.

SS316LN (14N) material available in the form of plates were used for the present study in order to evaluate the effect of cold work on the fatigue crack growth behaviour. The cold working was done in a 1 meter rolling mill. The plates were cold worked for 5, 10 and 15 % levels. The % of cold work was calculated based on the reduction in thickness. The required thickness reduction was achieved by 3 or 4 rolling operations.

3.2 Sample fabrication

3.2.1 Base material specimens

From the 30 mm thick plates, CT blanks of dimensions $70x65x30mm^3$ were cut and further machined to 20mm thickness blanks. From these blanks, the compact tension (CT) specimens were fabricated in TL orientation with width (W) of 50 mm. The notch of the CT specimens was prepared using electric discharge machining process. The other surfaces were ground to achieve a surface roughness better than 5-10 μm. Small impressions were made over the crack mouth opening side to place the DCPD leads for current input and voltage measurement as can be seen in Fig 3.5.

The specimens for room temperature and high temperature studies differ slightly since the load-line displacement gage for the former requires sharp knife edges to be seated properly, and for the latter needs slightly rounded geometry.

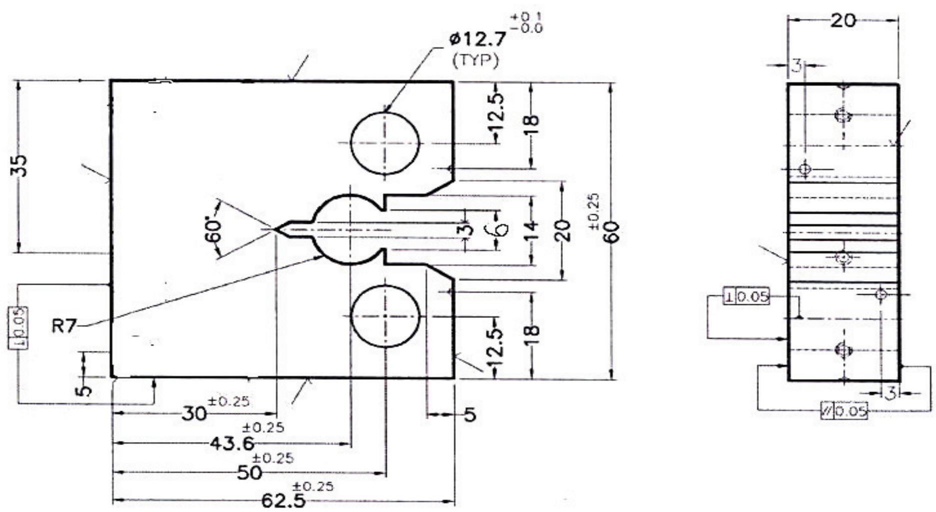

Figure 3.5 General compact tension (CT) sample drawing for FCG tests

3.2.2 Weld material specimens

Specimen blanks of 70×65×30 mm^3 were extracted from the weld pads avoiding the regions of any defects detected by radiography. Care was taken to ensure that the welded portion is approximately in the centre of the blanks. The CT specimens of 20 mm thickness were fabricated as shown in Fig.3.5. aligning the centre lines of the weld metal and the specimen. The notch was cut using the electric-discharge machining (EDM) along the welding direction ensuring that the crack plane is in the centre of the weld metal region.

3.3 Crack growth measurement

Direct Current Potential Drop (DCPD) was used in the present study for online measurement of crack length during FCG tests. It is a technique that involves the passage of a constant direct current through a specimen and measurement of the voltage generated across the crack mouth. The crack length was correlated to the change in the voltage measured across the crack site during its growth. Four lead wires were welded on to the specimens; two serve the purpose of current input while the other two measures the output voltage generated. For high temperature tests, the measurement lead wires should be made of same material as the test specimens, in order to avoid errors in the measurement of crack length due to any thermal emf generated. The DCPD values were measured intermittently at various stages of testing in order to determine the crack growth. The DCPD current path in the CT specimen and its setup with leads welded to the sample are shown in Fig 3.6. The DCDP leads are covered with insulator material in order to prevent any error due to short circuit.

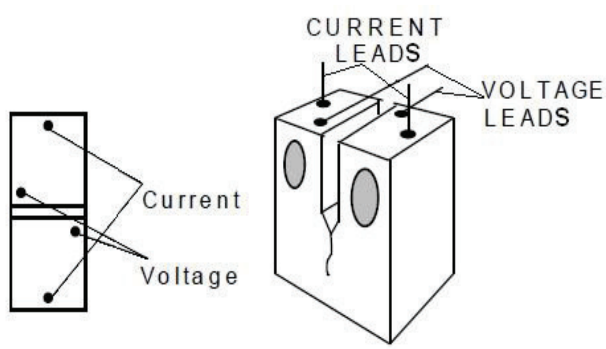

Figure 3.6 Schematic of CT specimen with DCPD leads

An important requirement for using DCPD for crack length measurement is its pre-calibration for the same specimen geometry as to be used in the test. In essence, the technique measures the resistance of the specimen as suggested in Gilbey and Pearson [199], where they developed a DC resistance method for measuring crack length changes in metal specimens during fatigue crack growth and this method was further developed for high temperature applications. The use of DCPD in measuring creep crack lengths has been reported by Siverns and Price [200], An earlier study in our laboratoryon J-Δa curves shows that the DCPD based and compliance based crack lengths are comparable [201]. DCPD method has been recommended for measuring crack length during fatigue crack growth tests [43].

The electrical voltage V is measured across the crack mouth and is related to the crack length. The electric potential across the crack mouth can be related to the unbroken crack ligament resistance, Ω, through the Ohm's law: $V = I \cdot \Omega$. With respect to a crack through a material of uniform thickness, a decrease in the un-cracked ligament (increase in crack length) increases Ω and the corresponding voltage output increases for a constant input current (*I*). That is $V/V_r = \Omega/\Omega_r$ where V_r is the reference voltage for a specimen with reference crack length and resistance Ω_r.

The voltage output is sensitive to the input current and the location of the current leads. In metals and metallic joints such as welds, slow crack growth can be measured using this DCPD method since the advancing crack faces increase in the specimen's electrical resistance to increase the voltage output. Hence a relation could be obtained between a/W and V/V_r. Calibration of the crack length with respect to the DCPD voltage is, therefore, necessary for different specimen geometry and location of the current and voltage measuring leads.

Nearly 15 number of CT specimens with identical initial notch and wire cut to different lengths were used for DCPD calibration. Lead wires were welded manually. Passing a constant current of through these specimens, the voltage output across the crack mouth was monitored at three different temperatures. For ambient temperature, the current used were 10, 15 and 20 A whereas at elevated temperatures 5, 10 and 15 A were used, since for the specimen geometry, a constant current of 20 A could not be stabilized. First specimen without wire cut was taken as the reference specimen and the initial voltage of that specimen was taken as reference voltage. It is noticed that initial notch length a_0 of the wire cut specimens vary due to specimen preparation methods and correspondingly the V_r reference voltage for the specimens could be different from that of the reference specimen. In such cases, a correction for the reference voltage has to be applied for calculating the correct V/V_r. This correction factor is proportional to the ratio of the initial a_0's of the wire-cut specimen to that of the reference specimen. The results for various temperatures are shown in Table 3.6. It is noticed that changes in current and temperature do not change V/V_r *vs* a/W relation obtained by polynomial fit as can be seen in Fig 3.7.

Table 3.6 Variation of V/V_r with a/W for different constant currents and temperatures

Sp No	Initial Notch Length a_0	Crack Length a	a/W	Correction Factor	V/V_r Corrected for initial crack length variation								
					RT			370 C			550 C		
					10A	15A	20A	5A	10A	15A	5A	10A	15A
0	19.701	19.701	0.3940	1	1	1	1	1	1	1	1	1	1
2	19.605	21.939	0.4388	0.99513	1.038	1.03839	1.03887	--	--	--	--	--	--
4	19.593	23.932	0.4786	0.99452	1.08159	1.08236	1.08545	--	--	--	--	--	--
5	19.597	24.958	0.4992	0.99472	1.08934	1.08949	1.09043	--	--	--	--	--	--
6	19.714	25.972	0.5194	1.00066	1.13287	1.1334	1.13662	--	--	--	--	--	--
6a	19.695	25.97	0.5194	0.9997	1.0888	1.08814	1.08897	1.09218	1.09133	1.09141	1.09062	1.09116	1.09046
8	19.686	27.984	0.5597	0.99924	1.13815	1.13786	1.14556	--	--	--	--	--	--
10	19.583	29.945	0.5989	0.99401	1.19385	1.19455	1.19448	--	--	--	--	--	--
12	19.653	31.957	0.6391	0.99756	1.23608	1.23675	1.23725	1.24201	1.24177	1.24152	1.24206	1.24237	1.24183
14	19.622	33.955	0.6791	0.99599	1.30787	1.30891	1.30924	--	--	--	--	--	--
16	19.666	36.008	0.7202	0.99822	1.32022	1.32023	1.32004	--	--	--	--	--	--
16a	19.695	35.958	0.7192	0.9997	1.30058	1.30121	1.30165	1.30499	1.30481	1.30556	1.30306	1.30604	1.30493
18	19.623	37.935	0.7587	0.99604	1.33782	1.33741	1.33853	--	--	--	--	--	--
20	19.553	39.954	0.7991	0.99249	1.38748	1.38766	1.38875	--	--	--	--	--	--
22	19.631	41.965	0.8393	0.99645	1.46769	1.467	1.46851	--	--	--	--	--	--
25	19.602	44.948	0.8990	0.99497	1.61581	1.61584	1.61549	1.61825	1.61836	1.61783	1.61862	1.61898	1.61835

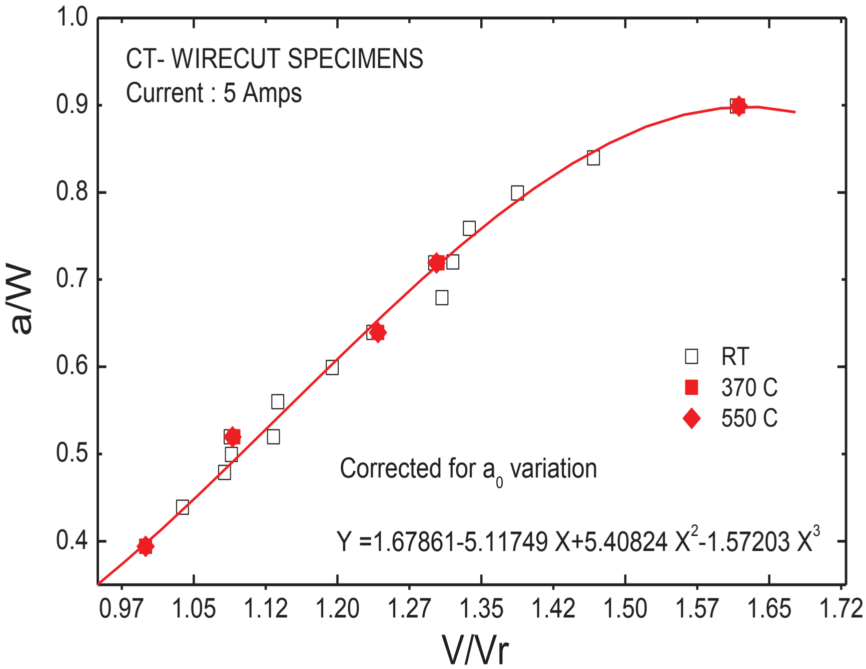

Figure 3.7 Correlation between crack lengths normalized by CT sample dimension *W* and voltage (normalized by reference voltage) at various constant currents and temperatures with R^2 value of 0.987.

A third degree polynomial curve was fitted to the a/W-V/V_r data for all the temperatures. The relation between crack length and voltage is as follows

$$^{a}/_{W} = B0 + B1\left(^{V}/_{V_r}\right) + B2\left(^{V}/_{V_r}\right)^2 + B3\left(^{V}/_{V_r}\right)^3.$$

The constants obtained were ($B0$=1.67861, $B1$=−5.11749, $B2$=5.40824 and, $B3$= −1.57203). This relation was used in the test application to measure the crack length automatically during the fatigue crack growth test as per the ASTM E 647 [43].

3.4 Fatigue Pre-Cracking

The CT specimens used for the FCG test were subjected to fatigue pre-cracking as per ASTM E-647 at room temperature to obtain a sharp fatigue crack ahead of the notch and also to ensure *a/W* ratio between0.45-0.55. Pre-cracking was done in load shedding mode using a resonance based fatigue machine of 20kN capacity, which is shown in Fig.3.8. According to the guidelines of ASTM E647, a pre-crack of length 0.1*B*, where *B* is the thickness of the specimen, or 1 mm is to be introduced in test specimen for FCG. The K_{max} in the finishing cycle of pre-cracking should be less than the initial K_{max} for the FCG test. DCPD measurements were made before and after pre-cracking. DCPD measurement before pre-cracking is the reference voltage V_r and the measurement after pre-cracking is called initial voltage (V_0).

The other conditions for the precracking is final ΔK and K_{max} values for precracking should be lower than the starting values for FCG test, whether it is *K* decreasing or increasing. Also, to avoid transient effects, there are other guidelines on step size of load reduction, crack increment in step etc. A load ratio (*R*) of 0.1 was used for all the pre-cracking in this work. The frequency of loading varied from 75 to 80 Hz during pre-cracking as the crack extended, since the resonant frequency depends on the elastic compliance of the system, including the specimen.

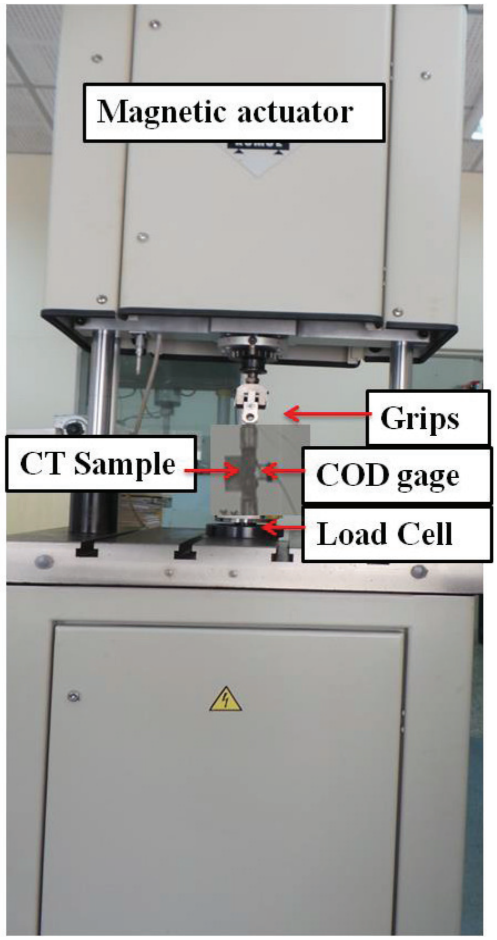

Figure 3.8 Resonance based pre-cracker and FCG test system.

3.5 Fatigue crack growth testing

Fatigue crack growth tests were carried out using CT specimens at room temperature (RT) and high temperature (HT) in a fully automated closed loop, servo-hydraulic testing system (Fig. 3.9 (a) and (b)) with a load capacity of 50kN. The test set up, control, data acquisition and online processing of the data to display the progress of the tests were achieved through the application software. The tests to determine the threshold stress intensity factor range (ΔK_{th}) were carried out with $\Delta K = \Delta K_o . e^{C(a-a_o)}$ condition as per ASTM E647 guidelines, where C = -0.08 for decrease in ΔK *(for threshold)* and + 0.08 for increase in ΔK *(for Paris regime)*, a_0/a initial/actual crack length and ΔK_o is the initial ΔK. A sinusoidal waveform was used for all the tests. A loading frequency of 15Hz was employed for all the tests, except those for evaluating the frequency effects. Other test frequencies employed in tests carried out on the servo hydraulic machine were 0.75 & 5 Hz. A few tests were carried out at 75 Hz, for which the resonance fatigue machine that was used for pre-cracking was employed. FCG tests at R values ranging from 0.05 to 0.75 were carried out, though for the basic tests, R=0.1 was chosen as recommended in the codes for design data generation.

To monitor crack growth during the test, DCPD was connected to the loaded specimen through leads which were spot welded. SS 316LN filler wires of 1.5 mm diameter were used as the leads in order to avoid any errors due to thermal emf. For high-temperature fatigue tests, a furnace with resistance heating was used in this study as shown in Fig 3.9 (a and b). It is a three zone furnace for temperature range from 100 to 1000 °C with an accuracy of ± 2 °C, and digital display of the test temperatures from all the temperature zones. The power supply for the furnace is 400 V / 50 Hz. The furnace was of split type and was provided with suitable ports for COD gage side entry. The DCPD leads were taken out through the bottom opening of the furnace close to the pull rods. High resolution crack opening displacement (COD) gauge was connected to the specimen (as shown in Fig 3.10) under fatigue loading in order to measure the load line displacement so as to determine the crack closure, as required by the standards. The COD gages used for the high temperature tests were different from those for room temperature tests. It has a provision for water-cooling and is mounted on the furnace with mounting brackets. A close view of the high temperature test setup with the furnace is shown in Fig. 3.9 (b).

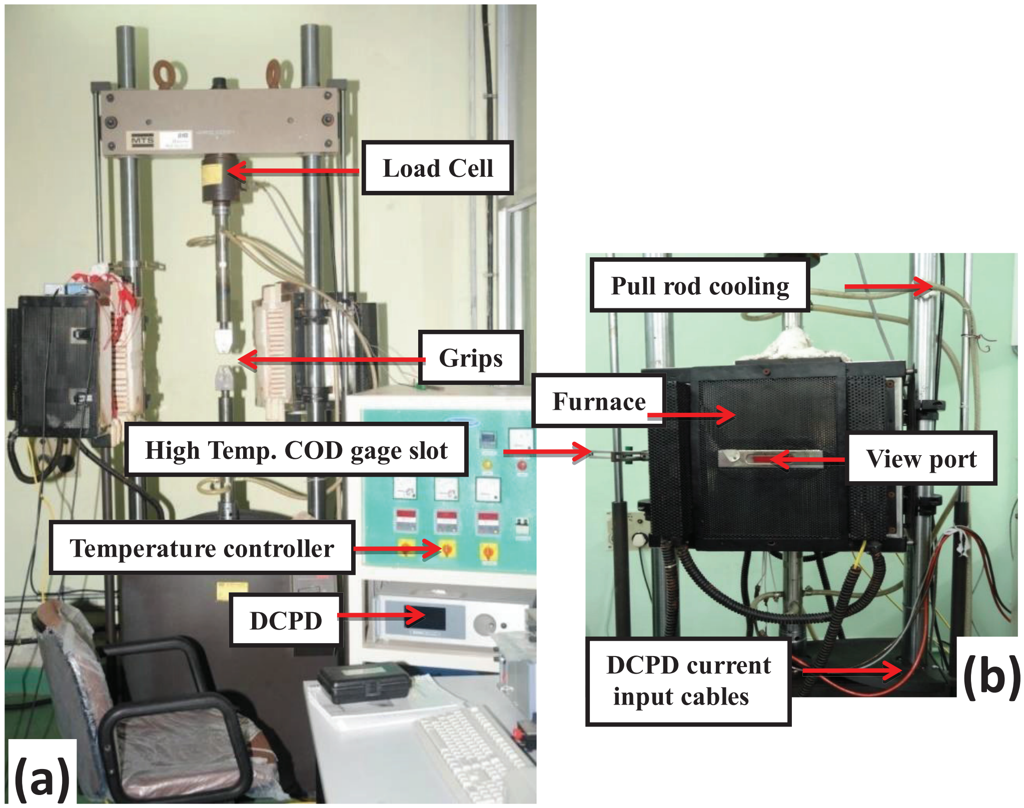

Figure 3.9 (a) Servo-Hydraulic FCG test system with (b) high temperature COD slot

Figure 3.10 High temperature COD gage mounted on to CT sample

3.6 Crack closure measurement

The opening and closing loads could be determined from the load (P) – displacement (δ) data as the deviation from linearity which determines the load at which crack opens fully in the loading part of the cycle (opening load, P_{op}) or starts closing in the unloading part of the cycle (closing load, P_{cl}). For this, after each da/dN calculation, it is a common practice to apply a few cycles of very low frequency, but with K_{min} and K_{max} values same as the current values in the FCG test, and collect P-δ data at sufficiently close intervals. In the present study, a slow ramp from P_{min} to P_{max} and back was used in order to acquire data at closer intervals, rendering the determination of the opening or closure loads more accurate. A schematic representation of the load cycle indicating the different parameters is given in Fig. 3.11 (a). Here, $\Delta P = P_{\max} - P_{\min}$, $\Delta P_{eff} = P_{\max} - P_{cl}$, where $\Delta P, \Delta P_{eff}$ are applied and effective load amplitudes, $P_{\max}$: Maximum load and $P_{\min}$: Minimum load. A typical P- δ plot is presented in Fig. 3.11 (b) with the deviation of the displacement from linearity indicated. Compliance offset [43] method was used to identify P_{cl} value which is the deviation from liniearity (marked) in Fig 3.11(b).

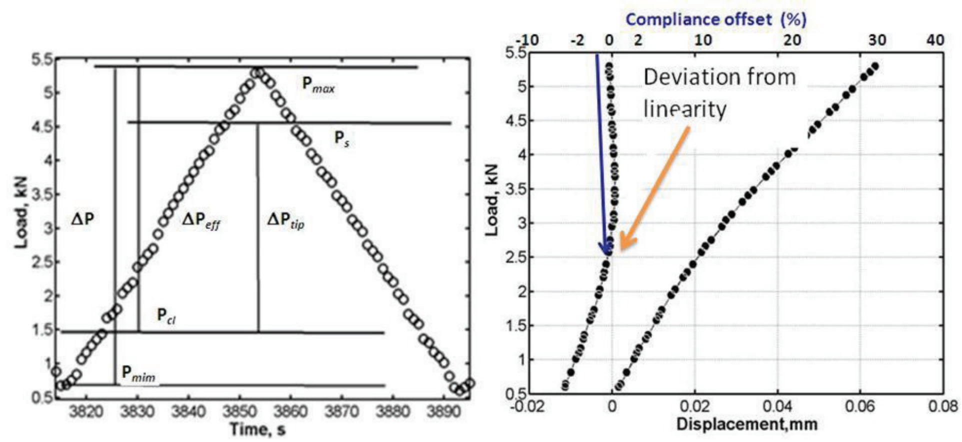

(a) **(b)**

Figure 3.11 (a) The load cycle indicating the different parameters, (b) Load – Displacement data for crack closure load measurement as per ASTM E 647 section X 2.7

This consists of the following. The load-displacement data is divided into small overlapping segments, each consisting of about 5 % of the cyclic range. Open crack complianceis determined from the clearly linear segment below the maximum load. In the paris regime, this usually happens below about 90% of the maximum load since local plasticity leads to small deviations from linearity. Compliance values from the small segments were also computed. Now, compliance offset (%) is determined as Compliance offset = (Segment compliance−open crack compliance)x100/opencrack compliance. From the plot of load vs compliance offset, the closure load is determined as the point where the compliance offset is 2%.

3.7 Optical measurement of crack size

Optical crack size measurement is important to ensure the correctness of crack length value obtained by DCPD. After fatigue crack growth test, the specimens were parted into two halves by using same servohydraulic machine to view the pre-crack, FCG and post fractured regions of the specimen. The high temperature tested specimens generally show the pre-cracked region clearly because of the formation of oxide layer. To clearly view the pre-cracked region in RT tested specimen, it was heat tinted, i.e., heated to 200 ºC, then cooled to ambient temperature before pulling open to two halves. The initial and final crack lengths were measured optically using a travelling stereo microscope by using 9 points average method specified in ASTM E-1820 [202]. The travelling stereo microscope used to measure the crack length is shown in Fig.3.12(a) and the normal features observed on the failed surface is shown in Fig 3.12(b). The optically measured value is compared with crack length value obtained from the test data in order to correct the differences exist if any.

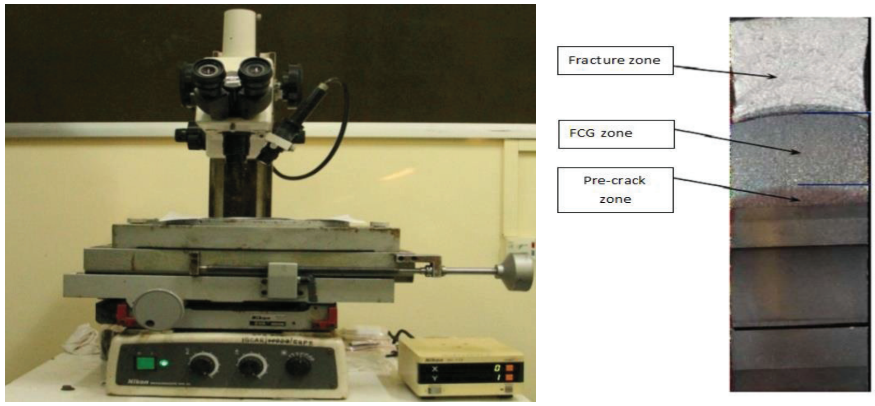

Figure 3.12 (a) Travel stereo microscope (b) Macro view of the fracture surface showing different regions of crack extension

If the deviation is more than 0.2mm in the crack length values obtained from optical microscope measurement and DCPD, the crack length should be corrected by interpolation method. Thus, the corrected stress intensity factor will be reported as per the ASTM E 647. The crack length measured using DCPD is verified with the optically measured value of initial and final crack length over the fracture surface. The *a* vs *N* data were processed for obtaining d*a*/d*N*, by adopting the seven point polynomial method. This method involves fitting a second-order polynomial to sets of (2*n* + 1) successive data points, where *n used* is 3. The polynomial constants were determined by the regression analysis over the crack length and number of cycles by fitting the data. The corresponding slopes were used for computing the crack growth rate (d*a*/d*N*) and corrected crack lengths were used of estimating the ΔK.

3.8 Characterization techniques used

3.8.1 Optical Microscopy

Samples with approximate dimensions of 10x10x5mm^3 from plates of 8N, 14N and 22Nwere prepared for optical microscopy by grinding using various grades of emery papers followed by diamond and colloidal solution polishing to obtain mirror finish. Electrochemical etching of polished specimens was done using 10 g oxalic acid in 100 ml water by applying 3 V for 90 s. Another reagent (HCl, HNO_3, and glycerol) was also used [203] for etching to reveal microstructural features such as grain boundaries, twins, precipitates etc. The samples were examined using optical microscope capable of magnification up to 1000X. These micrographs were used for grain size measurements too. For grain size analysis, linear intercept method was adopted.

3.8.2 Scanning Electron Microscopy

Fractographic examination of the FCG tested specimens was carried out using scanning electron microscopy. Samples for this were extracted from the tested specimens by cutting the tested specimens to about 10 mm depth from the fracture surface. These samples were subjected to ultrasonic cleaning to remove any extraneous particles from the fracture surface. Fractographic features were examined under a SEM (CamScan, model 3200) to study the nature of crack growth. The SEM is equipped with energy dispersive X ray analysis (EDAX) facility which was used to identify the nature of precipitate and particles observed on the fracture surfaces.

3.8.3 X-Ray diffraction technique (XRD)

The main objective of this XRD technique in this study was to identify the presence of deformation induced martensite transformation in different specimens subjected to cyclic loading under various conditions. Samples for this study were extracted from the fracture surface and subjected to XRD. XRD data were acquired on Inel make machine (Model-Equinox 2000) equipped with gas detection cell (argon and ethane) curved detector, and intensity measurements were taken using germanium monochromatic Co-Kα radiation (wave length, λ= 1.789 A) in asymmetric acquisition mode. The standard database (JCPDS) was used to analyze the XRD patterns.

3.8.4 Transmission electron Microscopy

Transmission Electron Microscopy (TEM) was carried out for selected specimens to observe the dislocation structures. The specimens were mechanically ground and polished to achieve 100 μm thickness using standard metallographic procedure. 3 mm diameter discs were punched out from the thin foil of polished specimens. Perforation was carried out by Struers Tenupol 5 double jet thinning in 10% perchloric acid and 90% methanol solution. The TEM examinations were carried out using Libra 200FE (Carl Zeiss) high resolution TEM operated at 200kV.

3.8.5 Magnetic measurement

The magnetic Atomic force microscope (AFM, NT-MDT make, and Model : NTEGRAPRIMA) was used for the detection and semi-quantitative evaluation of deformation induced martensite that formed close to the crack tip during the crack growth under cyclic loading. The technique employs a magnetic probe, which when brought close to a sample, interacts with the magnetic stray fields near the surface. The strength of the local magnetostatic interaction determines the vertical motion of the tip as it scans across the sample and reveals the magnetic phase present in the deformed region.

3.8.6 Residual stress measurement

The hole drilling method is used for measuring residual stresses [204] in the CT specimens of the welds before and after FCG testing. The experiments were carried out using the indigenously made deep hole drilling setup available at IIT-Bhuvaneswar. The through thickness residual stresses were measured by deep hole drilling method. The center reference hole was 15 mm away from the notch tip on the weld as shown in Fig. 3.13. The residual stresses were measured in notch direction (along the weld) and transverse to it at the reference point.

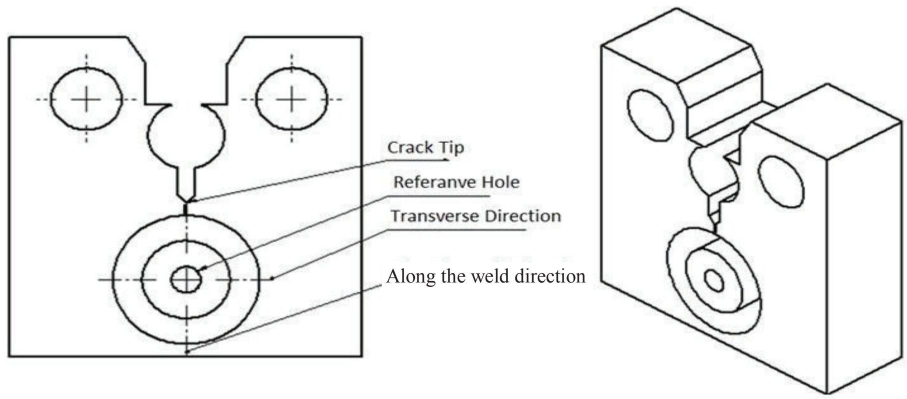

Figure 3.13 Hole drilling methods employed on the CT sample made from weld

3.9 Short fatigue crack growth measurement

In the present study, the short and long crack growth of SS316LN (8N) under cyclic loading in vacuum has been evaluated in the Scanning Electron Microscope fitted with a mechanical stage. CT specimens of width 25mm with initial notch of length 5mm were used. Specimens used were 2 mm thick for short crack growth and 6 mm for long crack growth. The CT specimens were fabricated by EDM wire cutting. Specimens for short crack growth studies, were not pre-cracked, while those for long crack growth measurements were precracked in a servohydralic machine before testing in the SEM chamber.

The notched CT specimen was loaded on to the mechanical stage as shown in Fig 3.14, which was then placed inside the SEM (CamScan make) chamber and a constant vacuum of 10^{-7} mbar was maintained. The temperature within the chamber is about 293 K. The sample was cyclically loaded with a frequency 0.5 Hz in vacuum to study the initiation of crack from notch. Further, more load cycles were given in order to observe the crack propagation in the SEM. To study the long crack growth, precracked CT specimens were loaded and placed inside the SEM chamber. Constant amplitude load cycling was applied to the specimen. As the crack propagated, this resulted in an increasing ΔK. Thus, profiles of the propagating fatigue cracks, both short and long, were monitored on the SEM screen. Results of both types of cracks were obtained by intermittent snap shots as well as continuously using a video system. Simultaneously, EBSD data also were acquired in order to study the association of crack growth with microstructural features as well as for *in-situ* observation of DIMT close to the crack tip. The crack length (a) *vs* number of cycles (N) data were analysed as in the case of conventional tests to obtain the FCG curves.

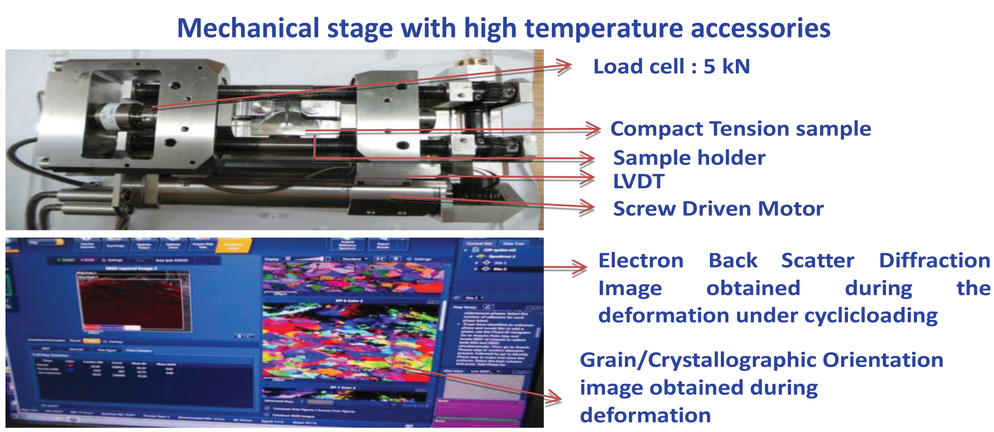

Figure 3.14 Mechanical stage for FCG test attached to SEM for in situ observation of crack growth

CHAPTER 4

EFFECT OF TEMPERATURE ON THE FCG BEHAVIOUR OF SS316L (N)

CHAPTER 4: EFFECT OF TEMPERATURE ON THE FCG BEHAVIOUR OF SS316L(N)

4.1 Introduction

In this chapter, the investigation on the fatigue crack growth (FCG) behaviour of austenitic stainless steel SS316L(N) with 0.08 mass% nitrogen (8N) is discussed. Conventional FCG analysis incorporating the crack closure effects is carried out to examine the effect of test temperature on the FCG behaviour. An attempt is made to examine the results on temperature dependence of FCG in terms of high temperature phenomena such as oxide-induced crack closure, creep, dynamic strain ageing etc. Tests were carried out at different frequencies to throw more light on the mechanisms influencing FCG at different temperatures. A cursory look at the possibility of deformation induced martensitic transformation contributing to FCG resistance at ambient temperature has been made. The inherent inadequacies associated with the conventional FCG analysis have been identified, which led to a more detailed study on this aspect in later chapters.

4.2 Fatigue Crack Growth Studies of SS316LN at room temperature

The extensive literature survey and in-house experience indicate that the austenitic stainless steel of type SS316LN has potential application for the high temperature components of sodium cooled Fast Breeder Reactors (FBR) [7, 12] and various other industries at different temperatures and environmental conditions. It is chosen as the major structural material for several high temperature components of PFBR which is in advanced stage of commissioning at Kalpakkam. For the damage tolerant design [90, 91] of components made of this steel, *inter alia* its FCG properties at different temperatures are necessary. A preliminary study was carried out at temperatures ranging from 300 - 823 K to evaluate these properties for the SS316L(N) with 0.08 mass% nitrogen (referred to as 8N here). The crack closure contributions were evaluated and the effective threshold $\Delta K_{eff,th}$ and the Paris regime properties using ΔK_{eff} as the driving force were determined as suggested in the ASME [90] and RCC-MR [91] codes. In order to understand the observed behaviour better, further tests were carried out at different frequencies and testing modes.

As already presented in the earlier chapters on literature survey and experimental details, the FCG behaviour of any material is presented in terms of crack growth rate (da/dN) against the applied stress intensity factor range (ΔK) known as FCG curves, which have different crack growth regimes named as Threshold, Paris and Unstable regimes [24, 25].Threshold and Paris regimes have practical relevance to structural integrity assessment. Hence, further discussion is limited to these two regimes and the effects of various parameters on the FCG behaviour are discussed in the following.

The Paris regime is considered to be generally less sensitive to microstructure, whereas, the microstructure, cold work level, environment, temperature, load ratio, crack closure, overloads, etc are found to influence threshold regime. The results of the preliminary investigation carried out on the FCG behaviour of SS 316 L(N) at room temperature in both threshold and Paris regimes are presented in Fig 4.1. The FCG results of SS316LN without and with incorporating crack closure effects are shown in this figure. The effective threshold stress intensity factor range ($\Delta K_{eff,th}$), i.e., after correcting for crack closure was found to be 4.5 MPa.m$^{1/2}$. As can be seen from Fig 4.1, the extent of crack closure increases with decreasing applied ΔK. However, at an applied ΔK of about 7 to 7.5 MPa.m$^{1/2}$ in the transition regime between Paris and threshold regimes, an increase in crack growth rate is observed. Just around the same regime, 7.5 to 10 MPa.m$^{1/2}$, there is a decrease in closure contribution too. This points to the presence of a toughening mechanism reducing the crack growth rate in spite of the high ΔK_{eff} which vanishes below 7.5 MPa.m$^{1/2}$. Maximum difference between the ΔK and ΔK_{eff} curves, i.e., maximum contribution from the crack closure, is observed at an intermediate ΔK= 10 MPa.m$^{1/2}$. Generally, FCG thresholds are governed by the local deformation mechanism at the crack tip and the extent of crack closure. Based on the previous studies [30, 31, 63], different crack closure mechanisms may play significant role over the crack growth behaviour. The possible mechanism which might have influenced the crack growth rate has been examined in the following. First, the plasticity induced crack closure, it has been shown by different researchers that plasticity induced crack closure prevails at near-threshold regime [31,63]. However, near the threshold, the crack growth rate is very low due to the low loads. It has been observed that in the near-threshold regime, plane strain situation prevails and hence the plasticity induced crack closure, if any, is limited [65, 66]. Another alternative is the roughness induced crack closure, which stems from the faceted type of crack growth in the low SFE materials. In the tests at 300 K, oxidation induced closure will not be significant. Therefore, it may be anticipated that the crack closure in the present case is induced by both plasticity and roughness. However, based on theory of dislocations [66], these mechanisms have been discounted [189]. Also, these mechanisms are expected to give rise to a monotonic change in the extent of closure with applied ΔK, where as a non-monotonic variation in the extent of closure is observed in the present case.

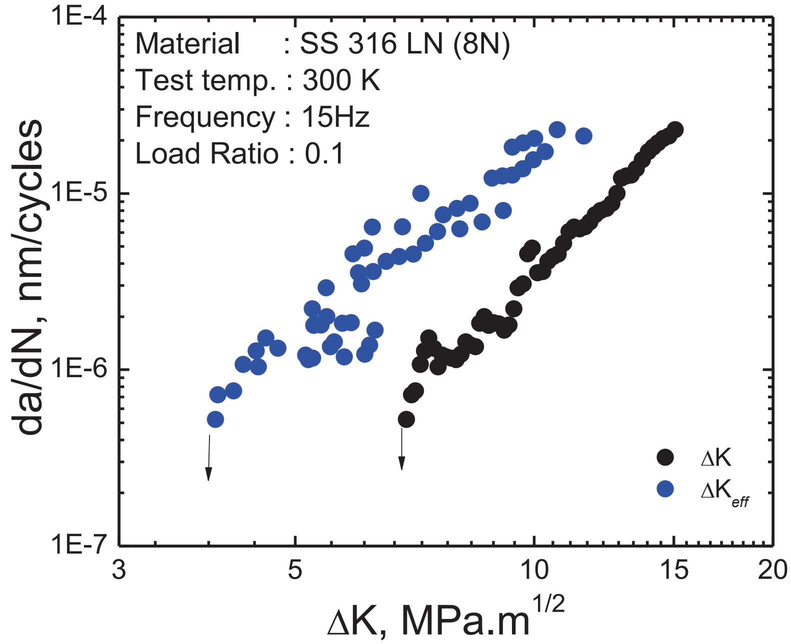

Figure 4.1 FCG behaviour of SS316LN without and with crack closure correction

The austenitic stainless steels are prone to deformation induced martensite transformation (DIMT) under cyclic and monotonic loading at and below ambient temperature. Therefore, it can be anticipated that there is a possibility of DIMT playing a role in the observed FCG behaviour. The extent of DIMT is found to vary with the applied stress, strain rate and temperature. Recent studies on stainless steels [142-144] indicate that DIMT influences the crack growth rate not by contributing to the crack closure but by enhancing the intrinsic crack growth resistance of the material. The present study attempts also to address this aspect through FCG tests conducted at constant K_{max} in ΔK decreasing mode. In this test, crack closure measurements were not made.

In the ΔK decreasing test with constant K_{max}, the K_{min} and R keep increasing as the test progresses towards the threshold region where the closure effects are said to be prominent in constant (low) R tests. The starting R value was about 0.11 and it increased to 0.64 at the end of the test. Therefore, the effects of crack closure also decreases progressively. Thus, the results of this test are not influenced by closure when the R value becomes 0.5 [65]. Thus the data in the near threshold region are expected to be free from crack closure. The FCG results for SS316L(N) -8N from constant K_{max} test are superimposed over the data for constant R (=0.1) tests with and without crack closure correction in Fig. 4.2. The initial data without closure correction in the Paris regime from both the tests nearly coincide with each other as expected. Since R increases during the test, the data for constant K_{max} should be moving towards the closure-corrected data for constant R test and match with it in the near-threshold regime. However, the constant K_{max} test suggests a better FCG resistance than the closure corrected data from constant R test. In an intermediate regime, the difference is minimum. It appears that the latter underestimates the crack growth resistance; however, may be preferred for a safer integrity assessment since it is more conservative, as long as the reason(s) for the observed differences are not understood clearly.

It may be noted that the crack closure is determined using the compliance method, i.e., beginning of crack closure in the unloading segment/full opening of crack in the loading segment of the cycle is identified as the point where there is a deviation from linearity in the load (P) versus load-line displacement (d) plot. It is possible that this procedure has overestimated the crack closure or opening loads leading to underestimation of the crack growth resistance. Sadananda et al [66] have questioned associating crack closure with the deviation from linearity in the *P-d* plots.

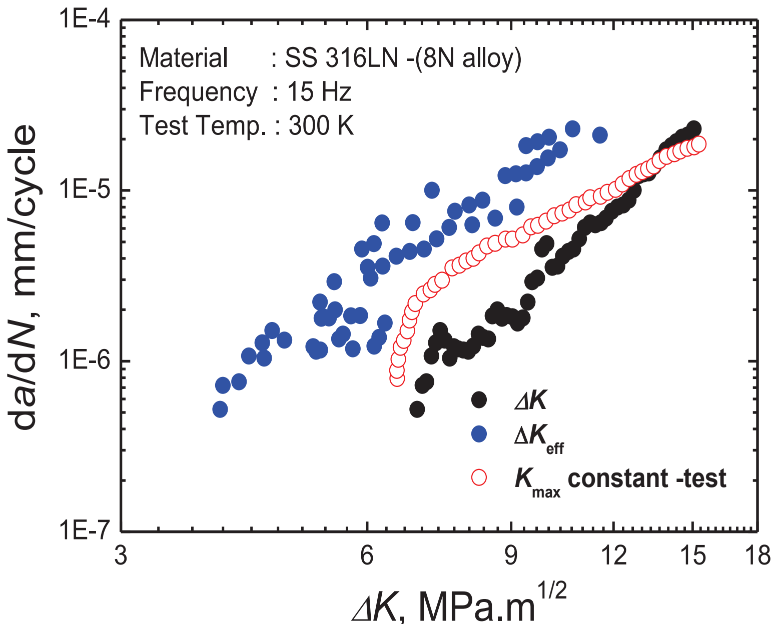

Figure 4.2 Effect of K_{max} on the FCG behaviour of SS316L(N) in ΔK decreasing test. The solid symbols are the data from constant R (= 0.1), in which both K_{min} and K_{max} decrease as the test progresses. The open symbols are for K_{max}constant test in which K_{min} and R increase as the test progresses.

From the above results, it appears that the closure-corrected FCG data for SS316L(N) from constant R test show an intermediate region with low levels of crack closure, which is not in the expected trend. The constant K_{max} test data shows the smallest difference with the constant R data in the same region. This can happen if DIMT which is found to occur in this class of steels during cyclic loading causing transformation toughening, and vanishing at sufficiently low ΔK, plays a role in the observed behaviour. Studies with material and/or test conditions which can lead to different extents of DIMT will help answering this question which is further examined in the next chapter (Chapter 5). In this chapter, this is not further discussed and the focus here is restricted to the FCG behaviour of 8N steel at different temperatures using conventional crack growth analysis.

4.3 Fatigue Crack Growth Studies of SS316LN at high temperature

Many of the SS 316L(N) components in PFBR are exposed to temperatures in the range 623-823 K during the reactor operation. The preexisting flaws or those generated during service under such conditions can grow due to the flow induced vibrations and thermal fluctuations experienced during the service. In order to avoid catastrophic failure due to crack growth by taking appropriate action, periodic inspection and integrity assessment of the components are necessary. For integrity assessment as well as to decide on the appropriate inspection intervals, the FCG properties of the material at the relevant temperatures are essential. Hence, FCG tests were carried out on the 8N variant of SS316L(N) at various elevated temperatures between 300 and 823 K. Effects of test temperature on the FCG behaviour of SS316LN-8N in both threshold and Paris regimes are discussed in the following sections.

4.3.1 The Paris regime

The FCG results in the Paris and threshold regimes for 8N at different test temperatures in the range 300-823K are presented in Fig 4.3 without crack closure correction. Further, Paris and threshold results have been discussed seperately in the following sections. Fig. 4.4 shows the Paris regime after incorporating crack closure correction. It is observed that crack growth rate increases with temperature at a given ΔK except at 723 K, where it falls below the values at 623 K. The difference in the crack growth rate is high at low ΔK (< 25MPa.m$^{1/2}$) levels when compared to high ΔK. However, the FCG rates at 673 and 723 K are of the same order in the ΔK range 10-30 MPa.m$^{1/2}$. After crack closure correction, despite the high scatter, it is clear that the difference in FCG curves at different temperatures are higher, presumably due to the higher extents of closure with increasing temperature. Further, it is noticed that FCG data for the temperature range 673 - 773 K are overlapping.

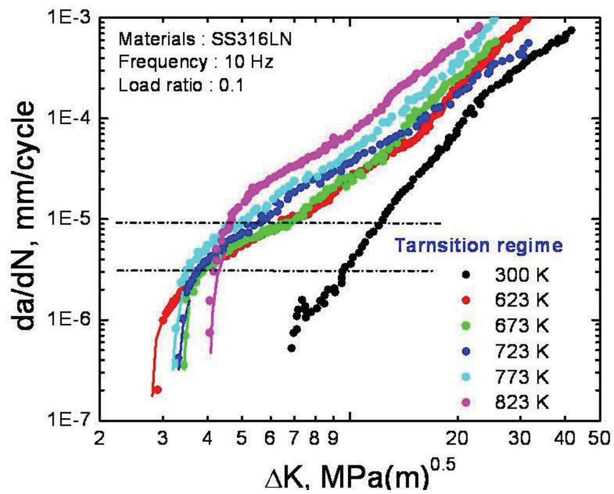

Figure 4.3 Effect of test temperature on the FCG behaviour of SS316L(N)-8N without crack closure correction in Paris and threshold regime

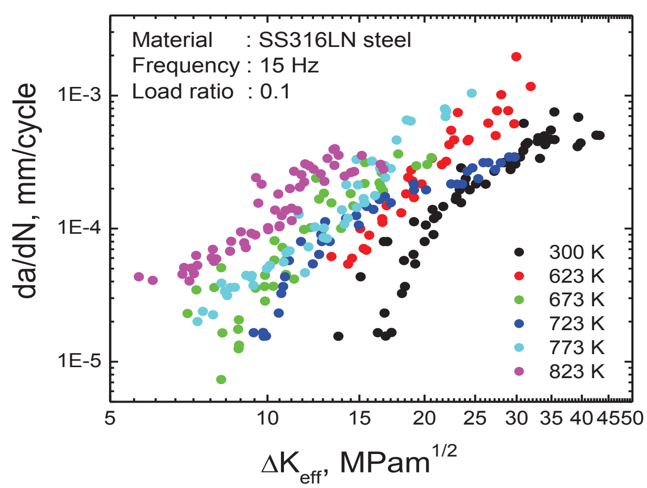

Figure 4.4 Effect of test temperature on the FCG behaviour of SS316LN (8N) after crack closure correction

Table 4.1 Paris parameters at different temperatures for 8N steel using ΔK and ΔK_{eff} for correlating

Temperature, K	ΔK		ΔK_{eff}	
	m	**log(*C*, nm/cycle) nm/cycles**	***m***	**log(*C*, nm/cycle) nm/cycles**
300	3.4721	–2.7053	3.3079	–2.3919
623	3.9264	–2.8442	3.7494	–2.4943
673	3.8369	–2.5510	3.3450	–1.7057
723	3.8311	–2.5160	2.8471	–1.0956
773	3.4288	–1.8217	3.2886	–1.5712
823	2.3766	–0.5106	2.5518	–0.4478

The FCG parameters for the 8N steel in the Paris regime are presented in Table 4.1. A general trend of increasing log*C* and decreasing *m* with temperature is evident from the plot of the same data in Fig. 4.5. It is seen that there is a small increase in log *C* while *m* remains constant in the range 623-723 K when crack closure is not accounted for, i.e., when applied ΔK is used for correlation. At higher temperatures, the increase in *C* and decrease in *m* are quite significant and compliment each other as has been reported for several materials. In an earlier study on P91 steel, a similar deviation from the complimentary variations in *C* and *m* at an intermediate temperature was reported for the steel in normalized and tempered condition by Nani Babu et al [95]. For the same steel in aged condition, the data for the intermediate temperature was in line with those for the other temperatures. Based on this observation, the deviation was ascribed to DSA effects. Variation of log*C* and *m* with temperature from the present data after closure correction shows a clear deviation from the general trend in the range 623-723 K. The general increase in log*C* with temperature (Table 4.1) is a consequence of the temperature-dependent decrease in the strength of the material, while the decrease in *m* at high temperature, i.e., lower sensitivity of the crack growth rate to ΔK, indicates the increased significance of thermally activated mechanisms in damage accumulation. However, at intermediate temperatures, the phenomenon of dynamic strain ageing (DSA) plays a major role in deciding the crack growth behaviour. This will be further examined in section # 4.5.

The temperature-dependence of crack growth behaviour may be linked to those of the basic mechanical properties, viz., Young's modulus (E), yield strength (σ_{ys}) and ultimate tensile strength (σ_u). Therefore, it appears that the temperature dependence of FCG rate can be rationalised by taking in to account the temperature dependence of these properties (Table 4.2)

Table 4. 2 Tensile properties of SS 316L(N) at different temperatures

Temperature, K	300	623	673	723	773	823
E, GPa	200	172	168	164	159	155
σ_{ys}, MPa	290	160	155	163	147	146

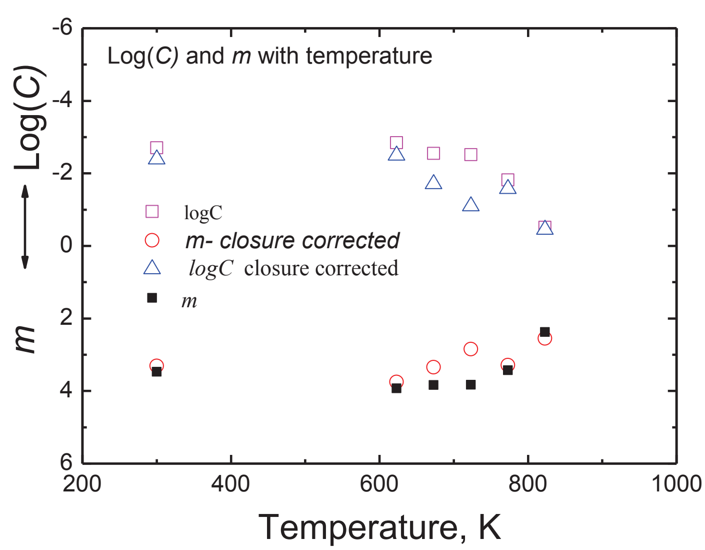

Figure 4.5 Effect of temperature on the Paris parameters for SS 316LN (8N)

Attempts have been made to establish an empirical relation of da/dN for different temperatures with the normalized driving force parameters. The concept of using normalized stress intensity factors for correlating FCG data was initially introduced by Pearson [205] and applied to various materials at ambient test condition [206]. Considering that K is an LEFM parameter, the temperature dependent E has been chosen as one of the normalising parameters. The FCG curves in terms of normalized (with E) driving force are presented in Fig 4.6. It is obvious that the FCG curves for all temperatures lie in a relatively closer scatter band than in Figs. 4.3 and 4.4; however, the temperature dependence and the anomaly in the range 673-773 K still remain. It indicates that while E does influence the crack growth behaviour, its role is not significant. These observations are in agreement with previous reports [205, 206] that the variations in elastic modulus cannot account for the differences in FCG rates for different materials. Recalling that 673 - 773 K is the peak dynamic strain ageing (DSA) temperature range for the present steel [123], and a peak or plateau in σ_{ys} is one of the manifestations of DSA [207], σ_{ys} has been chosen as another normalising parameter. It may also be recalled that the crack tip plastic zone size (r_p) is an important parameter in FCG and it is a function of applied ΔK and σ_{ys}; $r_p = \frac{1}{2\pi}\left(\frac{\Delta K}{\sigma_{ys}}\right)^2$. Therefore, it is appropriate to consider the possibility of accounting for the temperature induced variations in FCG data by normalising ΔK with σ_{ys}. The results are presented in Fig. 4.7; the FCG data for all the test temperatures except for 723 K, lie in a single scatter band. Thus, expressing FCG data in terms of $\Delta K/\sigma_{ys}$ rather than $\Delta K/E$ appears more appropriate.

A Paris type relation exists between da/dN and $\Delta K/\sigma_{ys}$. $\frac{\mathrm{d}a}{\mathrm{d}N} = C \cdot \left(\frac{\Delta K}{\sigma_{ys}}\right)^m$ with C = 4.5 nm/cycle and m = 2.73. Interestingly, this exponent is close to 3, the value expected from theoretical considerations for metals and alloys [73].

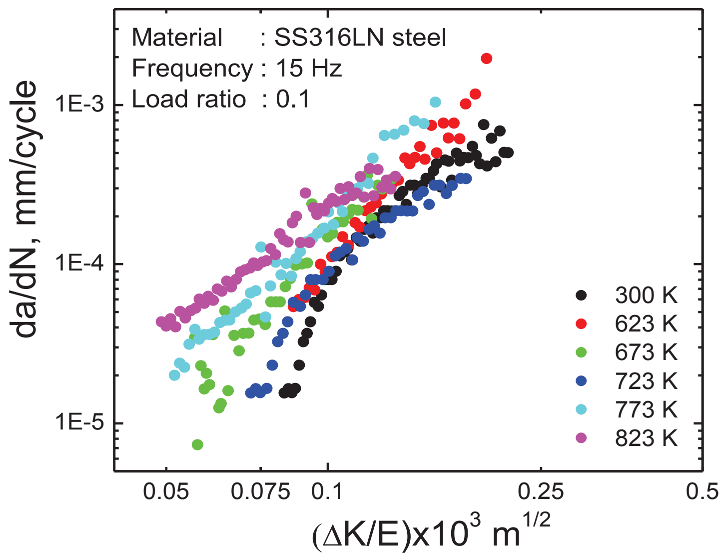

Figure 4.6 Effect of test temperature on the FCG behaviour of SS316LN after normalization with Young's modulus.

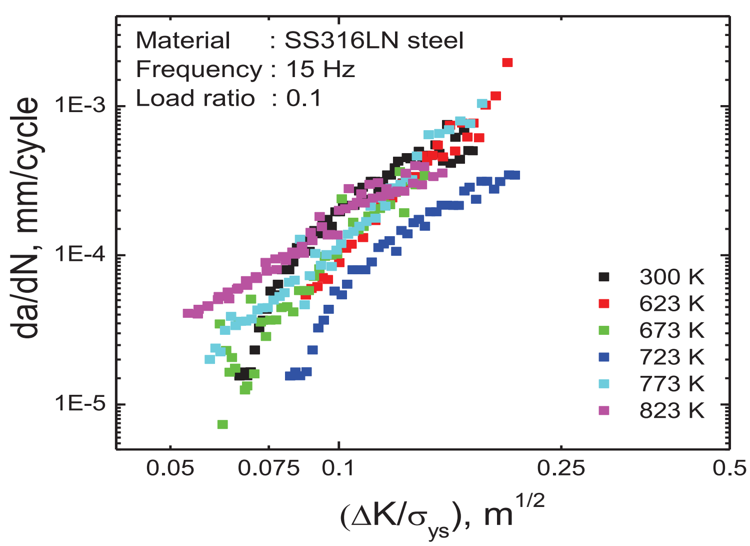

Figure 4.7 Effect of test temperature on the FCG behaviour of SS316LN after normalization with yield strength

4.3.2 The threshold regime

In threshold regime, the crack growth is more sensitive to the several factors including the test temperature. Effect of test temperature on the FCG behaviour of SS316LN-8N in the threshold regime is discussed in the following. The FCG results for the test temperature range 300-823 K at load ratio 0.1 and frequency 15Hz without and with crack closure correction are presented in Figs. 4.8 and 4.9 respectively. The crack growth rate increases with temperature; for example at a ΔK=8 MPa.m$^{1/2}$, a 10 fold increase in the crack growth rate for a change in temperature from 300 to 673 K is observed. However, increase in crack growth rate with further increase in the test temperature is limited as can be seen in both the figures (Figs.4.8 and 4.9). From Fig. 4.8, it is observed that there is a sharp change in the slope of the FCG curves for elevated temperatures except at 823 K. The value of ΔK at which this occurs decreases with increasing temperature. Also, there is a tendency of these curves to bunch together in the threshold region.

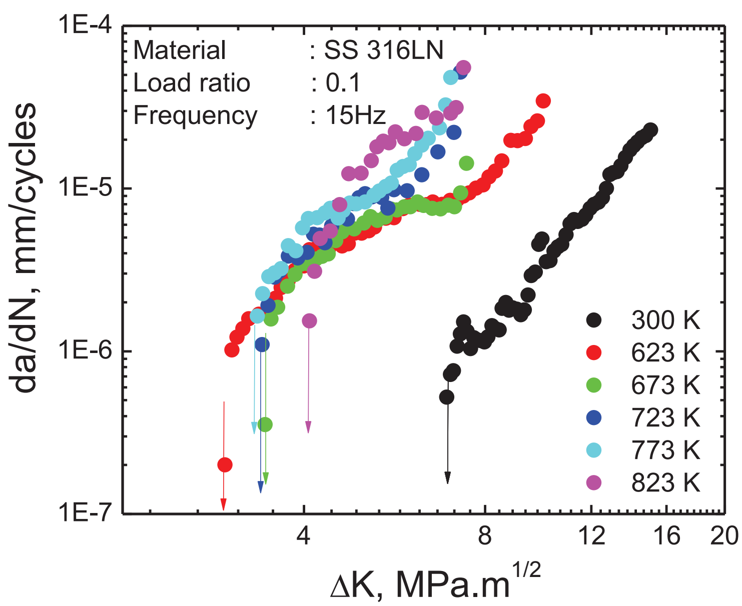

Figure 4.8 FCG results of SS 316LN-8N at different temperatures in the range 300-823 K

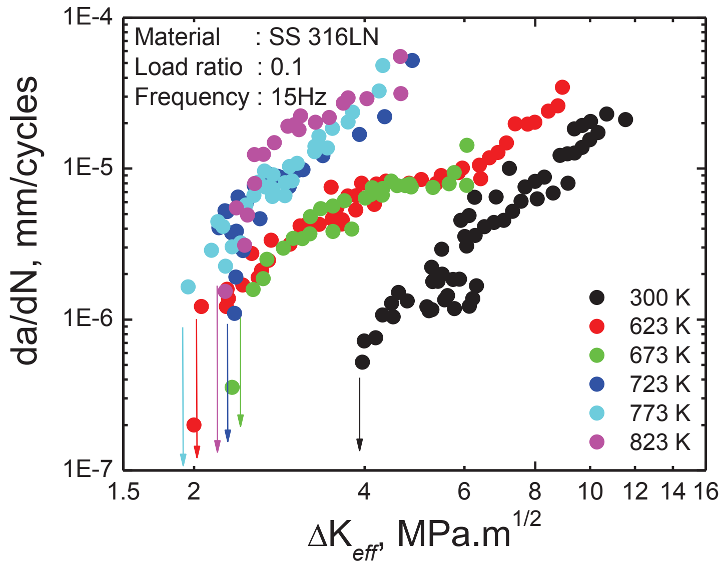

Figure 4.9 FCG results of SS 316LN-8N after crack closure correction at different temperatures in the range 300-823 K.

Even beyond the threshold, 623 and 673 K data are in the same band where as 723 and 773 K form another scatter band. It is likely that the onset and disappearance of DSA causes this slope change. The change of slope in the FCG data for a temperature at a particular ΔK may also be associated with the disappearance of DSA. It may be noted that DSA depends not only on temperature, but on strain rate too. Since these tests are done at constant frequency, the strain rate decreases with decreasing ΔK and it is likely that it falls in to the DSA range of strain rate for that particular temperature. An attempt to determine the activation energy for the rate controlling mechanism for DSA based on the temperature dependence of ΔK values at which slope change occurs, is presented in section # 4.5, where DSA phenomenon is dealt with in more detail.

In addition, Fig. 4.9 shows that there is a grouping of FCG data after crack closure correction, that is, (i) 623-673 K data form one group, (ii) 723-823 K data fall in another group and (iii) the room temperature FCG data is far away from the high temperature data. This indicates that the effect of temperature on the FCG behaviour is different at different temperatures.

Figure 4.10 shows the variation of ΔK_{th} and $\Delta K_{eff,th}$ with temperature. Both the threshold parameters (Fig. 4.10) decrease rapidly from 300 to 623 K, the extent of decrease of $\Delta K_{eff,th}$ being less. With further increase in the test temperature up to 773 K, both ΔK_{th} and $\Delta K_{eff,th}$ remain more or less constant, followed by a small increase at 823K, which again is smaller for $\Delta K_{eff,th}$.

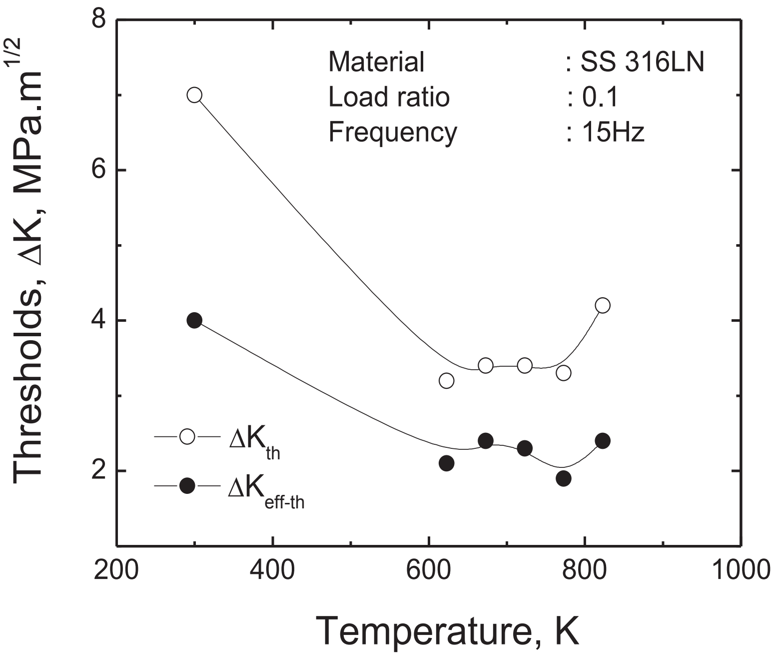

Figure 4.10 FCG thresholds at different temperatures

The decrease in ΔK_{th} with temperature is attributable to the decrease in the strength of the material as presented in Table 4.2where the yield strength decreases from 290 MPa to 160 MPa from 300 to 623 K. With further increase in the temperature, the yield strength remains nearly the same. The plateau in the ΔK_{th} in the temperature range 623 -773 K is consistent with change in yield strength with temperature. Similar trends in the thresholds have been reported previously for SS316 (N) welds and P91 steel [105, 152]. However, the relatively higher ΔK_{th} at 823 K is primarily assigned to the oxide-induced crack closure, and is *partially* accounted for by closure correction. It is observed from the difference between ΔK_{th} and $\Delta K_{eff,th}$ that the extent of crack closure varies with temperature. For example, crack closure at 300 K is high compared to the other temperatures. Crack closure contribution is low at intermediate temperatures and there is again an increase in closure at 823 K. The variation in the extent of crack closure with temperature may be associated with the changes in the closure mechanism. There is a change in slip character from planar to wavy with increasing temperature leading to a reduction in roughness induced closure. Also, any transformation induced crack closure is absent at high temperature. Closure induced by oxidation becomes prominent at high temperatures. It is noted here again that even after the crack closure correction, the trend in variation of threshold with temperature remains the same, though the extent of variation is considerably reduced, especially at 823 K. The possible effects of DSA will be discussed later in section #4.5.

In section # 4.3.1 (Paris regime), normalization of ΔK by σ_{ys} was found to be more appropriate than by E in the description of temperature dependence of FCG data in the Paris regime. Hence, the same exercise is carried out with the threshold regime data to examine how far the temperature dependence of σ_{ys} influences the FCG behaviour in this regime. Figure 4.11 (a) and (b) present the results of da/dN as a function of $\Delta K/\sigma_{ys}$ and $\Delta K_{eff}/\sigma_{ys}$ for different temperatures. From Fig 4.11(a) it is clear that taking in to account the temperature dependence of yield strength brings down that of the FCG threshold. However, there is a considerable increase in the thresholds with temperature, beyond 623 K. The closure corrected data, on the other hand, shows much lesser temperature dependence. Thus, normalising the ΔK with yield strength amplifies the closure contribution in the threshold indicating that the closure here is oxide-induced. In the threshold region, the temperature dependence of closure-free FCG is almost completely accounted for by that of σ_{ys}. Presumably, there is no additional influence of DSA in this regime other than through σ_{ys}. However, it may be argued that the small increase at 673 K followed by a decrease up to 773 and again an increase at 823 K are also associated with setting in of DSA due to interstitials, its disappearance and further setting in of DSA due to substitutional solutes at 773-823 K. This would require additional studies.

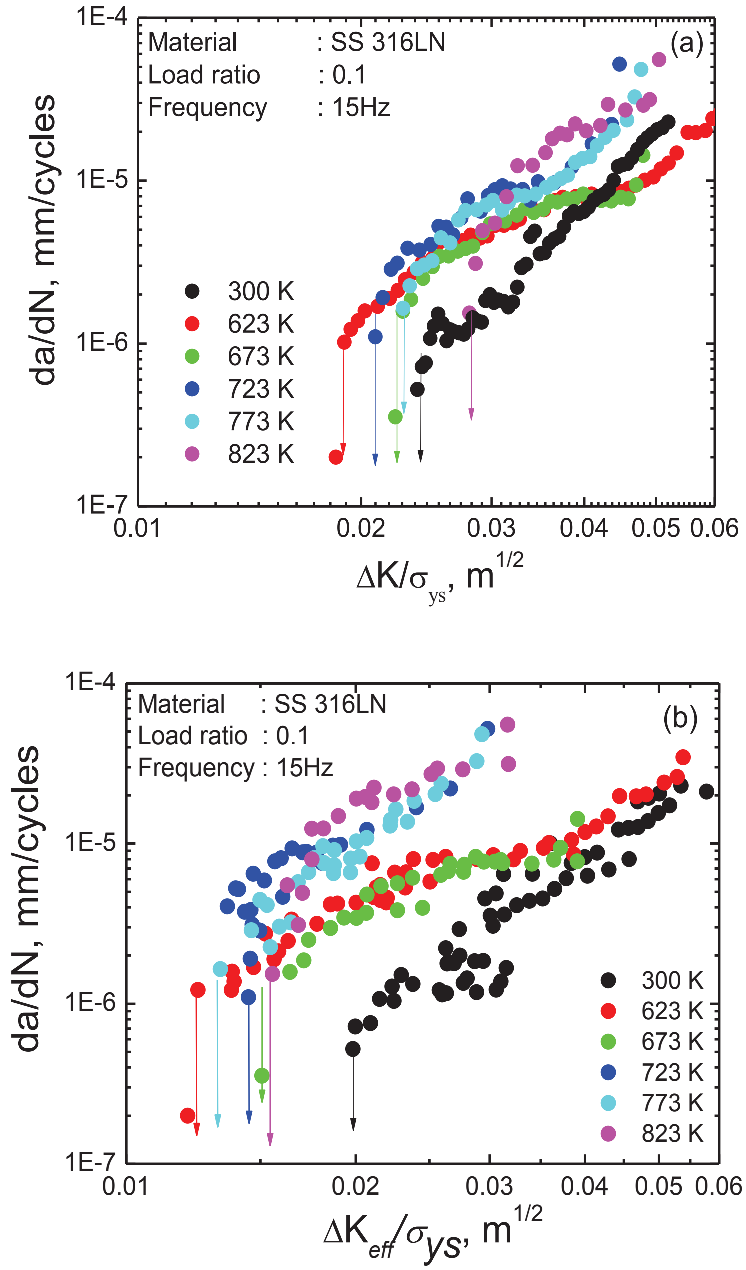

Figure 4.11 FCG results of SS 316LN-8N, (a) ΔK, (b) ΔK_{eff} normalized with yield strength in the temperature range 300-823 K

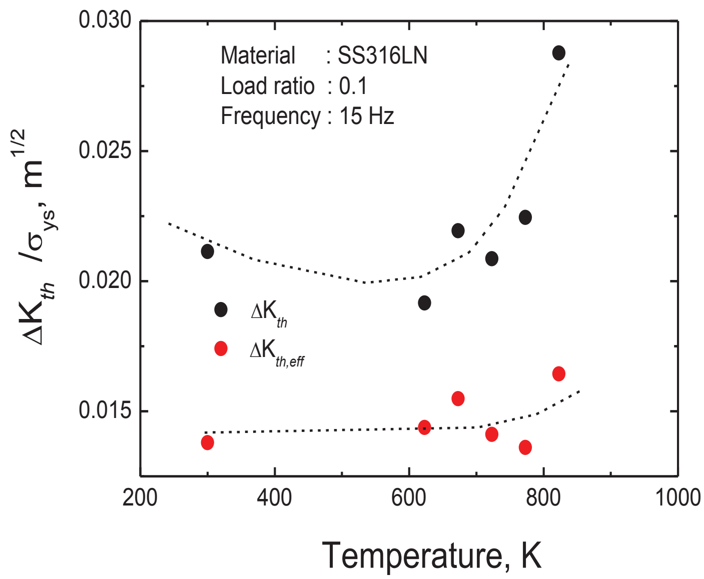

Figure 4.12 FCG thresholds normalized with yield strength at different temperatures

4.4 Change in crack closure mechanisms with temperature

Slip is one of the important deformation mechanisms, which plays a significant role in the FCG behaviour. In the present case, the material of study is SS 316LN steel which has a face centered cubic (FCC) structure. Generally, all the 12 slip systems in FCC materials are activated during deformation even at room temperature. However, the presence of N in SS316LN lowers its stacking fault energy, making difficult the constriction of partial dislocations to enable cross slip, resulting in predominantly planar slip. Crack growth occurs along the planar slip bands that form along the easy slip system, viz., the [110] and (111) system. In a polycrystalline system, the difference in grain orientation between neighboring grains necessitates crack path deviations, depending on the angles of tilts and twists between the grains. These deviations lead to the increase in the roughness of the crack surface. However, at high temperatures, cross slip becomes easier and the slip character changes from planar to homogenous due to random slip systems becoming active [106]. Slip can take place along any of the favourably oriented systems and hence crack can grow along any one of the activated slip planes rather than the (111) planes unlike in the case of crack growth at room temperature. Thus, the crack path is straighter resulting in considerably reduced roughness of the crack surfaces. The differences in the tortuousness of crack paths at different temperatures presented in Fig.4.13 (a) through (c) are in agreement with the above observation.

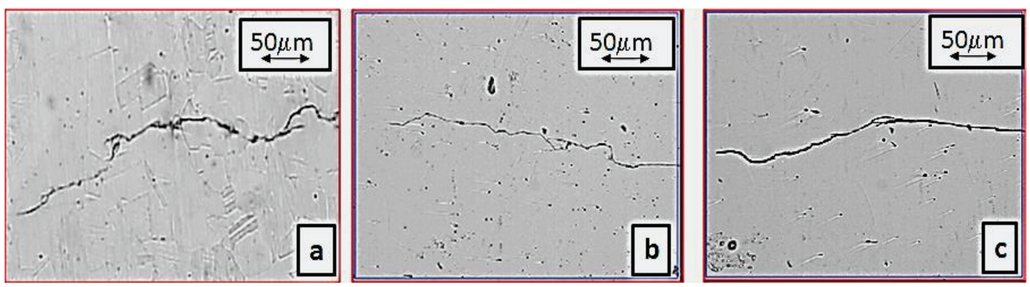

Figure 4.13 Crack path deviations with temperature (a) 300 K, (b) 623 K and (c) 823 K

Considering the slip character, it is apparent that the roughness induced crack closure (RIC) contribution is predominant at room temperature. The RIC comes down significantly with increase in temperature due to increased homogeneity of slip. Next, consider the plasticity induced closure. The plastic zone size is an inverse function of yield strength ($r_p = \frac{1}{2\pi}\left(\frac{\Delta K}{\sigma_{ys}}\right)^2$). Since the yield strength decreases with temperature, there is an increase in the crack tip plasticity leading to increase in the plasticity induced crack closure, if any. At high temperature, e.g., 823 K, oxidation of the crack surface scan lead to oxide induced crack closure. However, at intermediate temperatures, both contributions are minimum and hence the ΔK_{th} is low in the intermediate temperature. From the FCG results after crack closure correction presented in Figs.4.4 and 4.9, it is clear that the extent of crack closure is different at different temperatures. A comparison of the data presented in Figs. 4.3 and 4.4 indicates that the extent of crack closure is low for the test temperatures 623 and 773 K, while it is high at 673, 723 and 823 K in the ΔK range 10-25 MPa.m$^{1/2}$. This observation indicates the possibility of contributions from more than one crack closure phenomenon in this temperature range. Also, even after closure correction, the trend in FCG thresholds (Fig. 4.9) remain same confirming that in addition to variation in closure contribution with temperature, the FCG behaviour is influenced by other mechanisms. The overlapping of the FCG curves at intermediate test temperatures is examined by considering the dynamic strain ageing (DSA) effects rather than the crack closure effects which are not consistent with the crack growth mechanisms.

4.5 Effect of Dynamic strain ageing on FCG

The observed improvement in FCG resistance at 623-823 K is examined with reference to the changes in mechanical behaviour due to DSA effects. The manifestations of DSA in tensile test results have been discussed extensively in literature [207, 208]. It is well established that DSA manifests as (i) increase in strength (ii) decrease in ductility (iii) increase in work hardening rate and (iv) negative strain rate sensitivity of flow stress [207]. The consequent changes in tensile properties of material at different temperatures can lead to the observed anomalous variations observed in the FCG parameters in the intermediate temperatures (623-773 K),, viz., the non-monotonic variations in log$C$ and m in Fig. 4.5 and observed temperature-independence of FCG curves etc. Presence of DSA in

SS316L(N) in this temperature range is corroborated with the tensile properties at different temperatures presented in Table 4.2. The yield strength rapidly decreases from room temperature to 623 K. However, the rate of decrease in the yield strength at 673 K is low, and a small peak in YS is observed at 723 K. In addition, yield strength is more or less same at 773 and 823 K

4.5.1 Effect of dynamic strain ageing on fatigue damage

All the manifestations of DSA mentioned above have been observed in SS316LN steel [107,123,204,205]. Increase in strength is expected to increase the FCG resistance; however, in the case of SS316LN, only a plateau in strength has been observed. Reduced ductility is expected to lead to decrease in FCG resistance, while the observation in the present study is a plateau in the threshold regime from 623 to 773 K followed by an increase at 823 K. An extensive study by Choudhary [208] on the same SS316L(N) indicated DSA in this material over a wider temperature range, viz., 523-873 K. While the σ_{ys} showed a plateau, the flow stress for higher levels of strain showed a discernible peak, the strength of which increased with increasing strain level from 0.002 to 0.2. The FCG specimens have extremely sharp cracks and the strain levels at the crack tip can exceed 0.2. Thus, the flow stress of the material at the crack tip can be high, especially at ΔK levels corresponding to the Paris regime. In the present study, the elevated temperature tests cover only a part of the temperature range. More studies at temperatures in the range 300-623 K and above 823 K will further elucidate the effects of DSA on the FCG behaviour in the entire DSA range.

Choudhary [208] has estimated the DSA induced changes in the work hardening rate θ of the same SS316LN steel at strain rates in the range $3\text{x}10^{-3}$ to $3\text{x}10^{-5}$ s^{-1}. He defined two θ values, θ_2 and θ_5, the average work hardening rates, as the rate of change in flow stress with strain from 0.2 to 2.0% strain and from 0.5 to 5.0% strain respectively. He evaluated θ_2 and θ_5 at different temperatures and strain rates from true stress–true plastic strain as $\theta_2 = (\sigma_{0.02} - \sigma_{0.002})/(0.02-0.002)$ and $\theta_5 = (\sigma_{0.05} - \sigma_{0.005})/(0.05-0.005)$, where $\sigma_{0.002,}$ $\sigma_{0.005,}$ $\sigma_{0.02,}$ $\sigma_{0.02}$ are the true stress values for true plastic strains of 0.002, 0.005, 0.02, and 0.05 respectively.There is a significant increase in θ in the DSA regime with a peak towards the end of the DSA regime. For SS316L(N) in solution annealed condition, he reported an increase in θ_2/E and θ_5/E with temperature in the range 573 - 873 K, the latter being more significant.

The observation here is that there is an increase in crack growth resistance in the DSA temperature range, which is not fully rationalised by considering the variation in yield strength. A phenomenological description of how DSA improves the FCG resistance is given below, based on the effect of variation in θ. FCG test is done in the load control mode where load keeps varying (either increase or decrease depending on the chosen test mode). The effect of θ on the stress-strain hysteresis loop is shown schematically in Fig. 4.14. This is specific to the load control mode in which the FCG test was carried out. It is obvious from Fig. 4.14 that the low θ condition leads to higher plastic strain compared to the high θ condition. The extent of fatigue damage depends on the plastic strain amplitude. Though the FCG specimen is in a globally elastic condition, local crack tip plasticity plays an important role in causing fatigue damage and resulting crack growth. Also, the hysteresis loop energy, which indicates the energy input to the material that causes damage, is lower in the high θ condition, i.e., in the DSA regime. Lower plasticity in the high θ conditions results in lower level of accumulated fatigue damage, and therefore lower FCG rate. Thus, DSA occurring at the crack tip cause an increase in crack growth resistance. In other words, to maintain the same crack growth rate, or to inflict the same level of crack tip damage, it needs a higher driving force (ΔK) in the DSA temperature range due to the increase in θ. Hence, threshold shifted to higher values (than would be expected in the absence of DSA) with temperature due to DSA.

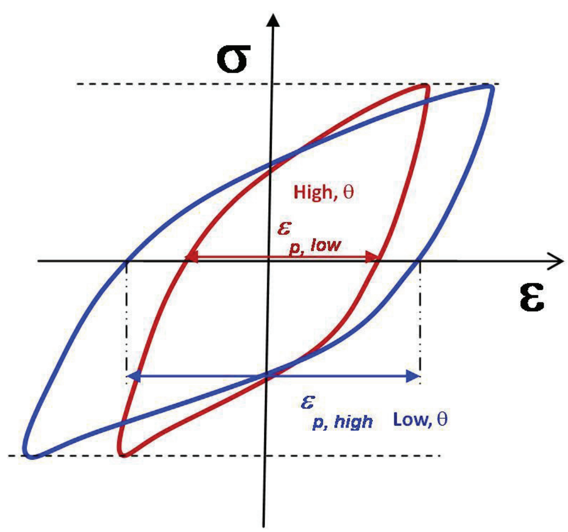

Figure 4.14 Schematic diagram of plastic strain(ε_p) response during stress control fatigue test for the low ($\varepsilon_{p,low}$) and high ($\varepsilon_{p,high}$) work hardening material.

Now, consider the possible effects of DSA on FCG parameters in the Paris regime. Generally, while load-shedding mode of test is used in determining the FCG threshold, load increasing mode is employed for the Paris regime. According to available reports in the literature, the onset and disappearance of serrations due to DSA in the load-elongation data from tensile tests happens at certain critical levels of strain [207-209]. The temperature dependence of this critical strain has often been used to evaluate the activation energy for DSA in order to identify the responsible species. Also, DSA is a phenomenon that operates in a certain range of strains, strain rates and temperatures. In a FCG test, the strains and strain rates change with changing ΔK, and there is a possibility that DSA effects are not present during the entire test, but only in part of the test. In a ΔK increasing test, the onset of DSA will lead to a decrease in m and increase in C values as observed in the present study. In a ΔK decreasing test, on the other hand, the reverse is true. This can be experimentally verified by conducting tests in both the modes within and outside the DSA temperature regime. A quantitative analysis of the changes in m and C values would require more in-depth studies at different temperatures and frequencies, which however, will induce additional mechanisms that influence the FCG behaviour, making extraction of any meaningful information extremely complex.

4.5.2 Mechanism of dynamic strain ageing

The different manifestations of DSA are caused by the dynamic interaction of moving dislocations with interstitial or substitutional) solute atoms. In order to ascertain the mechanism for DSA, the kinetics of the crack growth process (or the damage mechanisms at the crack tip) as a function of temperature can be examined using the Arrhenius type of relation. Since DSA is a time-dependent process, one can consider the temperature dependence of crack tip strain rate ($\dot{\varepsilon}_{tip}$) as an appropriate prameter to estimate the activation energy Q for the process. In environmentally assisted cracking studies, there have been studies to correlate $\dot{\varepsilon}_{tip}$ to load-line displacement rate or ΔK [209]. The ΔK dependence of $\dot{\varepsilon}_{tip}$ has been given as $\dot{\varepsilon}_{tip} = f(\Delta K^{n})\ \mathrm{s}^{-1}$, where n varies from 2 to 4 as the Paris exponent (m). Peter et al. [210] describe $\dot{\varepsilon}_{tip}$ as a function of ΔK and frequency of cyclic loading as $\dot{\varepsilon}_{tip} = 68.6 \nu A_R \Delta K^4 \mathrm{s}^{-1}$, where ν is the cyclic loading frequency and A_R depends on R (2.44×10^{-11} for $R \leq 0.42$ for austenitic stainless steels). Here, the n values have been taken from the Paris regimes data presented in Table 4.1; these values varying from 2.55 to 3.75 for different temperatures are chosen for the exponent instead of 4, in the analysis. The ΔK is considered to be the driving force for the crack tip damage processes. Thus, the crack tip strain rate ($\dot{\varepsilon}_{tip}$) at different temperatures corresponding to ΔK at transition point from Fig 4.8 values (Table 4.3) have been

Table 4.3 Transition point in the FCG curve at different temperatures

Temperature, K	623	673	723	773	823
Inflection point, $\mathrm{MPa.m}^{0.5}$	7.60	7.16	5.59	5.23	5.50

calculated as $\dot{\varepsilon}_{tip} = 68.6 \nu\ A_R\ \Delta K_{eff}^{\ n}\ \mathrm{s}^{-1}$. The temperature dependence of $\dot{\varepsilon}_{tip}$ can be expressed in the form of an Arrhenius type equation as $\dot{\varepsilon}_{tip} = Ae^{-Q/R_g T}$, where A is a constant, R_g is the gas constant and temperature is in K. Arrhenius plots ($\ln \dot{\varepsilon}_{tip}$ vs. $1/T$) for 623 – 823 K in Fig. 4.15 shows a two slope behaviour, indicating the possibility of different rate-controlling mechanisms. The lower slope corresponding to the temperature range 623-723 K gives an activation energy of 90±2 kJ/mole, which is in the range of that for carbon diffusion in austenitic steels (47-90 kJ/mol) [211]. The higher slope corresponding to the temperature range 723-823 K gives an activation energy value of 160±5-kJ/mole, is same as that for nitrogen diffusion in stainless steels [212]. Thus, in the entire range of temperatures examined here, DSA controlled by interstitial diffusion is responsible for the observed *T*-dependent changes in FCG behaviour. DSA associated with substitutional diffusion may be active at higher temperatures.

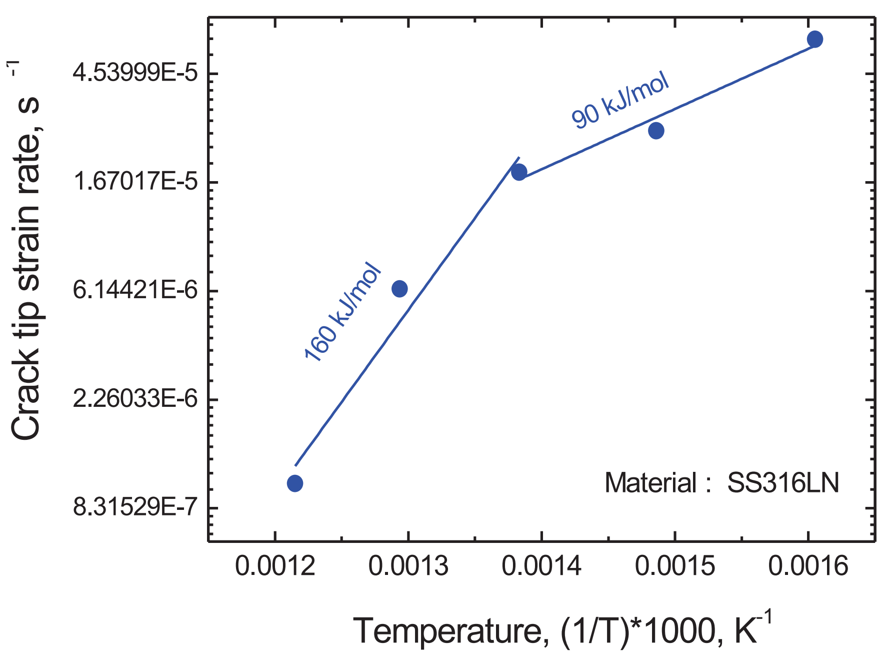

Figure 4.15 Arhenius plot of crack tip strain rate for the temperature range 623 - 823 K corresponding to ΔK at which DSA vanishes

4.6 Effect of test frequency on the fatigue crack growth

The loading frequency/strain rate exerts an influence on the elevated temperature FCG behaviour. This can come through the time-dependent phenomena such as creep, oxidation etc in addition to the significant role played by strain rate in the DSA regime. To examine these, tests were carried out at different frequencies. Figure 4.16 presents the FCG results at 75 Hz for different temperatures. There is a monotonic decrease in the threshold with temperature till 773 K followed by a small increase at 823 K (possibly due to the oxide-induced closure, which was not measured). The crack growth rate increases with temperature at higher ΔK regime, i.e., above ~ 6 MPa.m$^{1/2}$, whichis an expected trend. The ΔK_{th} values obtained at 75 Hz are presented in Fig 4.17 as a function temperature along with the data for 15 Hz from Fig. 4.9 for the purpose comparison. The salient observations are as follows:

(i) ΔK_{th} values are independent of frequency at room temperature. This is understandable since beneficial effect of DSA or detrimental effect of crack tip-environment interaction are not significant.

(ii) However, at higher temperatures, the ΔK_{th} values are lower for 15 Hz than those obtained at 75 Hz. One may argue that it is due to the longer time available at this frequency for other time and temperature dependent mechanisms such as interaction of the freshly exposed fracture surface with the air environment, or creep effects to cause an increase in the crack growth kinetics. However, in that case, these effects should have led to a decrease in ΔK_{th} with further increase in temperature, which is not the observation. The lowering of local stress intensity factors due to creep-induced crack tip blunting [210] is assumed insignificant at these frequency ranges.

(iii) The trend is similar at both the frequencies with an initial decrease in the threshold with increasing temperature to attain a minimum followed by a marginal increase. The minimum in ΔK_{th} at 15 Hz occurs at a lower temperature (623 K) than that at 75 Hz (between 723 and 773 K) consistent with the DSA theory.

(iv) At 15 Hz, the extent of increase in ΔK_{th} is small in the range 623-773 K and significant from 773 to 823 K. However, at 75 Hz not only there is a decrease in ΔK_{th} in the range 623-773K, the increase in ΔK_{th} from 773-823 K is small compared to that at 15 Hz. Therefore, it is likely that at high frequency, either the DSA effects are less or the DSA range shifts to higher temperature. Additional tests above 823 K are needed to confirm this.

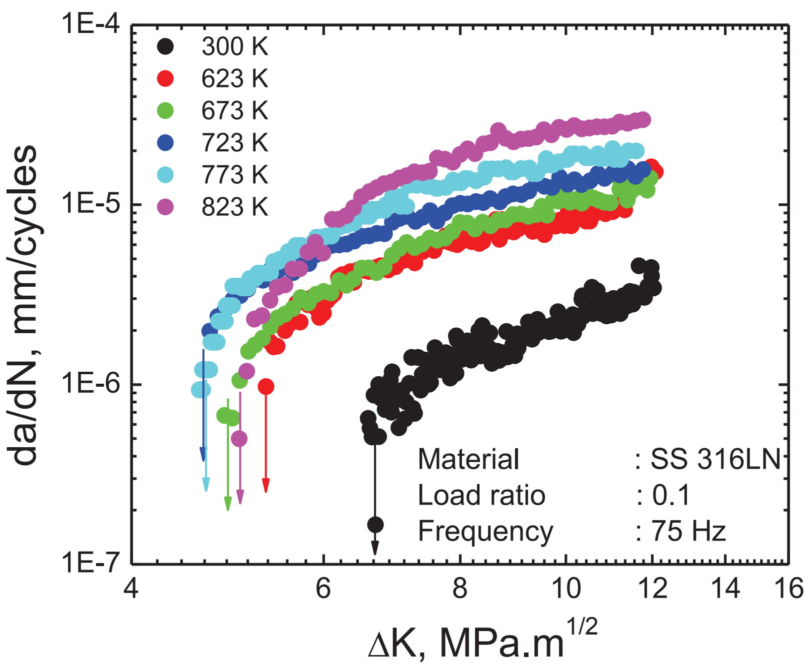

Figure 4.16 FCG behaviour of SS316LN-8N at 75Hz and different temperatures

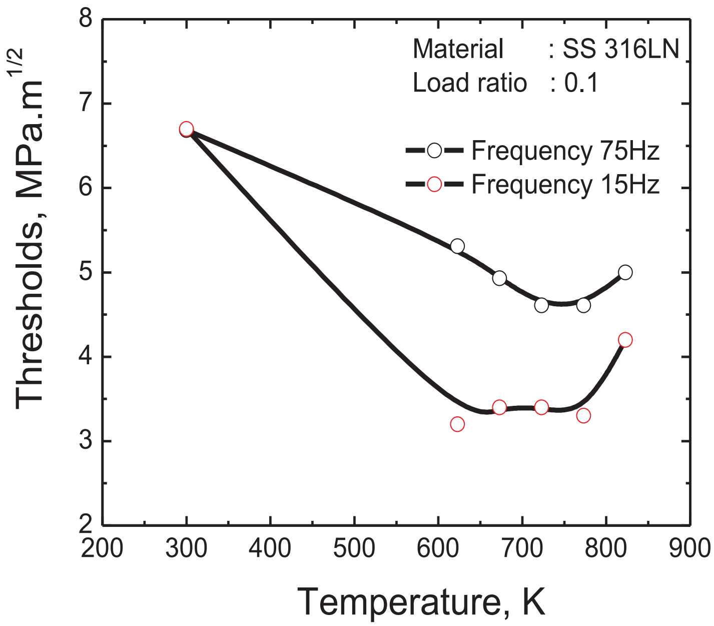

Figure 4.17 Effect of frequency on the threshold behaviour of SS316LN-8N different temperatures frequency 75 Hz in the figure

FCG tests were carried out at a much lower frequency, viz., 0.75 Hz, in the threshold regime at 673 K, which is in the midrange of minimum in threshold observed at a frequency of 15 Hz. Results are presented in Fig 4.18 along with those for 15 and 75 Hz. In the threshold regime, the crack growth resistance is higher for 0.75 Hz than 15 and 75 Hz, which is consistent with the possibility of crack tip blunting leading to reduction in crack tip stress intensities. However, at higher ΔK levels, the crack growth rate obtained at 0.75 Hz falls between those for 15 and 75 Hz. In this region, the crack is already much blunter at all the frequencies than in the threshold regime, and the time available for creep even at 0.75 Hz is lesser. Another factor is the strain hardening of the crack tip material. The effect of increased work hardening due to DSA has already been discussed earlier in Section #4.5. The same discussion holds good here since even in absence of DSA, faster loading rates generally induce higher hardening at the crack tip, since the recovery is less.

Marvasti, et al, [213] suggest a third threshold in addition to ΔK and K_{max} thresholds, viz., a frequency threshold for crack growth in pipeline steels. They propose two reasons for dormancy of cracks at low frequencies leading to this. These are related to reduction in local stress intensities at the crack tip due to crack blunting. The longer time available at low frequency and high temperature cause creep and/or oxidation leading to crack tip blunting. In the present material, these factors may contribute to the improved crack growth resistance at low frequencies. Conventionally, this behaviour is ascribed to crack closure induced by plasticity/creep or oxides; however, this is in controversy since it happens even when closure cannot be observed in the load-displacement data. Hence, there is a need for the unified approach to describe the FCG behaviour.

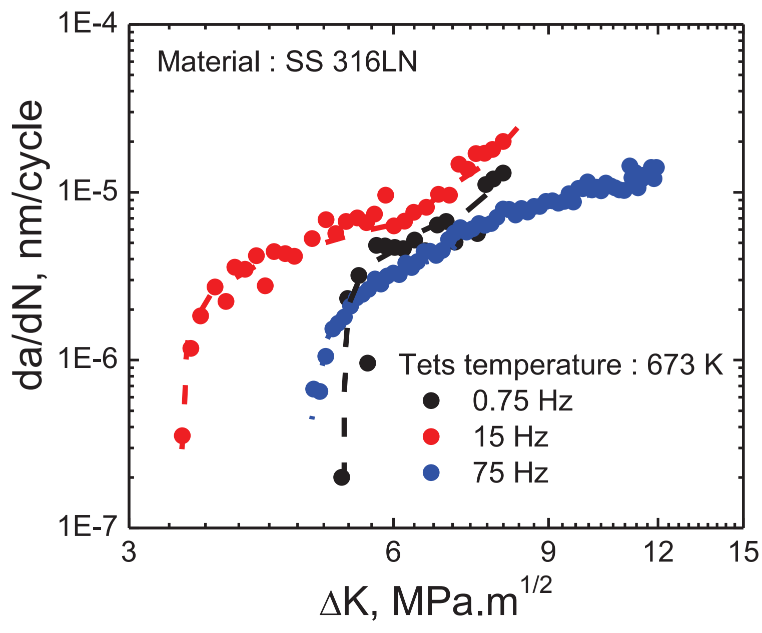

Figure 4.18 Comparison of FCG behaviour of SS316LN-8N at 673 K and different frequencies.

4.7 Conclusions

Fatigue crack growth behavior SS316LN steel has been evaluated in Paris and threshold regimes for the temperature range 300 - 823 K. The crack growth behaviour after crack closure correction compared with the constant K_{max} test data at room temperature indicates the discrepancy in the crack closure theory. The improved FCG resistance in the intermediate temperatures is attributed to the dynamic strain ageing effects rather than crack closure. Attempts to correlate the FCG data with normalized (using modulus and yield stress) driving forces did not completely account for the temperature dependence. Moreover, an increase in crack growth thresholds is observed at high temperature when compared to those obtained at intermediate temperature range 623 - 823 K. The plateau or increase in the effective threshold with temperature and overlapping of FCG curves in the range 623 - 823 K is due to DSA, which exerts beneficial influence on the intrinsic FCG resistance. The activation energy values estimated are 90 ± 2 kJ/mol in the temperature range 623-723 K similar to that for carbon diffusion, and 160 ± 5 kJ/mol in the temperature range 723-823 K similar to that for nitrogen diffusion indicating that the interaction of interstitial solute elements with dislocations is responsible for the DSA enhancing the FCG resistance of this steel. The reason for much larger increase of threshold at 823 K could not be unequivocally established though possibilities are DSA associated with substitutional solutes, and crack tip blunting due to creep or oxidation effects leading to reduced local stress intensities. Further studies are required towards this.

The dormancy of crack leading to higher threshold at low frequency and high temperature is possibly associated with blunting of crack tip due to creep and/or oxidation. It is obvious that this is not because of the plasticity or oxide induced crack closure. Difference between closure-corrected data from constant R test and closure-free data from constant K_{max} test suggests the inadequacy of crack closure in explaining several aspects of the FCG behaviour. Hence, further studies have been focused on FCG analysis using the unified approach or the two parameter approach which appears to be more fundamental in nature.

CHAPTER 5

ROLE OF NITROGEN ON THE FATIGUE CRACK GROWTH BEHAVIOR OF AUSTENITIC STAINLESS STEELS AND ANALYSIS USING UNIFIED APPROACH

CHAPTER 5 : ROLE OF NITROGEN ON THE FATIGUE CRACK GROWTH BEHAVIOR OF AUSTENITIC STAINLESS STEELS AND ANALYSIS USING UNIFIED APPROACH

5.0 Introduction

The various effects of nitrogen in austenitic stainless steels and their consequences in the mechanical behaviour have been discussed in Chapter 2: Literature Survey. These have important implications with respect to the fatigue crack growth behavior. This chapter deals with the effect of nitrogen on the FCG behavior of SS316L(N). The FCG results at room temperature for the three variants of this steel with 0.08, 0.14 and 0.22 mass% N (referred to as 8N, 14N and 22N respectively) have been presented and discussed. In addition to the conventional analysis of FCG data incorporating crack closure as prescribed in the ASTM standards for FCG (E647) and the French code for fast reactor nuclear islands, the RCC-MR, this chapter focuses on the fundamental inadequacies of the conventional FCG analysis as described in the previous chapter, particularly with respect to the crack closure phenomenon in the context of load ratio effects. In order to address these, the unified approach developed earlier has been used as a tool for an extensive analysis to evaluate the roles of (a) nitrogen and (b) load ratio on the FCG behaviour of these steels.

5.1 Background

At Indira Gandhi Centre for Atomic Research (IGCAR), Kalpakkam, a program has been initiated to develop SS316LN with optimum N content to improve the mechanical properties, and thus extend the life of the structural components. While the optimization is based on the tensile, creep and fatigue behavior, adequate resistance to crack growth in terms of the fracture mechanics properties needs to be ensured. As a part of this program, FCG resistance of SS316L(N) with three different N levels (8N, 14N and 22N) has been evaluated at ambient temperature at load ratio R = 0.1 [131]. The results of this preliminary study are presented in Fig. 5.1.

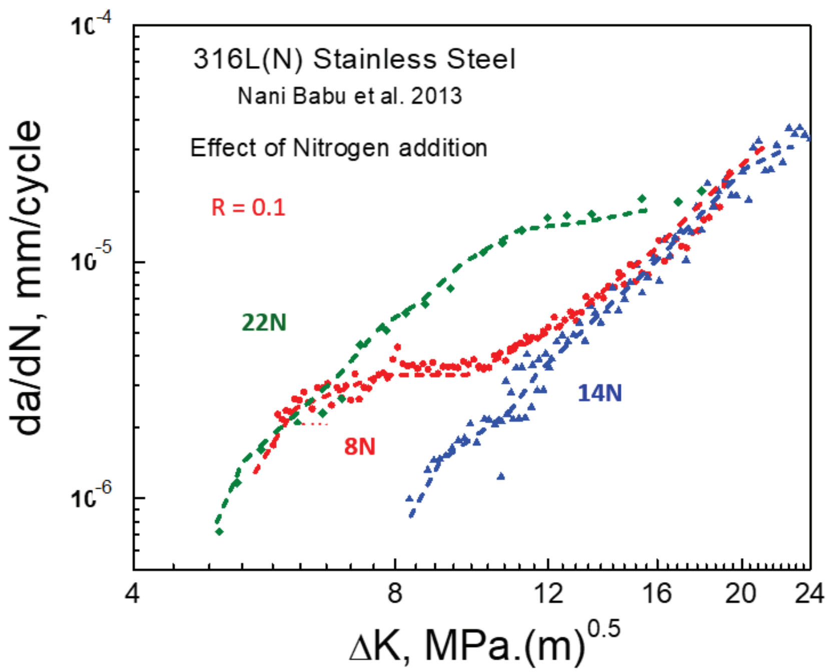

Figure 5.1 Effect of nitrogen on fatigue crack growth resistance of SS 316LN at room temperature

It is observed that the 14N steel has the best FCG resistance among the three variants. The 8N steel has FCG resistance similar to 14N steel in the Paris regime, while in the threshold regime, it is similar to 22N steel which has the lowest FCG resistance. Repeat tests confirmed the same trend. For 8N alloy, the crack growth rates follow that of 22N at low stress intensity factor range (ΔK) less than 6 MPa.m$^{0.5}$; but with increasing ΔK, the curve shifts towards that of 14N alloy. It is well known that in the low ΔK regime, the crack growth rate is more sensitive to microstructure, such as grain size, precipitates etc. FCG resistance found to be better for 14N variant when compared to the other variants. Nitrogen, while stabilizing the austenite phase, also a) improves the solid solution strengthening, b) causes grain-refinement thereby contributing to additional strengthening, and c) increases toughness via strain-hardening. All these effects, especially (b) and (c), are apparently beneficial for FCG resistance. Grain refinement leads to reduced FCG rate as the boundaries act as barriers to crack since on encountering a grain boundary, the crack propagation is temporarily halted till sufficient plasticity is generated by reinitiating slip in the next grain depending on the orientation. Also, this leads to frequent changes in the crack path, which in turn results in local changes in the mode of loading, thus reducing the driving force experienced by the crack tip [152]. However, there are no significant variations in the grain size with nitrogen content in the present study (details are presented in the microstructural analysis). The tests in this study were conducted at room temperature on solution annealed material, and hence the precipitate microstructure also is assumed to be similar. Therefore, the microstructural influence on FCG rates can be considered to be insignificant. The effect of increased strain hardening rate on improving FCG resistance has been discussed in detail in [105] with respect to the beneficial effects of dynamic strain ageing (DSA) under load controlled testing.

However, the FCG results presented above indicate a reversal in the beneficial effects of N beyond 0.14%. As already discussed in Chapter 2; Literature Survey, the decrease in stacking fault energy with increasing N content also shows a reversal in trend at 0.14%, [214] though there are contradictory reports in the literature on these effects. The enhanced FCG resistance for 14N alloy and the observation that 8N has similar resistance only at high values of ΔK, points to the possibility that some other mechanism that is dependent on both N content and stress level plays a role here and evokes the curiosity as to what is this mechanism. Austenitic stainless steels are known to undergo stress or strain induced phase transformation [136-139, 142-144]. This transformation, normally associated with the shear deformation process, can impart a good combination of strength and toughness to many structural materials [142-144], including ceramics [78]. For the austenitic stainless steels, it involves the austenite phase undergoing deformation induced martensitic transformation (DIMT) ahead of the crack tip due to the crack tip stress or strain fields. There are several parameters like strain rate, temperature, state of stress and/or strain, etc., that can influence the transformation due to plasticity ahead of the crack tip [137, 136].

Nitrogen additions to 300 series austenitic stainless steels stabilize the austenite, and hence inhibit the stress/strain induced transformation to martensite, which in turn can influence the mechanical behavior including the crack growth resistance. This was demonstrated by the results of classical experiments of Mei and Morris [142, 143] shown in Fig. 5.2. They have tested 304L stainless steel with and without nitrogen (304LN and 304L) at room temperature, and at 77 K. The absence of N in 304L favors localized transformation induced toughening at the crack tip, enhancing the FCG resistance. Figure 5.2 shows that at room temperature, FCG rates in both 304L and 304LN are the same, indicating that any beneficial effects of nitrogen on the mechanical properties including toughness in 304LN is offset by the lack of DIMT in it. In other words, the contributions to crack growth resistance in

304L due to DIMT and in 304LN due to nitrogen effects are of the same order. However, at 77 K, where the stress-induced martensitic transformation is more pronounced, 304L has a significantly higher FCG resistance than 304LN since presence of nitrogen inhibits the transformation in the latter. Also, in 304LN, the crack growth rates at 77 K are similar to those at room temperature, except at very high ΔK where some enhancement in crack growth resistance can be found. These results indicate that in the nitrogen bearing stainless steel, the extent of the transformation induced toughening is low. At very high stresses or strains, some transformation may still occur enhancing the crack growth resistance.

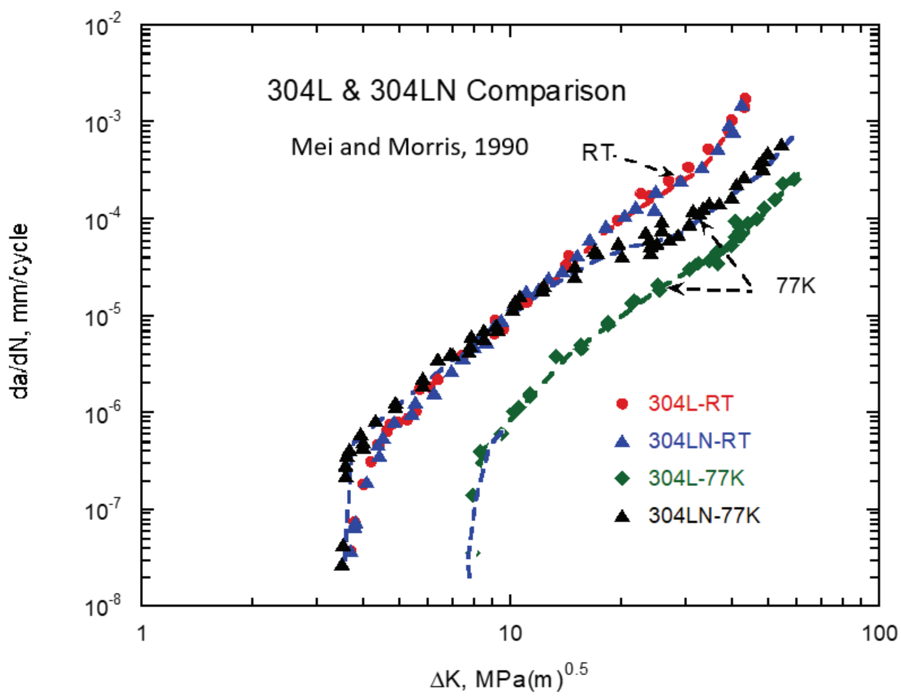

Figure 5.2 Effect of nitrogen on fatigue crack growth resistance for 304L and 304LN at RT and 77K.

A relook at Fig. 5.1 in line with the results of Mei & Morris [142, 143] to examine the role of DIMT shows that a) the transformation toughening occurs even at room temperature (298 K), and b) the extent of toughening depends on the N content. Thus, the results indicate that the transformation toughening depends on the stress or strain level as well, besides the temperature as noticed in the case of 304L. Lower temperatures and higher stresses seem to favor transformation and the high N content inhibits it.

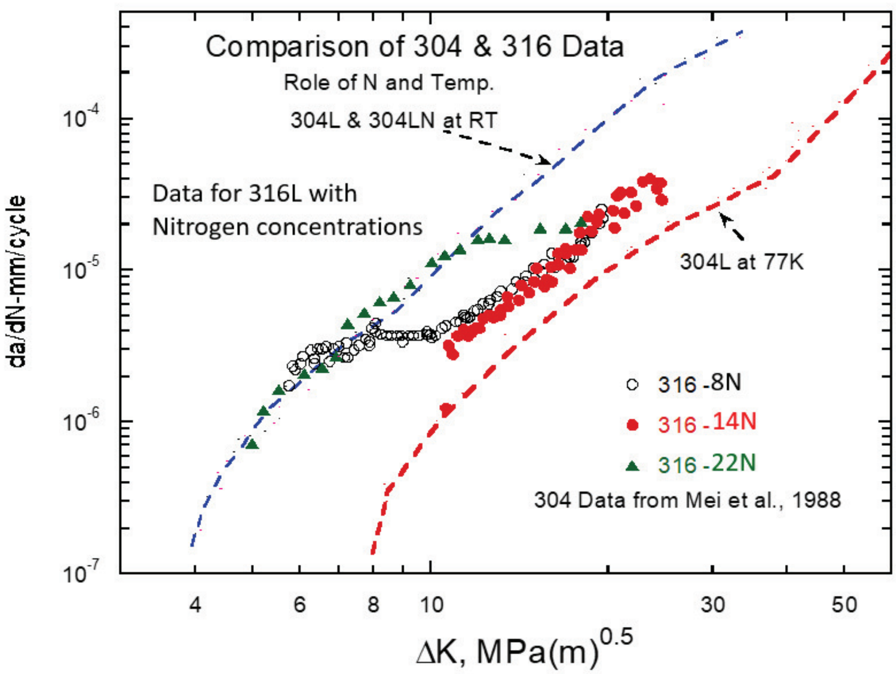

Figure 5.3 Comparison of FCG resistance for 304 and 316 austenitic stainless steels**.**

The results of SS316L(N) [131] and SS304 [143] from Fig. 5.1 and 5.2 are compared in Fig. 5.3. When there is no transformation toughening, the crack growth rates in SS 304L and SS 316L are essentially the same. However, the results of 14N at 298 K are closer to SS 304L at 77 K indicating some transformation toughening. One can expect larger contribution from toughening at lower temperatures. The crack growth rates of 8N alloy swing from no toughening at low stresses to the enhanced toughening at higher stresses. Thus, these results confirm that in SS 316L, enhanced FCG resistance due to the transformation toughening occurs even at room temperature depending on the N content.

XRD investigation of the FCG tested samples of SS316L(N) in the preliminary study confirmed the presence of martensite at the crack tip in 8N steel, especially at high ΔK levels emphasising the need for further studies to clarify the possible role of DIMT. The FCG data presented in Fig. 5.1 and 5.2 were generated at $R = 0.1$ as per the ASME and RCC-MR requirements for the structural integrity assessment of the components to confirm the adequacy of the materials' crack growth resistance. Since the transformation depends on the stress and/or strain, these effects are expected to vary with load ratio R, as a consequence of change in peak stress in addition to the amplitude. In the present study, a detailed evaluation of the FCG rates in SS 316L is undertaken as a function of N content and R. FCG tests were conducted at different R values so as to achieve significant variation in K_{max}, which is expected to lead to significant changes in the level of DIMT, if any. Preliminary results of this investigation, using one N concentration was presented before [131].

5.2 Effects of Load Ratio on the FCG behavior

From the above preliminary results, it is clear that N plays a role in the FCG behavior, but the effects are not monotonic in nature and these cannot be linked only to the various strengthening contributions of N to austenitic stainless steels as discussed in Chapter 2: Literature survey. The ΔK-dependence of the N effects, clearly point to contributions from a K_{max}-dependent phenomenon that is responsible for this, possibly the DIMT, which is known to be inhibited by the presence of N.

Further analysis of the FCG data at different R-values is required to confirm and quantify the contributions of DIMT. The justifications and details of the advanced data analysis towards this are presented in the following sections.

5.2.1 The Two-parametric Approach for FCG Analysis

The crack growth rate data are analyzed using the Unified Approach developed by Sadananda et al. [21, 193]. It is based on the fact that fatigue requires two load parameters involving amplitude and peak or mean stress for unambiguous description. The S-N fatigue has been analyzed using the stress range ($\Delta\sigma$) and the mean stress (σ_{mean}), ever since Goodman [215] more than 100 years ago. After Elber [56] introduced the concept of plasticity-induced crack closure, the FCG data have been analyzed using only one load parameter, namely the $\Delta\sigma$ or the stress intensity factor range, ΔK. The observed effects of R on FCG have been accounted for using an extrinsic factor, namely the plasticity-induced crack closure, which is measured using the load (P)- displacement (d) plots. It is believed that plasticity in the wake of a crack contributes to premature crack closure thereby reducing the ΔK experienced by the crack tip. It was shown [66], however, using the dislocation theory that a) the crack-wake plasticity does not contribute to reduction in the crack tip driving force, b) every dislocation emitted by the crack tip has its counterpart contributing to crack tip opening displacement (CTOD) (see also Weertman [51]), c) crack tip, therefore, remains open during unloading unless all the dislocations originated from the crack tip go back into the crack, thereby reducing the crack to an elastic crack. Dislocation emission from the crack tip can be considered to be the same as taking the material from the crack tip and redistributing it ahead of the crack tip. Thus, there is a material balance which, in dislocation theory, is simply stated as the law of conservation of Burger's vector, and d) analysis of the dislocation-crack interaction also shows that the plasticity ahead of the crack tip contributes to retarding force on crack tip, while the plasticity in the crack-wake contributes very little to crack growth [66]. In addition, Toribio and Kharin [216] using their detailed analysis have shown recently that, *'plasticity induced crack closure, which is habitually attributed to filling-in a crack with material stretched out of the crack plane behind the tip, is ruled out',* and the *'calculated compliance curves are bent in spite of the absence of plasticity induced crack closure, which raises the doubt about their trustworthiness as the means of the crack closure detection and assessment'*. Similar conclusion was also reached by Kujawski and Stoychev [217] while analyzing the crack initiation at sharp notches. Hence, it was concluded that, similar to the *S-N* case, the *R* effects on FCG arise from the two-parametric nature of fatigue. Of the five variables involved, namely ΔK, K_{max}, K_{min}, K_{mean}, and R, only two are independent. Sadananda et al [21, 193] have found that for crack growth, ΔK and K_{max} provide the most convenient parameters since thresholds can be defined in terms of both. Similarly, for the *S-N* fatigue, instead of $\Delta\sigma$ and σ_{mean}, $\Delta\sigma$ and σ_{max} are more convenient since endurance limits in terms of both these can easily be defined [218]. All the phenomena hitherto attributed to crack-closure have been reanalyzed by the Unified Approach using the two-parametric requirement for fatigue [189-193, 215]. The *R* effects in the present case, therefore, are analyzed using the two-parametric approach. In addition, it is noted that Mei and Morris [142, 143] have shown earlier that the observed *R* effects in 304L steel cannot be accounted for by the crack closure due to crack-wake plasticity but can only be accounted by the DIMT ahead of the crack tip.

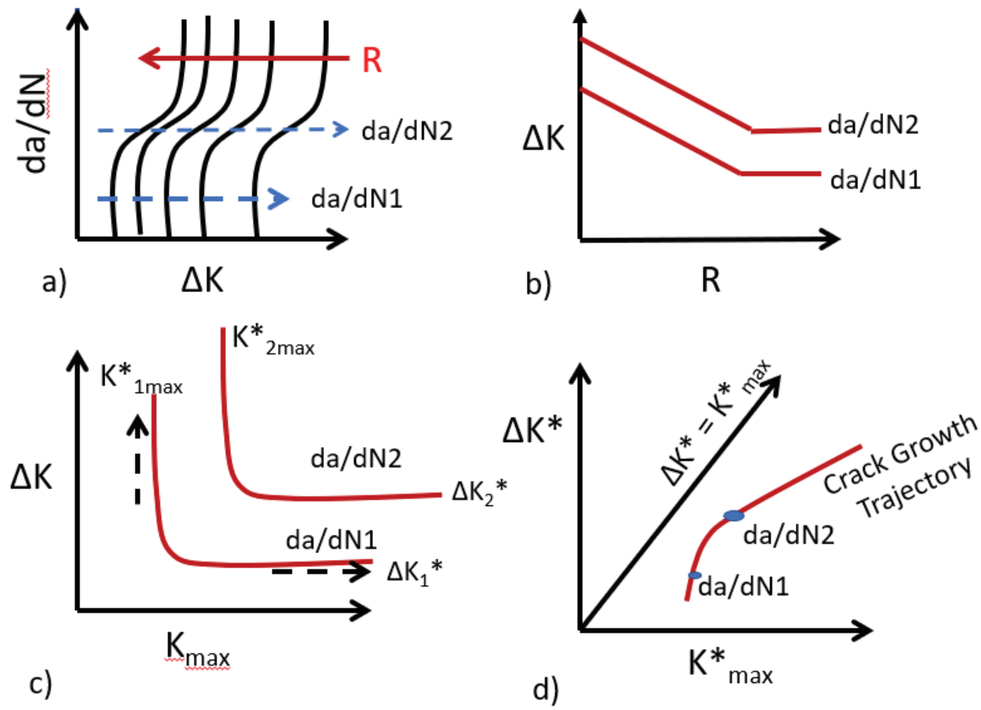

Figure 5.4 Schematic procedure to arrive at the two Crack-tip driving forces. a) FCG curves as a function of the R-ratio. b) ΔK-R bilinear curves for selected crack growth rates. c) The L-shaped ΔK-K_{max} curves generated using data extracted from figure b), for the selected crack growth rates. The L-shaped curves define the limiting values ΔK* and K_{max}* at each crack growth rate. d) Fatigue crack growth trajectory path depicting the material resistance to crack growth.

5.2.2 Estimation of Crack Tip Driving Forces

The data reduction scheme for arriving at the two crack tip driving forces, ΔK and K_{max}, is presented in Fig. 5.4. Generally, the FCG data are plotted in terms of crack growth rate (da/dN) vs. ΔK, as shown in Fig. 5.4a. From these data, one can plot ΔK vs. R for any given crack growth rate starting from threshold, as shown in Fig. 5.4b. Since ΔK vs. R plot generally is bilinear [187], this plot can be used to interpolate the data to extract additional values at intermediate R-values, particularly when the available FCG data as a function of R are limited. From these ΔK-R plots, one can generate ΔK vs. K_{max} plots for the selected values of crack growth rates, as in Fig. 5.4c. This ΔK-K_{max} plot generates, in essence, the relative variation of the two crack tip driving forces under fatigue, to enforce the imposed crack growth rate, da/dN. The material resistance is thus given by da/dN, and the ΔK and K_{max} values provide the measure of the applied forces to accomplish the task. The relative variation of the two parameters forms the fundamental material-resistance curve for any given crack growth rate (da/dN), as can be seen in Fig. 5.4c. They generally follow an L-shaped curve for any given da/dN. In a way, the ΔK and K_{max} values required to enforce a particular crack growth rate are relatable to cyclic and monotonic plastic zones formed as a part of the FCG process, and thus to the intrinsic response of the material to the imposed cyclic loads. At the threshold (i.e., da/d$N \leq 10^{-7}$mm/cycle), the curve defines the fundamental threshold regime below which a crack does not propagate under fatigue. Hence, fatigue threshold is not a single value, as is normally assumed, but a curve representing the relative values of the cyclic and static components that are involved, and thus defines the non-propagating regime for a given material and environment. Even though both parameters (ΔK and K_{max}) are involved in contributing to crack growth and both thresholds have to be met simultaneously for crack growth to occur, one or the other forms the controlling parameter in a given regime. For example, at low R values, K_{max} becomes the controlling parameter, since ΔK threshold is easily met. Likewise, at high R values, ΔK becomes the controlling parameter since K_{max} threshold is easily met. This aspect arises since the two are related via R as $K_{max}= \Delta K/(1-R)$. Fig. 5.4c also shows that for each crack growth rate, there are two asymptotic limits in terms of ΔK and K_{max}, and these are called the limiting values, ΔK^* and K^*_{max} for that particular crack growth rate. At the threshold crack growth rates, these form the limiting thresholds, ΔK^*_{th} and $K^*_{max,th}$. The curve obtained by plotting of these two limiting values, ΔK^* vs. K_{max}^* (parametrically as a function of FCG rate, da/dN) forms the "crack growth trajectory map", Fig. 5.4d. Each point on this trajectory corresponds to a crack growth rate. In essence, the crack growth trajectory map defines the change in crack tip driving forces required to ensure increasing FCG rates. There is an inherent history-dependence involved in the plot. The required crack tip driving force involving both ΔK and K_{max} can change as the material strain hardens during crack growth. Hence, the trajectory map also defines the crack growth resistance curve for a given material and test conditions. Thus, it reflects the intrinsic crack growth mechanisms involved for a given material and environment. When the ΔK^* -K_{max}^* trajectory lies on a 45° line passing through the origin, i.e., when we have the condition $\Delta K^* = K_{max}^*$ for all crack growth rates, it is referred to as ''pure fatigue line", a condition which is generally fulfilled when the damage occurs purely by cyclic strains. Crack growth by pure fatigue process, for example, could be similar to the plastic blunting process discussed by Laird [52]. It is relevant in the 'Paris-regime' where fatigue crack grows by the striation mechanism. Also, in medium carbon steel, tests done in high vacuum showed no or very little R dependence [68] indicating that no K_{max}-dependent phenomenon is operative. The crack growth trajectory for the vacuum test closely follows the pure-fatigue line. In addition, with increasing frequency the trajectory map for many materials moves towards the pure-fatigue line. The crack growth trajectory deviates from this 45^{o} line, when additional processes other than pure fatigue contribute to the crack growth. The superimposed process can be an environmentally-assisted crack growth or any other monotonic modes of crack growth, where the K_{max}-dependency is involved [219]. In the case of SS316L(N) as in the present study, the superimposed transformation toughening process could lead to such deviation. The crack growth trajectory is similar to taking a series of 2D-cuts in the 3-D behavior of fatigue that involve da/dN-ΔK-K_{max} variables [189]. Hence the two-parametric nature is intrinsic to fatigue and cannot be correlated to crack closure which is an extrinsic factor. Crack closure, if present, forms an additional factor to be considered. The analysis points out that the R-dependence itself is an intrinsic phenomenon arising from the two-parametric nature of fatigue.

5.3 Fatigue crack growth analysis of SS316LN using unified approach

Fatigue crack growth data for the three nitrogen alloys 8N, 14N and 22N and the analysis using unified approach are presented below, taking each alloy in turn. Figure 5.5a & 5.5b respectively shows the crack growth rate data in terms of ΔK and K_{max} for 8N alloy, for different R-values. If crack growth rates are purely K_{max}-controlled (essentially governed by the monotonic plastic zone) then we expect the plots to collapse to a single band when they are plotted against K_{max}, i.e., with no significant R effects. On the other hand, if they are purely cyclic load controlled, then there should not be any R-dependence when plotted in terms of ΔK. Examination of Fig. 5.5a and Fig. 5.5b shows that the data are neither purely ΔK controlled nor purely K_{max} controlled. Careful examination of Fig. 5.5b, however, reveals that at low R -values (i.e.,≤ 0.25), the data are closely grouped (even though one can differentiate the data for individual R-values) but are spread out for $R > 0.5$. High resistance to crack growth (low da/dN) at high K_{max} values could be an indication of the increased toughness due to DIMT.

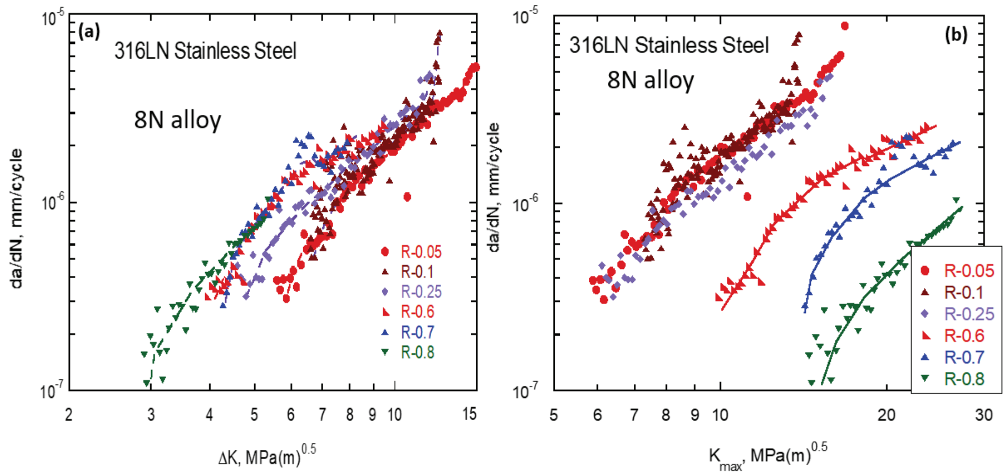

Figure 5.5 Fatigue crack growth rates of 8N alloy at various R-ratios as a function of a) ΔK and b) K_{max}.

Using the data in Fig. 5.5a, ΔK vs R for various selected crack growth rates can be plotted. Figure 5.6a shows these plots for three selected crack growth rates. A typical bi-linear behavior can be seen with ΔK nearly constant at very high R-values but increasing linearly with decreasing R until R = 0. The current study is focused only on the positive values of R. From these ΔK-R curves, the ΔK-K_{max} curves are plotted for selected crack growth rates, Fig. 5.6b. The ΔK-R bilinear plot (Fig. 5.6a) has been used to extract additional points at intermediate R values using interpolation techniques to obtain continuous ΔK-K_{max} curves. A family of such curves for various selected crack growth rates is used to define the limiting values, ΔK^* and K_{max}^*, corresponding to each da/dN value. Using these limiting values, the crack growth trajectory map for the material is drawn as shown in Fig. 5.7 for the 8N alloy. The trajectory deviates from the pure fatigue line $\Delta K^* = K^*_{max}$ indicating some superimposed K_{max}-dependent processes to be operative over and above the pure cyclic process. The crack growth rates will be predominantly determined by

K_{max} if the K_{max}-dependent process dominates, i.e., if the cyclic-load contribution is just enough to keep the crack sharp during loading and unloading cycle. This happens sometimes during corrosion-fatigue. In essence, the crack growth trajectory maps provide the relative roles of the cyclic (or amplitude ΔK-dependent) process and the monotonic (or K_{max}-dependent process. In addition, the trajectory map also indicates the crack path-history effects as it depends on the evolving da/dN curves. In the present case, the K_{max}-dependent process gets superimposed on the fatigue process. The presumption here is that this K_{max}-dependent process is the localized transformation toughening. Environmental effects can also contribute to this deviation from the pure-fatigue line. That aspect can only be evaluated when the tests are done in an inert environment. Next, the data for other variants with different N contents are presented and the implications of these data in terms of the transformation toughening are discussed.

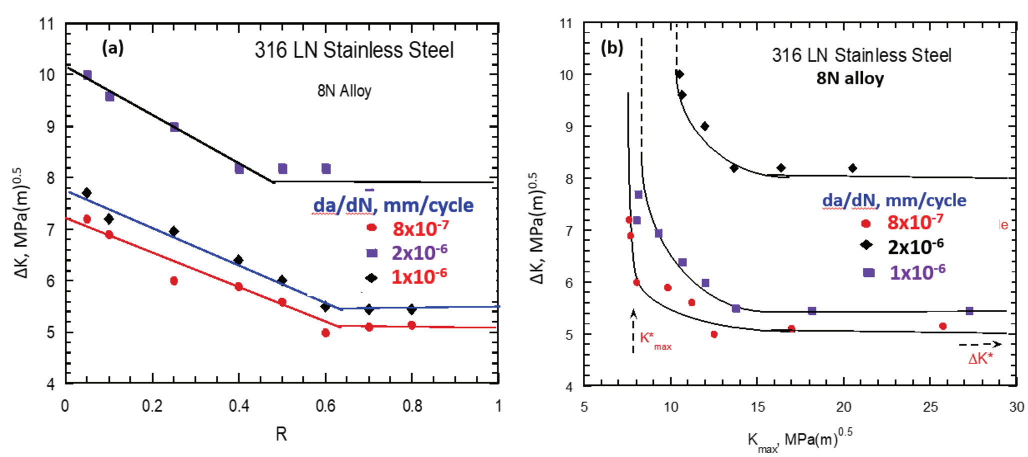

Figure 5.6 a) ΔK vs R for selected crack growth rates for 8N alloy showing a bilinear behavior. b) ΔK vs K_{max} curves for selected crack growth rates. The L-shaped behavior is shown with limiting values in terms of ΔK and K_{max} for each crack growth rate.

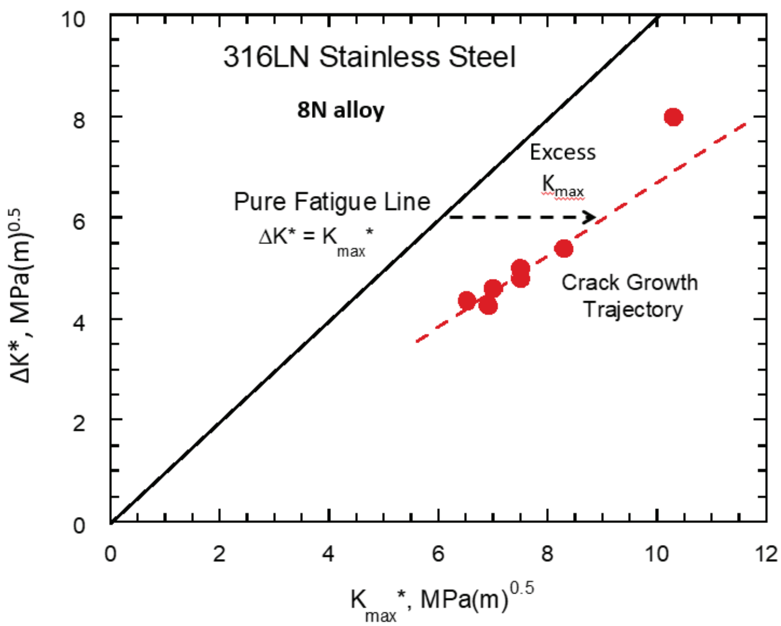

Figure 5.7 Crack growth trajectory map for 8N alloy, in terms of the limiting values ΔK^* and K^*_{max} for increasing crack growth rates.

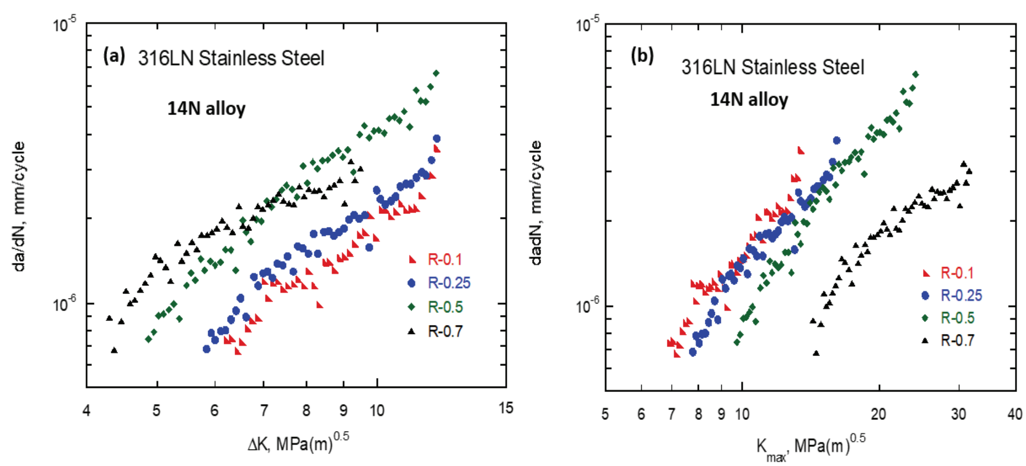

Figure 5.8 Crack growth rates for 14N alloy for various R values in terms of a) ΔK and b) K_{max}.

Figures 5.8 and 5.9 show the results for 14N alloy. Figure 5.8a shows the crack growth rates in terms of ΔK, and Fig. 5.8b in terms of K_{max}. Recall from Figs. 5.2 and 5.3 that crack growth rates for this alloy at ambient temperature ran parallel to those for 304 alloy at 77 K indicating the possibility of superimposed transformation toughening. Figure 5.8a shows these data as well as those at other R-values. It is interesting to compare the 14N data (Figs. 5.8a and 5.8b) with those of 8N in Fig. 5.5a and 5.5b. Figure 5.8b shows that the data for R = 0.7 in terms of K_{max} fall in a separate band compared to those for R= 0.1 and 0.25 which are somewhat close to each other. The data at R = 0.5 tend to approach the low R data, and more so at high K_{max} values. Figure 5.9a shows the typical ΔK-R bilinear behavior for the selected crack growth rates. Figures 5.9b and 5.9c show the ΔK-K_{max} curves for various crack growth rates covering the full range of crack growth rates. In Fig. 5.9b that corresponds to low crack growth rates (< 1.3x10^{-6} mm/cycle), the ΔK-K_{max} vary smoothly, but with increase in crack growth rate (or increasing K_{max} values) the L-shaped curve becomes more and sharper, Fig. 5.9c. Data at R = 0.7 helps in defining the limiting value of ΔK* while the data for the rest of the R values clearly define the K_{max}* value. The results are the reflection of the trends in the crack growth rate data in Fig. 5.8b where the data for R = 0.1, 0.25 and 0.5 are nearly merging with each other at high growth rates (>2.0x10^{-6} mm/cycle), while the data at R = 0.7 remain aloof. The effect is less pronounced for 8N alloy where the merging of the FCG data occurs only for R = 0.05, 0.1 and 0.25 while the data at higher R values spread widely, see Fig. 5.5b. Figure 5.9d shows the crack growth trajectory map for 14N steel depicting the variation of the two limiting values with increasing crack growth rate. Within the spread of the data, a representative line can be drawn showing that the data deviates from the pure fatigue line, indicative of some superimposed K_{max}-dependent process contributing to the crack growth resistance.

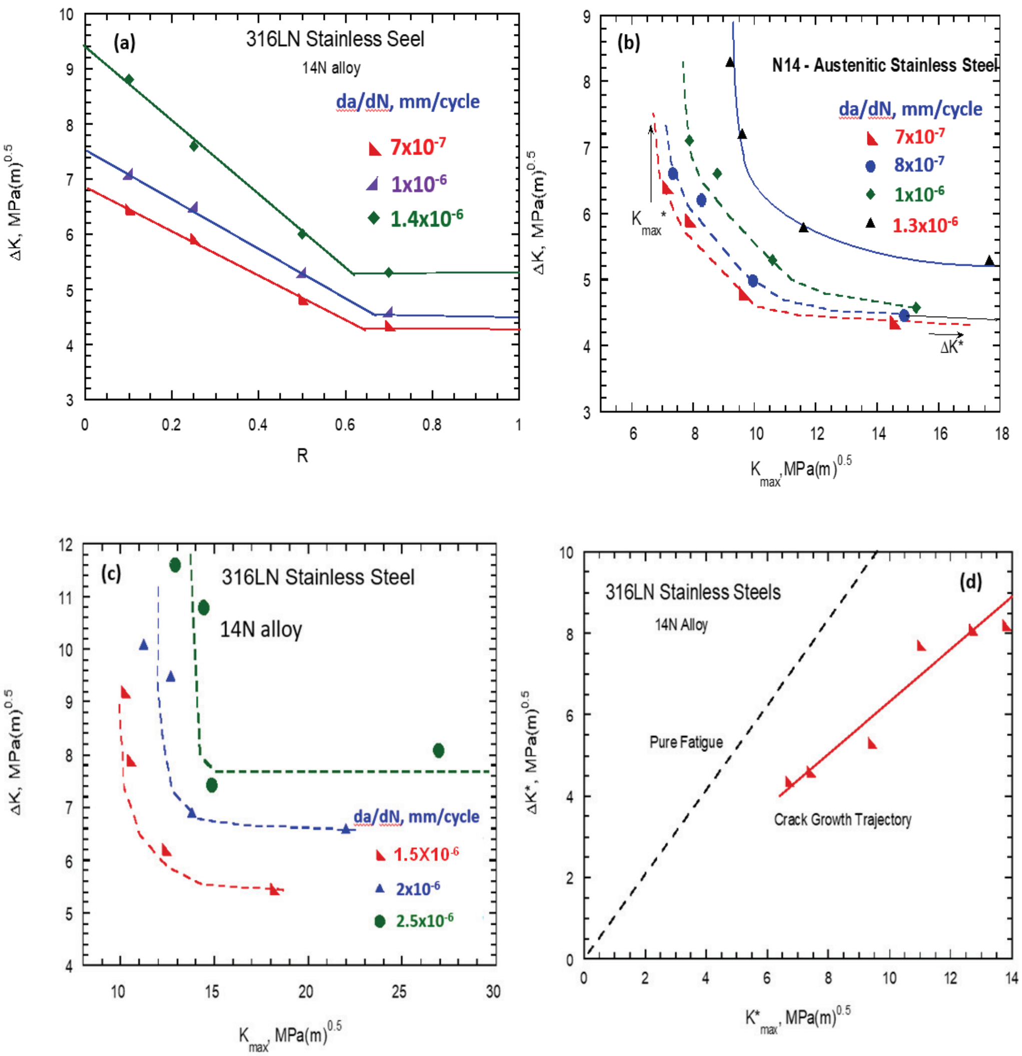

Figure 5.9 a) ΔK-R curves and b) ΔK -K_{max} curves for the N14 alloy for selected crack growth rates. Limiting Values ΔK^* and K_{max}^* for each crack growth rate are shown. c) ΔK - K_{max} curves for the N14 alloy at higher crack growth rates. d) Crack growth trajectory map for the N14 alloy.

Figures 5.10a and 5.10b show the crack growth rates in 22N alloy in terms of ΔK and K_{max}, respectively, for various R-values tested. A close examination of Figs. 5.10a and 5.10b indicates that the data are much closer in terms of ΔK than in terms of K_{max}. Nevertheless, even in terms of K_{max}, the data for R = 0.1, 0.25 and 0.5 are somewhat closer compared to those for R = 0.7, considering that it is in log-log scale.

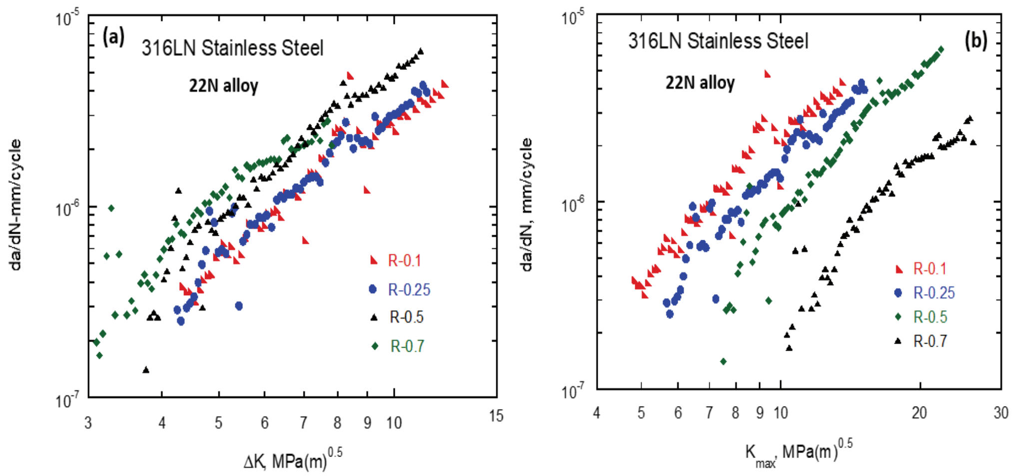

Figure 5.10 Crack growth rates for the 22N alloy for various R values in terms of a) ΔK and b) K_{max}.

Figure 5.11 shows ΔK-R data with some interesting features. Instead of normal bilinear curve, there appears to be a second plateau of ΔK at low R- values, although the extent of data is limited. At the high R end, we always expect the data to reach a plateau for R> 0.7. This behavior is reflected in the ΔK-K_{max} plots, Figs. 5.12a and 5.12b, except that at very high crack growth rates the second plateau seems to disappear, Fig. 5.12b. In this case, the limiting values of K_{max} are defined at the beginning of second plateau at low R values, as indicated in Fig. 5.12a.

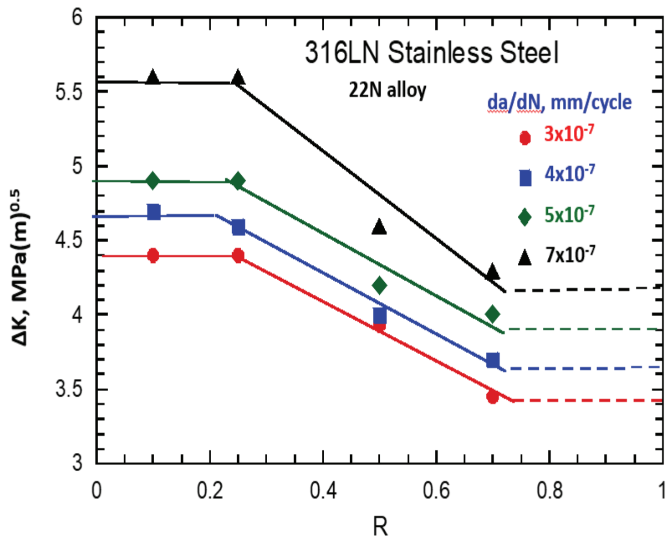

Figure 5.11 ΔK-R plots for 22N alloy. Within the limited data, the figure shows that ΔK levels off at low R values. At high R values the data are expected to level off for $R \geq 0.7$. Only dashed lines are shown as the data are limited.

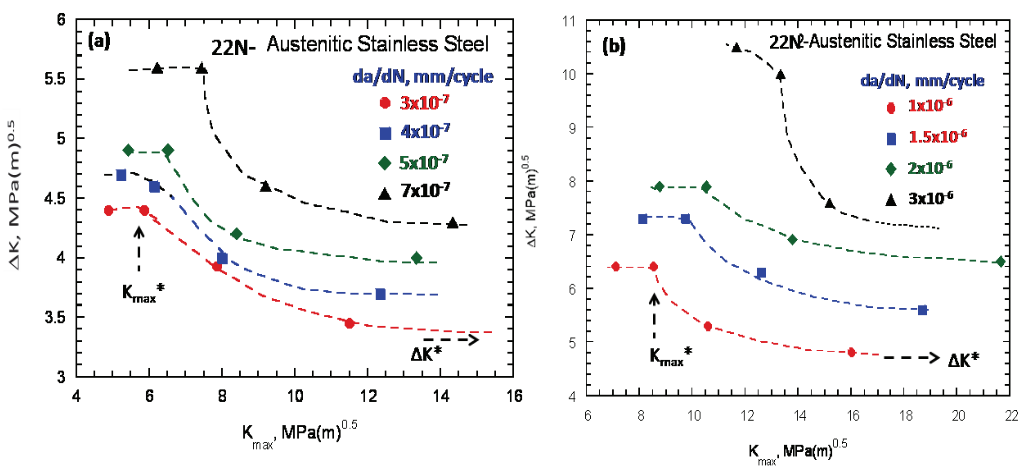

Figure 5.12 ΔK-K_{max} curves for the 22N alloy a) at low crack growth rates and b) at higher crack growth rates.

Normally, the observed flat ΔK regime at low R-values is a sign of the beginning of another L-shaped curve characteristic of a second operating mechanism. Many such cases have been observed where the operating mechanism switches from one to another as R increases [29, 189]. In those cases, one can observe two clear L-shaped curves merging with one another as R increases.

Figure 5.13 shows the crack growth trajectory map for 22N. One can draw two separate lines indicating that there are two distinct mechanisms operating. At crack growth rates below $1x10^{-6}$ mm/cycle, the trajectory line is close to and parallel to the pure fatigue line while above $1x10^{-6}$ mm/cycle, the line moves farther away from the pure fatigue line indicative of a separate super imposed K_{max} dependent process to be operative. It may be recalled from Figure 5.3 that crack growth rate data for 22N alloy move towards the 14N and 8N data, although this range appears to be small in the log-log scale. Figure 5.3, of course, shows the comparative data only at one R-value but indicates that transformation induced toughening is possible at high stresses even in 22N alloy. The results in Fig. 5.13, therefore, are self-consistent as it indicates a change in mechanism as the stresses become increasingly larger.

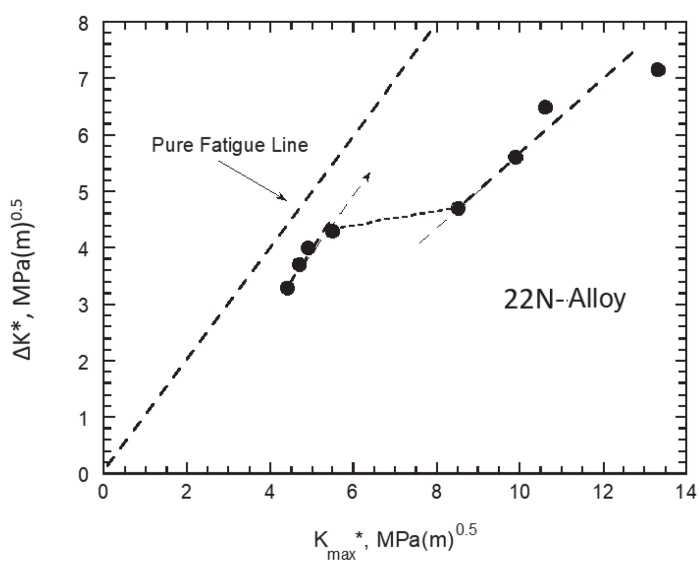

Figure 5.13 Crack growth trajectory map for the 22N alloy.

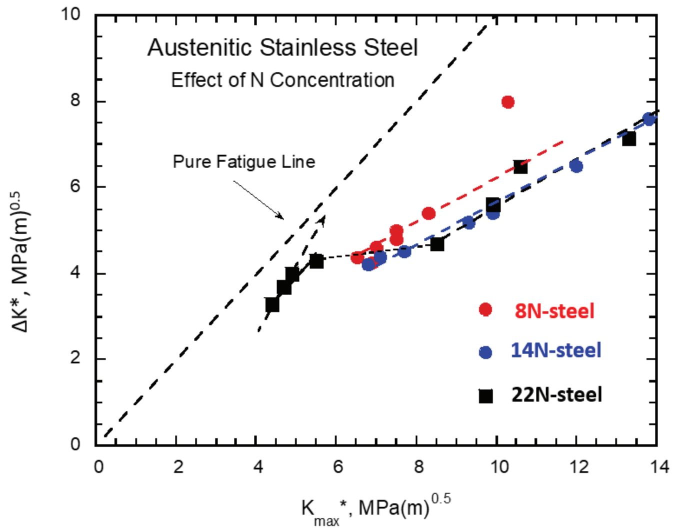

Figure 5.14 Crack growth trajectory maps for different nitrogen 316L stainless steels. The K_{max} dependent processes including DIMT make the trajectory to deviate from the pure fatigue line.

Figure 5.14 compares the crack growth trajectory maps of the three N alloys. At high crack growth rates (or high stresses/strains) the crack growth trajectories are close to each other and run parallel, but deviating from the pure fatigue line. Only in the 22N alloy, a separate mechanism at low *R*-values is clearly evident. This may be related to absence of transformation toughening due to the high N content.

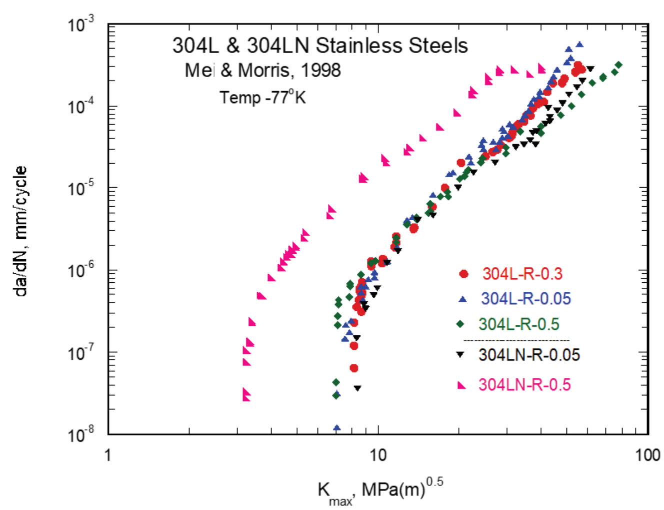

Figure 5.15 Crack growth rates in 304 Stainless steels as function of K_{max}, reported by Mei and Morris [142, 143].

5.4 Analysis of FCG data for other Austenitic Stainless Steels:

While Fig. 5.2 provides the data of Mei and Morris [142, 143] at one *R*-value, they have done tests at three *R*-values based on which they have negated the applicability of crack closure concept to account for the *R* effects. Their data are analyzed here using the two-parametric approach, even though the range of *R*-values they investigated is limited. Figure 5.15 shows their data in terms of crack growth rates as a function of K_{max} at 77 K for the three *R*-values that they have tested. The plasticity induced austenitic to martensitic transformation occurs more abundantly at 77 K in the nitrogen free 304L. Hence, the *R* effects reflect the transformation effects. The ΔK-R plots using this data for selected crack growth rates are presented in Fig. 5.16. Note that Fig. 5.16 is on linear scale in contrast to Fig. 5.15 which is a log-log plot. Fig. 5.16a shows the ΔK-R curves at low crack growth rates. Considering that ΔK-R curves follow a bilinear behavior with ΔK reaching some plateau for $R \geq 0.7$, the plot is extrapolated to $R = 0.7$ and then a plateau indicative of the minimum ΔK needed for crack growth is drawn. At high crack growth rates, Fig. 5.16b, the plateau in ΔK-R curves occurs at *R* values lower than 0.7. This earlier plateau at $R=0.5$ in Fig. 5.16b indicates that a higher minimum ΔK is required to enforce these growth rates in this alloy.

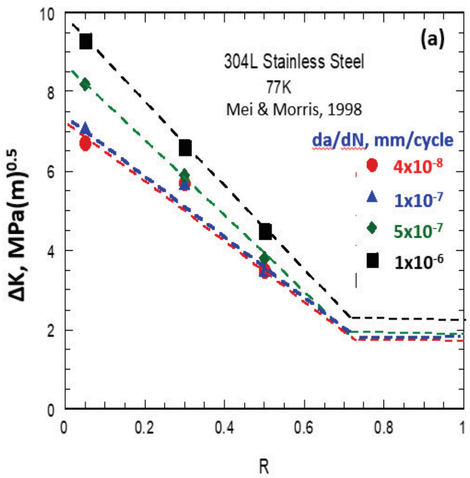

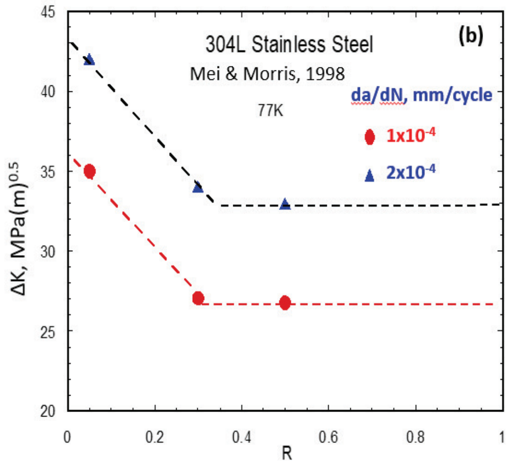

Figure 5.16 Plots of ΔK - R bilinear curves for selected (a) low and (b) high crack growth rates from Fig. 15. Bilinear curves are drawn through the limited data by extrapolation to high R values and a constant ΔK value at $R \geq 0.7$.

The procedure that has been used, therefore, is self-consistent. Fig. 5.17a provides the ΔK-K_{max} curves for the selected crack growth rates in Fig. 5.16a. Using the limiting values, ΔK^* and K_{max}^*, crack growth trajectory map is generated as shown in Fig. 5.17b. There is a significant shift from the pure fatigue line. The authors have clearly established that the increased crack growth resistance at 77 K arises predominantly from the stress induced transformation toughening. The transformation occurs due to crack-tip plasticity that forms a monotonic plastic zone [220,221] ahead of the crack tip.

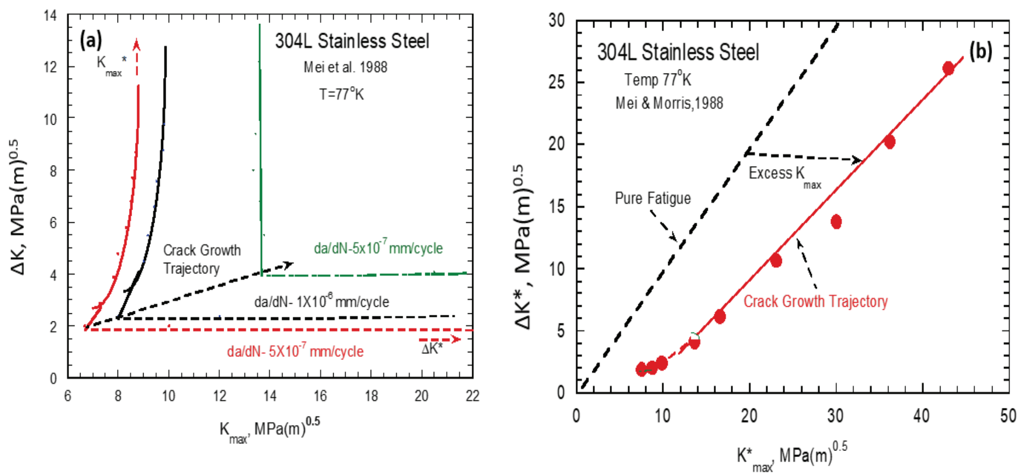

Figure 5.17 a) ΔK-K_{max} curves for 304L alloy at some selected crack growth rates, b) crack growth trajectory path for the alloy at 77 K, using Mei & Morris data.

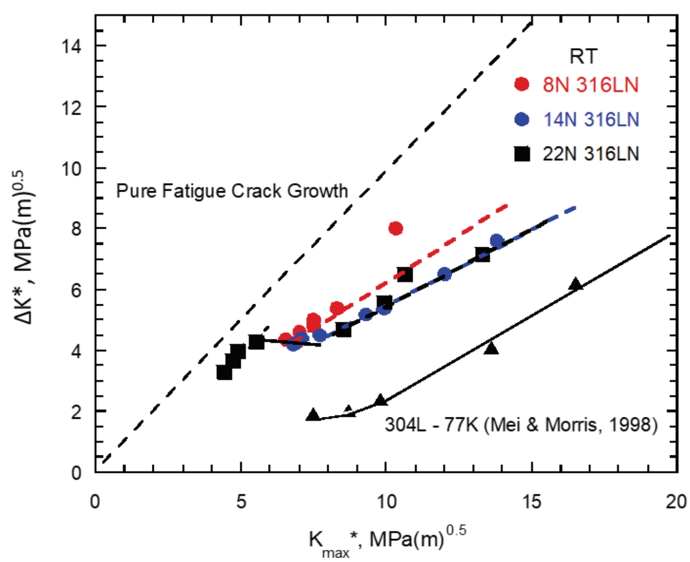

Figure 5.18 Comparison of trajectory maps of 8N, 14N and 22N, 316L alloys with that of 304L at 77 K where transformation induced toughening is known to occur.

The deviation or shift in the trajectory map from the pure fatigue line observed in Fig. 5.17b can be clearly attributed to the DIMT ahead of the crack tip, based on the extensive analysis by Mei and Morris [142, 143]. They have clearly ruled out the crack closure as contributing factor for the observed *R* effects in this alloy.

Considering the above results, we can now compare the trajectory data on 316L from the present work with those of Mei and Morris. The results are shown in Fig. 5.18. Based on these results, the following observations are made. (a) The present results on 316L are somewhat parallel to those of Mei and Morris. (b) The shift in the trajectory map observed for 316L at 298 K is not as pronounced as that observed in 304L at 77 K. This has to be expected both from Fig. 5.3 and from the fact that 304L is more prone to DIMT. Also, their tests were done at a lower temperature (77 K) where the DIMT is more pronounced. c) Crack growth trajectory maps provide some indication that there are additional superimposed processes over and above the pure fatigue process. d) Such an analysis is possible only when we consider the two-parametric nature of fatigue and analyze the data systematically for a full range of *R*-values.

5.5 Comparison with other published data on 316 Stainless Steels

There has been some work on the nitrogen containing 316 stainless steels at 77 K by Vogt et al. [148] in 1991, with (316LN containing 0.24N) and without nitrogen (316L, containing 0.03N). The nitrogen content in their LN alloy is close to the high N alloy (22N) in the present case. At 77 K, stress induced transformation should be significant in comparison to that at room temperature. On the other hand, presence of high levels of N may inhibit the transformation by stabilizing the austenite. Their results at 77 K, are compared with the room temperature results from the present study in Fig. 5.19. Though their results are limited to $\Delta K > 15$ MPa.m$^{0.5}$, it is noted that in the overlapping range, the two results are similar. Since at high ΔK, based on Fig. 5.2, there appears to be transformation toughening even in 22N alloy, it is possible that the merging of the room temperature data from the present study with theirs could be due to the same transformation toughening process.

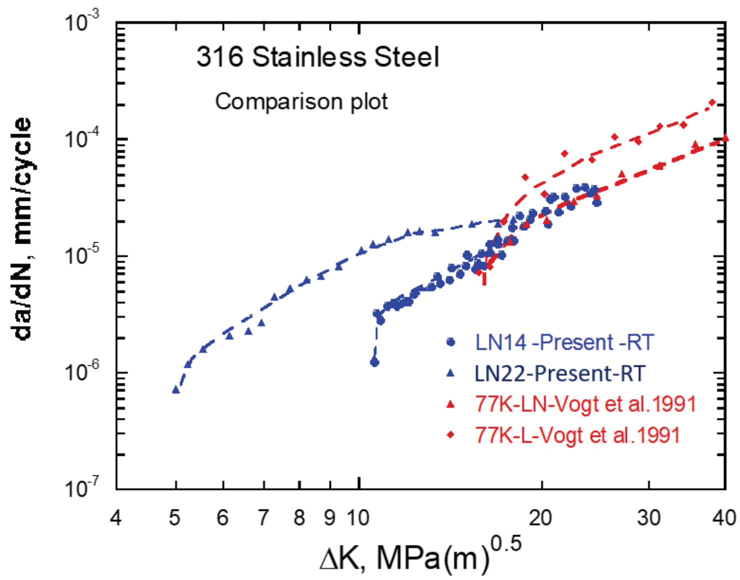

Figure 5.19 Comparison of present 316 SS data with those of Vogt et al., but tested at 77 K [148]. 14N, and 22N

The authors argue that in the 316LN alloy, the crack growth resistance is dominated by the planar slip due to the significant reduction of stacking fault energy by nitrogen additions. Also, the 316L alloy in their study, due to the lower nitrogen content, should be more prone to DIMT than 316LN. The role of slip planarity also is more important at lower temperature. Their TEM analysis, however, shows some amount of DIMT even in the 316LN alloy. Nevertheless, our results are consistent with those published in the literature data that show various degrees of DIMT affecting FCG resistance, depending on the N concentration. Data of Vogt et al. [148] were limited to one *R* value, and hence not sufficient to extract the crack growth trajectory maps for their alloys.

5.6 Microstructural analysis

Fractographic and microstructural analysis was done to evaluate the material response during the fatigue crack growth. Figure 5.20 shows the grain-size distribution in the three nitrogen alloys. The average grain size is around 70±8 μm for both 8N and 14N alloy. The grain size distribution of 8N is broader. Large grains, esp >80 micron, fraction is much more in 8N. The averge grain sizes appears to be 65, 55 and 45 microns for 8N, 14N and 22N. However, this variation is monotonic and 22N is expected to have a better FCG resistance from grain size point of view. However, there is a lot of overlap in the grain size distributions among the three alloys. This difference in grain size is not significant and therefore, the grain size may not be a major contributing factor in contributing to the differences in FCG behavior among the three alloys.

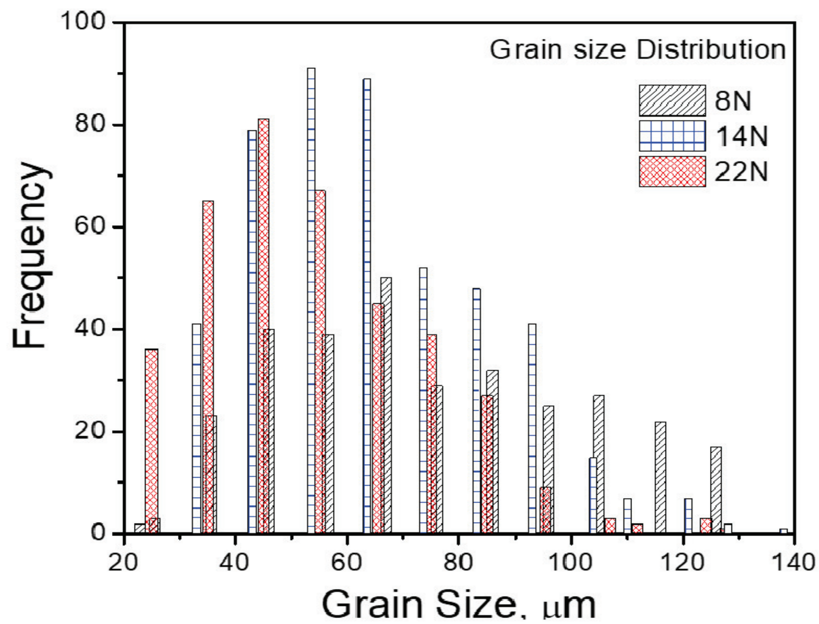

Figure 5.20 Grain size distributions in the three-nitrogen containing 316L stainless steels.

Figures 5.21a & 5.21b show the fracture surfaces of the three alloys at low and high crack growth rates. There appears to be an increasing faceted mode of crack growth with increasing N content. Similar observation has been made in the nitrogen containing stainless steels [148], particularly in materials tested at 77 K. The authors attributed this to pronounced planar slip that is presumed to have been facilitated by the reduction in the stacking fault energy by nitrogen. The faceted growth was more pronounced at low crack growth rates. Figure 5.21 also shows that faceted mode of crack growth was more pronounced in the 22N alloy compared to that in 14N and 8N alloys.

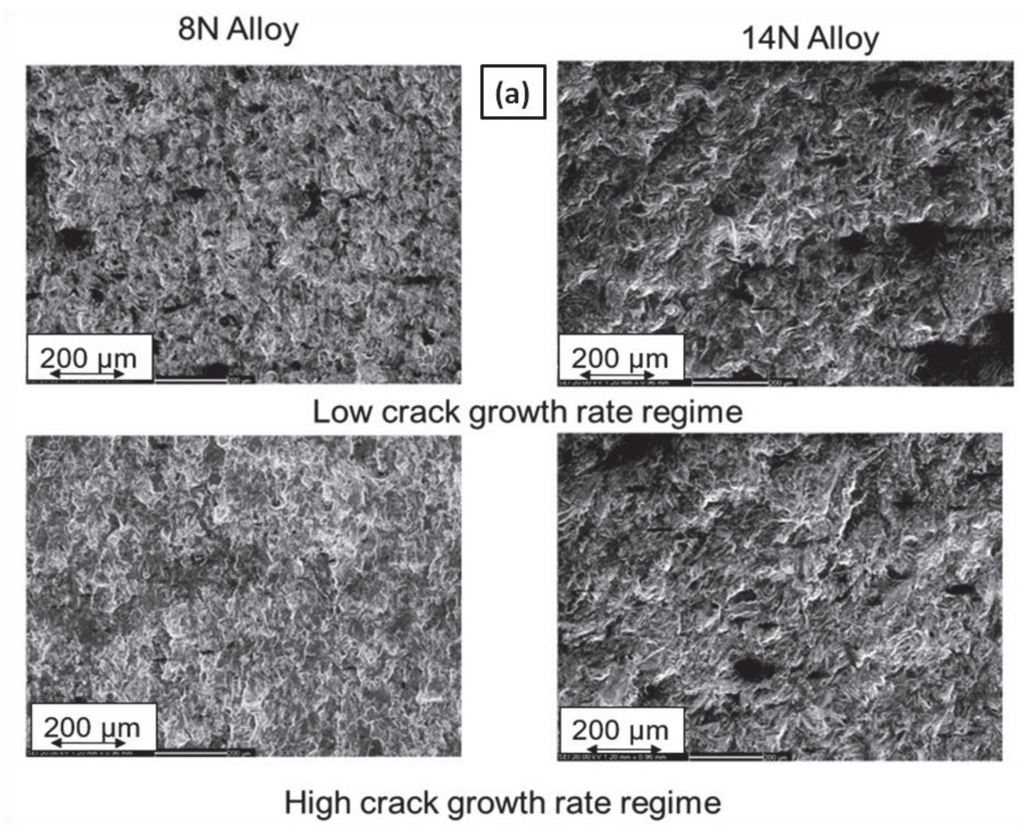

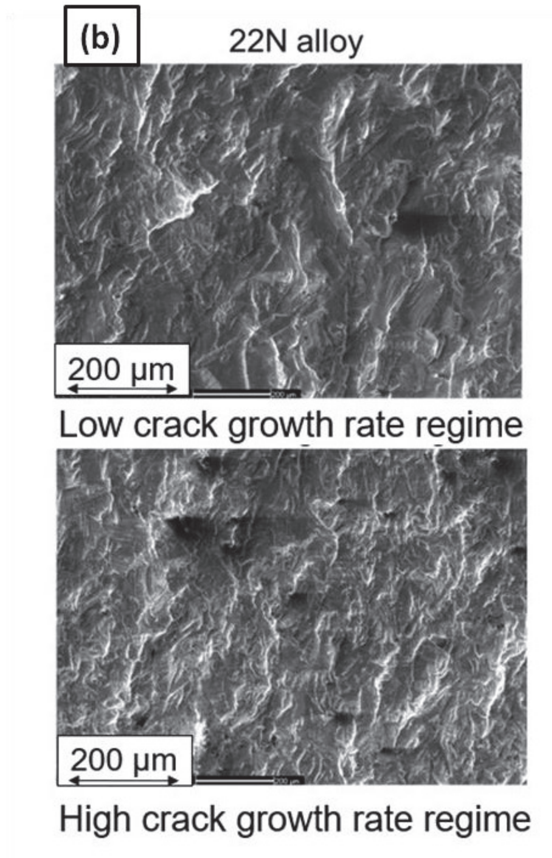

Figure 5.21 a) Fracture surfaces of 8N (left) and 14N (right) alloys. Crack growth from top to bottom. b) Fracture surfaces of 22N Steel. Crack growth direction is from top to bottom (high crack growth rate $da/dN > 10^{-6}$ *mm/cycle*).

Figure 5.22 shows the TEM pictures of the three alloys where the samples were taken near the fracture surfaces. It may be noted that with increasing nitrogen content shear band structure is more evident, Fig. 5.22b and 5.22c. Similar band structure was observed by Hedström and Odqvist [222, 223], and by Vogt et al.[148] in their 0.24% sample tested at 77 K. Vogt et al, upon analysis, found that these bands could be related to the formation of ε and/or α' martensitic phases formed due to deformation. The reduction in the stacking fault energy by nitrogen and the resulting planar slip can also contribute to the shear-band formation.

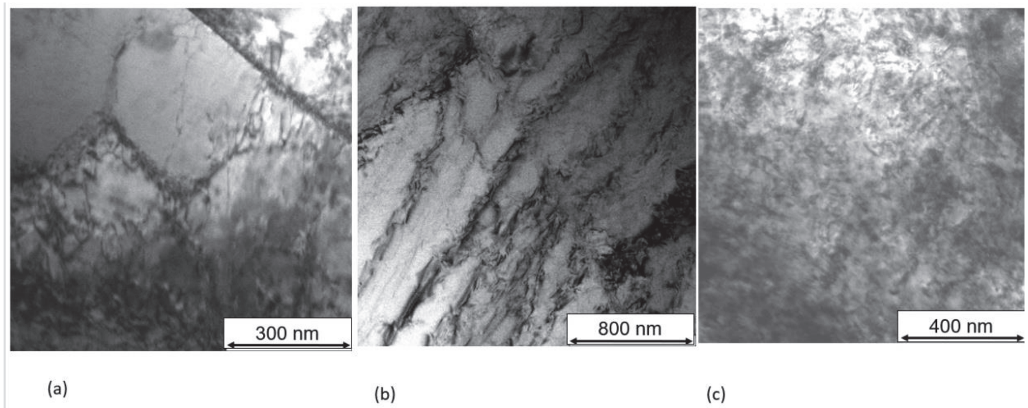

Figure 5.22 TEM images of FCG tested samples –(a) 8N (b) 14N and (c) 22N.

Figure 5.22a shows more or less equiaxed dislocation cell structure in the 8N test sample. The shear band formations as seen in Fig. 5.22b & 5.22c can promote the faceted mode of crack growth along the slip systems. Hence, such mode of crack growth is more dominant in close-packed planes, as in HCP and FCC systems, particularly at low crack growth rates close to the thresholds. Hence, some degree of faceted mode of crack growth is expected in austenitic stainless steels. Shear band formation has been observed in these materials [223], which promote the subsequent the strain-induced localized martensitic transformation and toughening. Thus, the roles of planar slip and DIMT are intertwined and it is difficult to separate the two.

Although nitrogen forms an interstitial in the austenitic steel and is projected to enhance the stacking fault energy (SFE), more detailed first-principle calculations indicate that the SFE is not a monotonic function of N concentrations [214]. The SFE initially increases with N addition but decreases again with further increase reaching a minimum value. Hence, there is an optimum N concentration that leads to a minimum in SFE and hence maximizes the planarity of slip. Thus, nitrogen, while contributing to the stability of austenite on one hand, depending on the

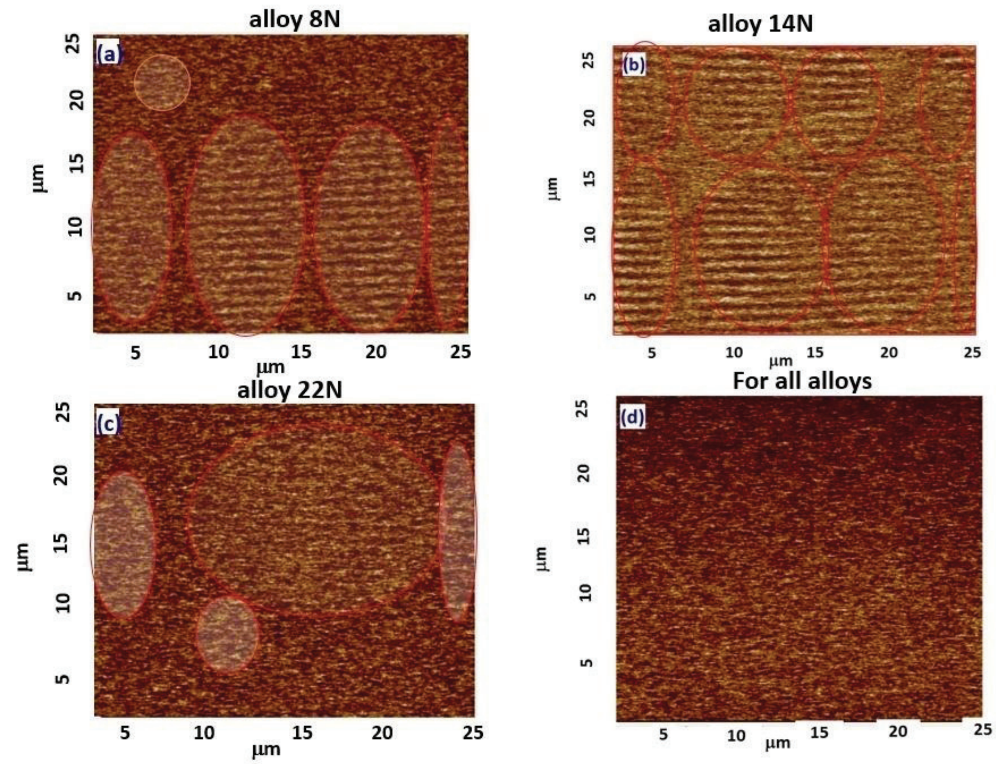

Figure 5.23 Typical magnetic domains obtained using MAFM for (a) 8N, (b) 14N, (c) 22N, all corresponds to ΔK of 15 MPa.m$^{0.5}$. Fig. d corresponds to $\Delta K \sim 5$ MPa.m$^{0.5}$ and the domain sizes are small, and the densities are similar for all the three alloys.

concentration also promotes the slip planarity on the other, thereby promoting the faceted mode of crack growth. These effects are reflected in both fractographs as well as TEM micrographs with enhanced shear band formation. Formation of stacking faults and restricted slip can also enhance the DIMT. Hence Vogt et al. [148] also concluded that the role of N in the austenitic stainless steels is somewhat complex and varies with the concentration. For example, nitrogen concentration higher than 0.24% in austenitic stainless steels can contribute to nitride formation and also can cause subsequent embrittlement depending on the distribution of nitrides.

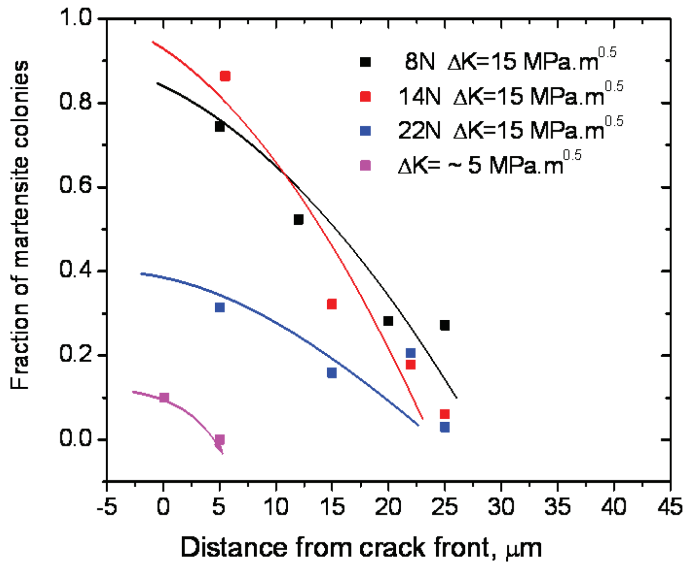

Figure 5.24 The fraction of the martensite colonies observed as a function of the distance from the crack tip for $\Delta K \sim 5.5$ and 15 MPa.m$^{0.5}$.

The question, then, remains in terms of the extent of deformation induced martensite in the samples in the present study. To address that issue, ferro-magnetic nature of the martensite is made use of to evaluate the intensity of martensitic transformation ahead of the crack tip. The extent of the magnetic domains present was measured as a function of distance from the crack (perpendicular to the crack growth direction) using Magnetic based Atomic Force Microscope (MAFM). The MAFM images are presented in Figs. 5.23 for the three alloys. Figures 5.23a, 5.23b, and 5.23c are for 8N, 14N and 22N respectively at 15 MPa.m$^{0.5}$. In these figures, the observed serrated regions are characteristic of the magnetic domains present. In each figure, the magnetic domains observed are encircled for easy identification. There is a significant increase in the density of these domains from 8N to 14N, however, for 22N, there is a notable decrease. At low ΔK levels (~5 MPa.m$^{0.5}$) the observed magnetic domains were similar but insignificant in all the three steels; a typical example is shown in Fig. 5.23 d. Thus, the density of the domains a) is higher at higher ΔK value, and b) decreases with distance from the crack. They are limited to the intense deformation zone, i.e., the plastic zone, which is around 160, 120 and 90 μm for 8N, 14N and 22N alloys, respectively at the corresponding thresholds. The average area fraction of such domains near the crack has been measured for a crack length of 0.1 mm for specimens of each alloy at low (~5.5 $MPa.m^{0.5}$) and high (15 $MPa.m^{0.5}$) ΔK values. These results for the three alloys are compared in Fig. 5.24. It shows that the domain densities are somewhat similar in both 8N and 14N alloys. The differences between these two alloys are quite small. On the other hand, the domain density in the 22N alloy is significantly small in relation to the other two alloys, however, the trend is similar to 8N and 14N. These results are consistent with the crack growth data in Fig. 5.2. At low ΔK value, the density is quite low for all the three alloys. Only one curve is shown representing all the three alloys. Thus, the results of the present microstructural analysis are consistent with the published data on the effect of nitrogen on the transformation toughening in these austenitic stainless steels.

5.7 Conclusions

The effect of nitrogen concentration on the FCG resistance of SS316L(N) at ambient conditions (laboratory air) was evaluated. For each of the three concentrations selected in this study, FCG rates were determined as function of load ratio R. The results were analyzed using the two-parametric approach involving ΔK and K_{max} parameters. Crack growth trajectory maps were constructed and compared with those determined for other austenitic steels using the literature data, where the transformation toughening has been adequately established. The results indicate the similarity in the crack growth trajectories, establishing that the increased crack growth resistance in the current nitrogenized alloys is due to transformation toughening. It is shown that the microstructural analysis on these three nitrogen alloys are consistent with the published data indicating that deformation induced martensitic transformation is occurring ahead of the crack tip contributing to the enhanced toughening. The extent of this transformation decreases with increase in nitrogen content. The benefit of this transformation offsets that from other advantages of presence of N, such as grain refinement and enhanced strain hardening (This aspect not covered in the present study). The results from the present study indicate that the optimum nitrogen content to derive the maximum benefit is dependent on its effect on the DIMT formation, in addition to the other well-known effects of N such as solid solution strengthening, reduced stacking fault energy, grain refinement and enhanced strain hardening.

CHAPTER 6

FATIGUE CRACK GROWTH BEHAVIOUR OF SS316(N) WELD AND COLD WORKED SS316L(N) – ANALYSIS USING THE UNIFIED APPROACH

CHAPTER 6 : FATIGUE CRACK GROWTH BEHAVIOUR OF SS316(N) WELD AND COLD WORKED SS316L(N) - ANALYSIS USING THE UNIFIED APPROACH

6.0 Introduction

As discussed in Chapter 2: Literature Survey, during manufacturing of components, welding and cold working are employed extensively, which introduce microstructural, such as δ-ferrite (in ausenitic stainless steel welds), increased dislocation density etc., and mechanical changes such as residual stresses in the material. In this chapter, the fatigue crack growth (FCG) behavior of SS 316(N) weld and cold worked SS316L(N) base materials has been evaluated at different R-values at room temperature and compared with that of the base metal in solution annealed condition. The FCG data were analyzed using the Unified Approach that considers the two-parametric (ΔK and K_{max}) nature of fatigue. The effects of R in both the base and weld metals are explained without invoking any extrinsic parameters, such as plasticity-induced crack closure. Since the residual stresses are of monotonic type, they affect the crack growth via the K_{max}-parameter. The crack growth trajectory plots were developed, and they show the relative changes (with reference to that of the solution annealed base metal) in the two crack tip driving forces, ΔK and K_{max} required to overcome the FCG resistance for a range of crack growth rates.

6.1 Back ground

The fabrication of large components and structures made up of SS316LN steel invariably involves bending operation which creates the cold work in the material and welding. By adjusting the chemical composition of the consumable electrodes, the weld metal of this steels is ensured to contain 3 to 7% δ-ferrite which helps to balance between resistance to hot-cracking during welding and embrittlement of the weld metal during prolonged service exposure at elevated temperatures [14]. Generally, the welds are also potential sites for defects such as porosity, lack of fusion/penetration, undercut, cracks etc. They are subjected to thermo-mechanical cycling, in addition to creep [10, 14,], fatigue [18], creep-fatigue [10], etc. Hence, for assessing the structural integrity, it is necessary to evaluate the FCG resistance of these welds. The extensive work on the FCG characterization of SS316L(N) base material is reported in the previous chapter. Limited studies were earlier carried out in the same laboratory on the weld metals [152, 153]. In this chapter, an extensive analysis of the FCG behaviour of SS316(N) welds as a function of load ratio, *R,* is discussed. (The weld is prepared using 8N, the variant of SS316L(N) with 0.08% N content. L indicating low (<0.03%) carbon content has been dropped in the designation of the weld) since the weld deposit contains about 0.05% C. The effect of residual stresses on the crack growth trajectory is highlighted. Also, since cold work introduced during manufacturing is likely to introduce residual stresses, the effect of cold work on the FCG behavior as reflected in the crack growth trajectory is examined.

6.2 Fatigue crack growth behaviour of SS 316 (N) weld

Austenitic stainless steel welds normally are not subjected to any post-weld heat treatment before they are deployed in service. The mechanical properties of these welds are influenced by the presence of (a) a duplex microstructure, (b) a high dislocation density and precipitates formed during the cooling, and (c) residual stresses introduced during welding. The results presented in the previous chapter on the FCG resistance of SS316L(N) base material indicated that, while nitrogen stabilizes the austenite to some extent, there was sufficient deformation-induced transformation toughening ahead of the crack tip that contributed to the *R*-dependence. Presence of compressive residual stresses in weld metal can also enhance its FCG resistance in comparison to that of the base metal. The FCG properties of the SS316(N) weld metal are evaluated at ambient temperature at various *R* values and the results are compared with those available in the literature on the crack growth behavior of other weld materials.

6.2.1 Hardness Measurement

In order to gain a rough understanding of the variations in the mechanical properties of different regions across the weld, Vicker's hardness measurements(10 kg load) were made in the transverse direction covering the base and weld regions on both the cap side locations (C-L) and the root side locations (R-L). Several sets of such measurements were made along the length of the weld. The results are presented in Fig. 6.1. Open symbols are for root side and closed ones for the cap side. Though the scatter is high, the results presented in Fig. 6.1 show that the weld is significantly harder than the base metal. Also, the scatter band for the root side is significantly above that for the cap side. The difference in hardness between the base and weld materials is partly due to that in the a) composition and b) microstructure, specifically the presence of δ-ferrite, higher dislocation density due to the cooling strains and precipitation during the weld thermal cycles. However, the higher hardness in the root side than the cap side points to the role of compressive residual stresses, which is expected to be higher at the root side due to higher levels of constraints.

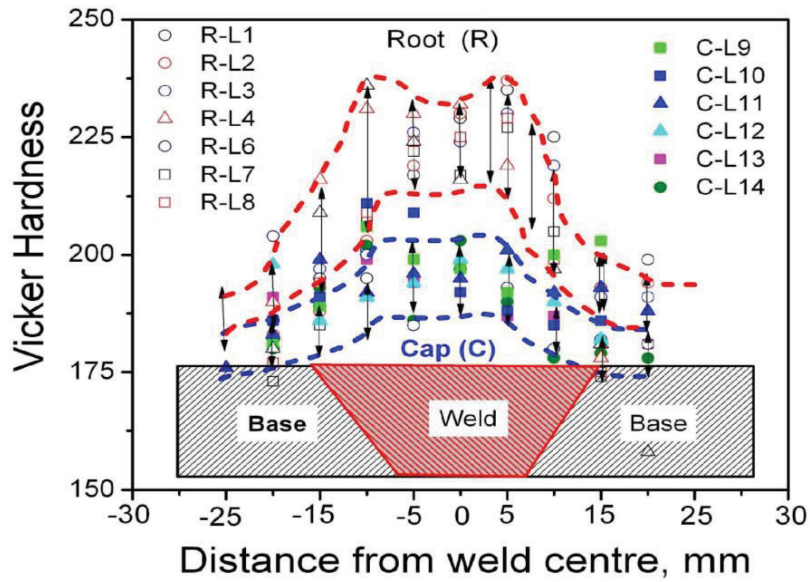

Figure 6.1 Hardness profile across the weld

6.2.2 Fatigue crack growth behaviour of SS316(N) weld

The fatigue crack growth rates, da/dN, in the weld metal for different R values are shown in Figs. 6.2a and 6.2b as a function of ΔK and K_{max}, respectively. From a comparison of the two figures, it is clear that the data for different R values fall in a smaller scatter band when plotted in terms of the K_{max} parameter (Fig. 6.2b) than in terms of the ΔK (Fig. 6.2a). It implies that the K_{max} is more dominant controlling parameter for characterizing the crack growth in this weld. The results are also consistent with the higher hardness in the weld, Fig. 6.1. The crack growth rates in the base and weld metals are compared in Fig. 6.2c, which shows that at a low R (R=0.1), the FCG resistance of weld metal is very high in comparison with that of the base metal. Considering that this is due to the presence of high compressive residual stresses, these effects are less pronounced at R=0.7. Figure 6.3 shows a schematic presentation of the effect of residual stress on the two crack driving forces ΔK and K_{max}. It shows that while ΔK is unaffected, the operating K_{max} at the crack tip gets affected by the residual compressive stress, for a given crack length. This aspect will be discussed next.

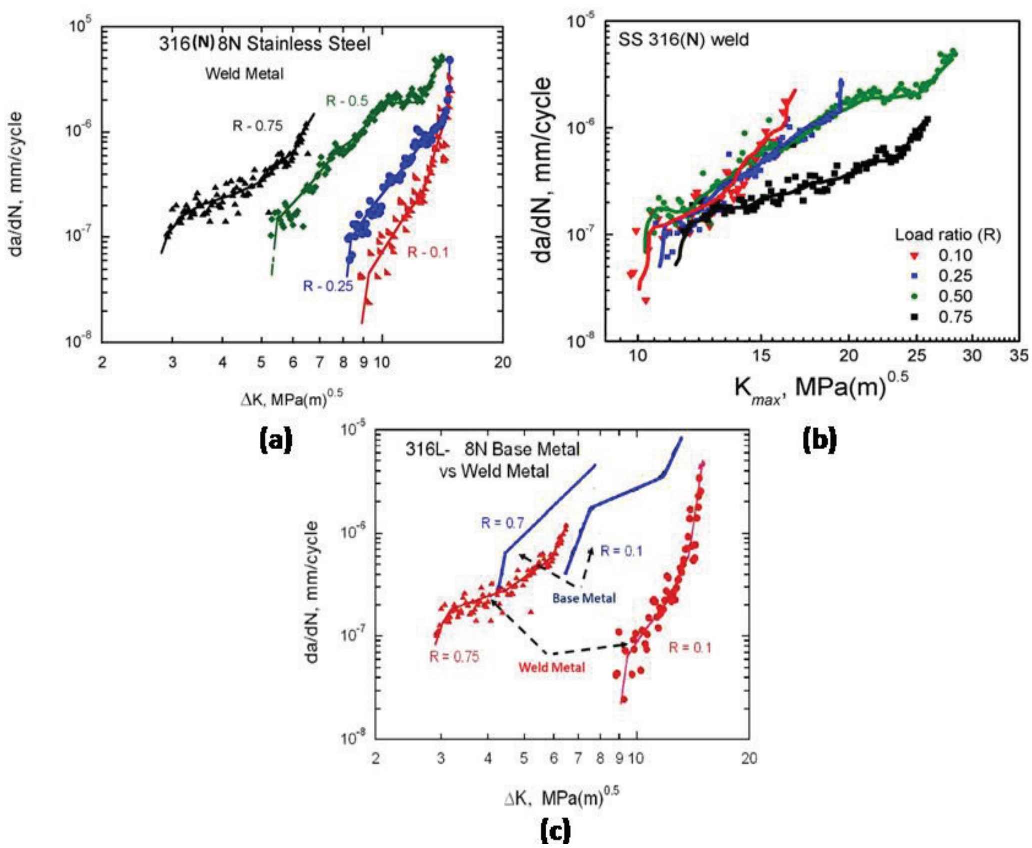

Figure 6.2 (a) Crack growth rate as functions of (a) ΔK, (b) K_{max} and (c) comparison of base and weld metal at low and high R values

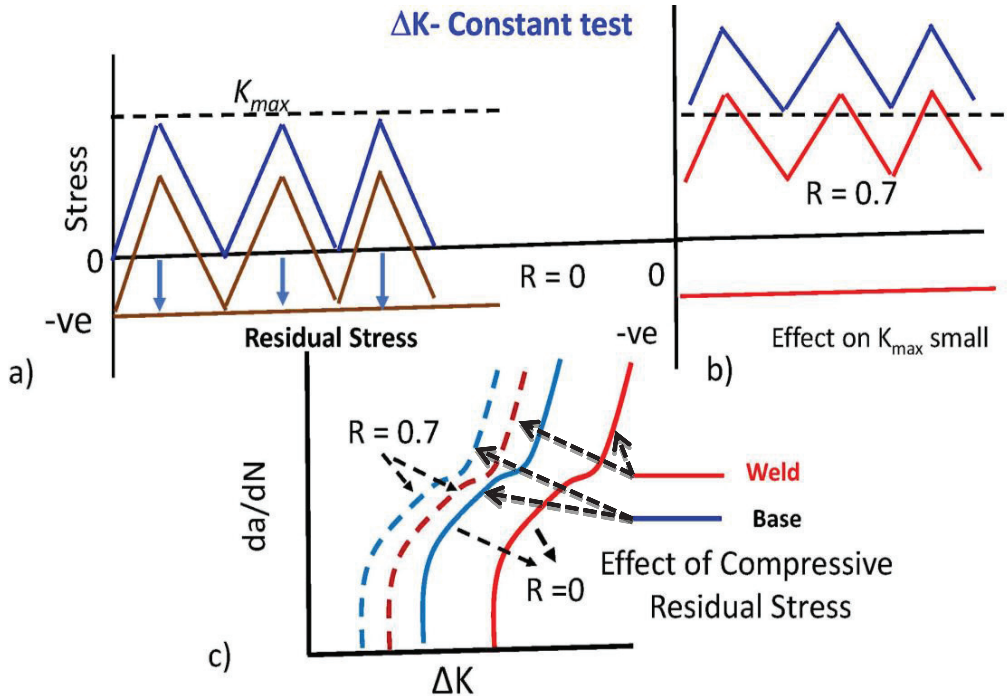

Figure 6.3 (a-c) Effect of compressive residuals stresses on the amplitude, $\Delta\sigma$ and maximum stress σ_{max} and their effects on fatigue crack growth rate. a) and b) correspond to crack length constant during the three cycles shown.

6.3 Analysis of Crack Growth Rates using the Two-parametric Approach

A brief summary of the two parameter approach is given here for the sake of clarity. Fatigue intrinsically requires two load-parameters for unambiguous description. Goodman [215] used the stress amplitude and the mean stress, more than a hundred years ago to uniquely quantify fatigue. The Haigh-diagrams have been developed to characterize *S-N* fatigue using the $\Delta\sigma$ and $\sigma_{mean,}$ or *R*. Traditionally, FCG is represented by d*a*/d*N* vs ΔK for different *R* values. A unified approach was developed to show that crack growth data can be uniquely represented in terms of ΔK and $K_{\max}$. The *R*-dependence, then is an intrinsic material property. The crack growth threshold is not a single value but a curve in the ΔK and K_{max}

plane. In essence, the extrinsic plasticity-induced crack closure is not needed to account for the R-dependence of FCG. If crack closure is present, then it will be a third parameter that needs to be considered, but it is not a substitute for the intrinsic two-parametric requirement for fatigue [187, 224, 225]. Since the residual stresses are monotonic in nature, they naturally affect the K_{max} parameter, as shown in Fig.6.3. In addition, it may also be noted that changes in the load-displacement curves of cracked specimens do not necessarily reflect the crack closure as is normally assumed, but can also arise due to plasticity ahead of the crack tip [226].

The data reduction scheme for the FCG analysis using the ΔK and $K_{\max}$ parameters are schematically presented in the previous chapter, Fig. 5.4. Figure 5.4a shows the FCG data in terms of ΔK. Fig. 5.4b shows the extraction of the ΔK-R data for selected da/dN values, starting from thresholds. Using Fig. 5.4b, the ΔK-K_{max} plots can be constructed for selected da/dN values, as in Fig. 5.4c. For any da/dN value, the ΔK-$K_{\max}$ data for different R values follow an L-shaped curve, with the knee defining the two limiting values, namely, ΔK^* and $K_{\max}^*$. It has been shown in Chapter 5 that the L-shaped curve represents the material microstructure/ environment property independent of the type of fatigue crack growth tests (i.e., constant R, constant ΔK, constant $K_{\max}$, etc.).

In the present case, the residual stresses in the weld affect the L-shaped curves and thus the limiting ΔK^* and $K_{\max}^*$ values. The plot of the limiting values, ΔK^* and $K_{\max}^*$, Fig. 5.4d, provides the crack growth trajectory map as discussed in the previous chapter. It defines the changing crack growth resistance with the crack growth rate for a given material/environment. The history effects are embedded in it.

Thus, it represents the fatigue crack growth resistance curve as a function of crack growth rate. It deviates from the pure fatigue line (45^o-line) when there are superimposed K_{max}-dependent processes. It can be the contribution from superimposed residual stresses as in the present case, environmental contributions, any other process dependent on monotonic load, or their combinations. The tests in an inert environment help to eliminate the superimposed environmental effects. In the case of the base metal, it was shown that deformation induced martensite transformation (DIMT) contributed to the enhanced crack growth resistance resulting in a corresponding deviation in the fatigue crack growth trajectory curve from the pure fatigue line.

6.3.1 The application of L-shaped curves for Friction Stir Welds in Al-alloys

Before analyzing the present data of the SS316(N) weld, it is instructive to examine the comparative FCG behavior of other weld and base materials available in the literature, using the two-parametric approach. Figure 6.4, for example, shows the L-shaped curves obtained using the FCG data of base metal and the friction stir welds (FSW) of 2024 and 6013 Al-alloys [161] at different R values. A close examination of this figure indicates that for both welds, the $K_{max,th}$* is affected by the residual stresses while ΔK_{th}* is not influenced. The details for each alloy differ. In particular, for base metals of both alloys, the $K_{max,th}$* values are the same (~5 MPa.m$^{0.5}$), while their ΔK_{th}* thresholds are different (1.5 and 3.5 MPa.m$^{0.5}$, respectively). In both cases, $K_{max,th}$* values are higher than the ΔK_{th}* values. It is generally true for all materials. For both the welds, the $K_{max,th}$* values are ~10 MPa.m$^{0.5}$, double the values compared to those of the base metals, while their ΔK_{th}* values remain the same as those for the respective base metals. The results confirm that the residual stresses being monotonic in nature, mostly affect the $K_{max,th}$* and not ΔK_{th}*.

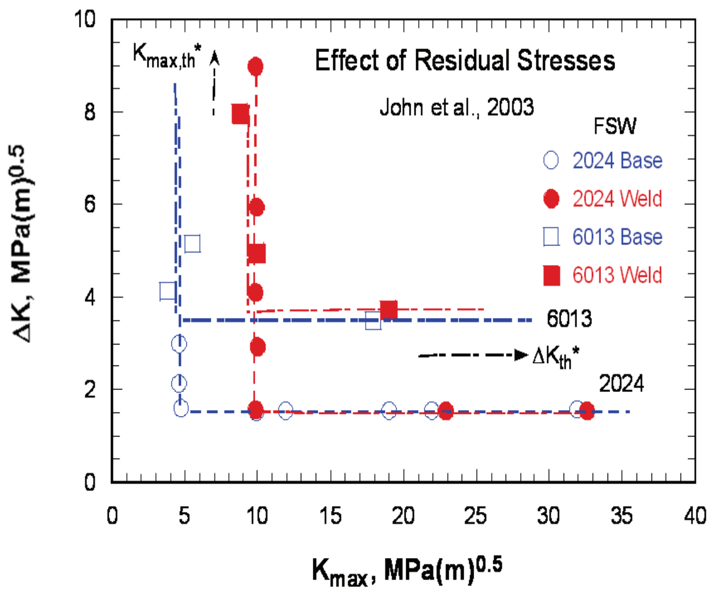

Figure 6.4 Effect of residual stresses on the ΔK-$K_{\max}$ threshold curve in 2024 and 6013 alloys from 'John et al. 2003 [161]

6.3.2 Two-parametric representation of the FCG in the SS316 (N) weld metal

As noted, before, the SS 316(N) weld in the present study has a higher carbon content. This is to ensure better creep resistance of the weld metal. The observed higher hardness in the weld metal (Section # 6.2.1) could also arise from compositional and microstructural differences, in addition to the residual stresses. These can also contribute to the increased resistance to FCG. Further analysis of the present data is done using the two-parametric approach. Figure 6.5a & 6.5c shows the ΔK-R plots extracted from Figs. 6.2a and 6.2b for the selected da/dN values. Interpolation was used to extract additional data for the intermediate R-values. The ΔK - K_{max} values thus determined are plotted in Fig. 6.5b for the selected crack growth rates. It includes both the original and the interpolated data. The plot shows the L-shaped behavior defining two limiting values, ΔK^* and K_{max}^* for each crack growth rate. In contrast to Fig. 6.4, the vertical line of L-curve in Fig. 6.5b bends, with some curvature towards the K_{max}-axis. Such behavior has been observed occasionally in some materials [189, 192]. However, the K_{max}-line becomes slowly straight at higher crack growth rates. In any case, the general feature of the L-shaped curve requiring the two liming thresholds, $K_{max,th}^*$ and ΔK_{th}^* for fatigue crack growth is maintained. While both thresholds should be met simultaneously, $K_{max,th}^*$ is the controlling parameter at low R, while at high R, ΔK_{th}^* is the controlling parameter. In the case of weld materials, the applied K_{max} has to overcome superimposed residual stresses to cause crack growth. Each of the L-shaped curves in the ΔK-K_{max} plot is associated with a crack growth mechanism. In some cases, more than one mechanism of crack growth may be involved. The transition from one mechanism to the other can occur with a change in R or change in crack growth rate. That gets reflected in the L-shaped curves. For example, Figs 6.5c and 6.5d show the beginning of the second L-shaped curves at low K_{max} values and high crack growth rates. This can be seen by the formation of the second plateau region. The crack growth trajectory map can be plotted using these limiting ΔK^*-K_{max}^* values, and results are shown in Fig. 6.6a. The trajectory map shows some bends in the curve. One can always draw a straight line considering any deviations as part of the spread in the data. At higher crack growth rates, the crack growth trajectory tends to merge with the pure fatigue line, indicating that there are no superimposed K_{max} effects any more.

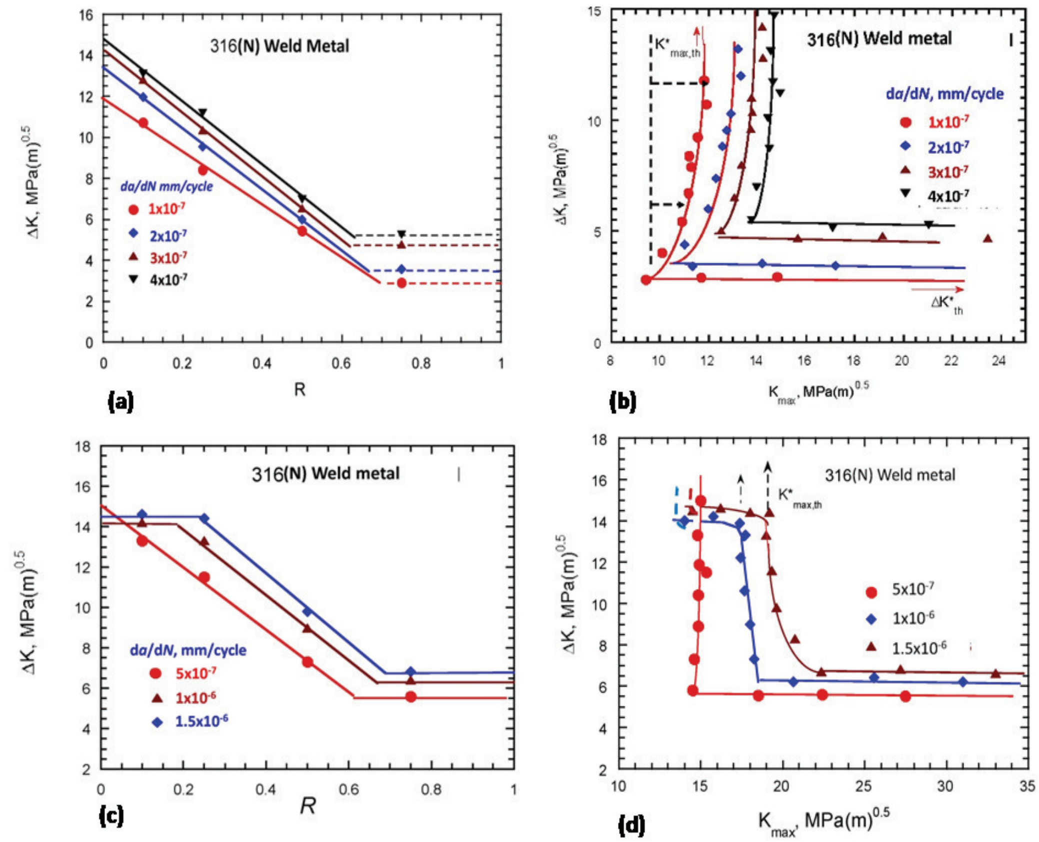

Figure 6.5 ΔK-R curves at low (a) and high (c) crack growth rate with the corresponding ΔK - K_{max} curves (b) and (d) respectively

The trajectory maps of the base metal from the previous chapter and weld metals from current chapter are compared in Fig. 6.6b. It was shown in the previous chapter that the deviation of the trajectory map from the 45^{o}-line for the base metal was due to the transformation toughening that occurs in many 300 series of austenitic stainless steels. While the presence of nitrogen inhibits this transformation toughening to some extent by stabilizing the austenite, it was found that some transformation still occurred in the 316 stainless steel containing 8N and 14N causing a shift in the crack growth trajectory. In the case of the weld metal, there can be two contributions, one from the residual stresses and the other from the transformation toughening. The applied K_{max} is therefore equal to

$$K_{max,ap} = K_{max,crack} + K_{max,res} + K_{max,tr}$$

where $K_{max,crack}$ is the intrinsic material resistance, $K_{max,res}$ is the component needed to overcome the contribution from the compressive residual stress and $K_{max,tr}$ is that needed to overcome transformation toughening. Linear summation of the components is possible within the linear elasticity approximation. The ΔK_{res} for each crack growth rate is extracted for different crack growth rates using Fig. 6.3c as the difference in the ΔK values in the weld metal in relation to that in the base metal. Figure 6.6c shows the variation in the ΔK_{res} as a function of crack growth rate. It indicates that the residual stress contribution changes with R. At R=0.1, the residual stress contribution is very high near threshold but decreases with increasing crack growth rate. At high R (R=0.75), the contribution is small even at the threshold and (Fig. 6.6c shows that it increases and saturates at high crack growth rates, ~5E^{-7} mm/cycle) remains constant with increase in crack growth rate.

From the Fig 6.6c, it clear that the difference in ΔK for R=0.1 is ~8MPa(m)$^{0.5}$ near to the threshold value. The residual stresses were measured on the CT sample near to the crack length of 35 mm from load line by hole drilling method as presented in the experimental, chapter 3. The residual stresses near that crack length (thresholds regime) is found to be -25 MPa, which is corresponding to the ΔK= -8MPa(m)$^{0.5}$. This confirms that the shift in the crack growth trajectory is due to the compressive residual stresses in addition to the transformation toughening. Moreover, it is possible that the residual stresses just ahead of the notch were relieved by the notch preparation. Therefore, initial data points are not affected. However, the FCG test in the near threshold regime started at a low ΔK level (~10 MPa(m)$^{0.5}$) and the residual stresses ahead of the crack influence the $K_{max,th}$. With further crack growth and continuous cycling again the residual stresses relaxed to same extent, bringing down the difference.

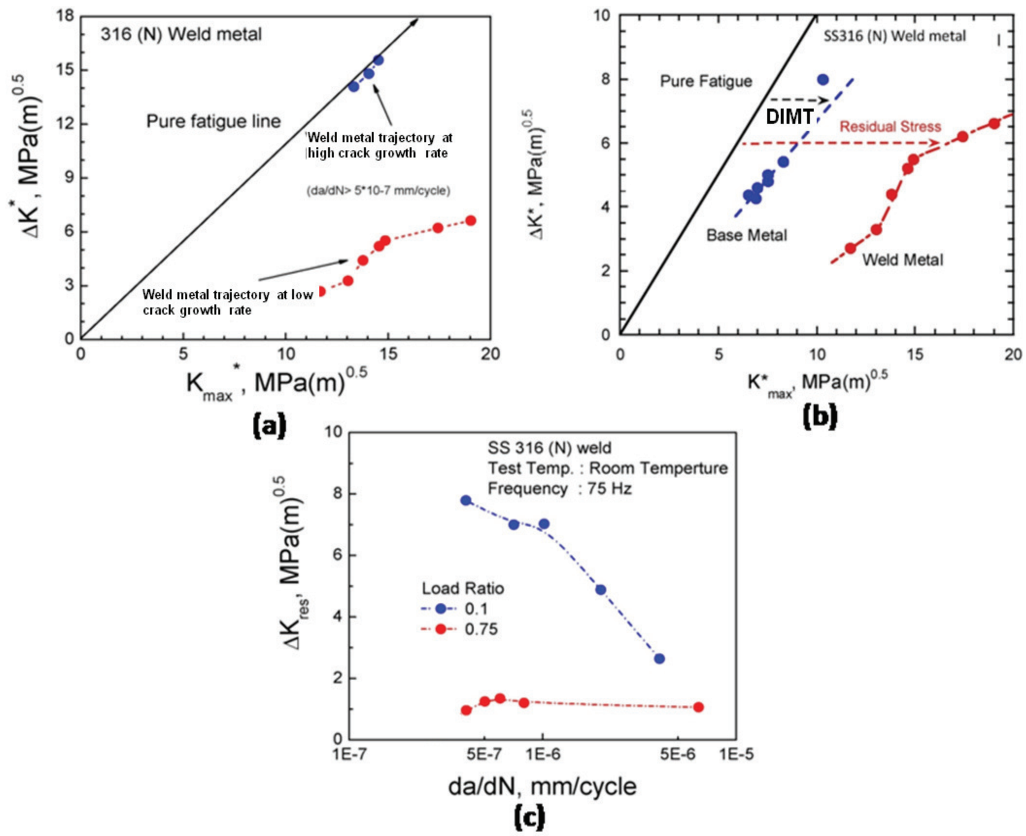

Figure 6.6 (a) Crack growth trajectory (ΔK^*-K_{max}^*) at low and high da/dN values (b) comparison of trajectories of base and weld metals, (c) ΔK_{res} in the weld metal as a function of crack growth rate

6.4 Two-parametric representation of the FCG in other weld materials

In order to identify the role of residual stresses using the two parametric approach, it is required to examine the FCG behavior of welds with different levels of residual stresses, which are also experimentally verified. This would require a detailed study with weld specimens fabricated from different weld pads prepared using different plate dimensions and/or using various welding procedures. The scope of such a study in itself is vast, and can form another thesis. Here, FCG data available in open literature on various welds with different levels of residual stresses are examined. Some of these studies quantify residual stresses by measurement, and others report qualitative assessment by relative magnitudes. In the following sections, the crack growth behavior of other weld materials reported in the literature is analyzed.

6.4.1 Low carbon steels

DeMarte [227] has reported the FCG behaviour of low carbon steels and their welds. Figures 6.7a and 6.7b show the results of DeMarte. The base metal was low carbon steel designated as A36. Two weld metals, A5.18 and A5.28, were used. The hardness data for the welds and the base metal are shown in Fig. 6.7a. In both the welds, the hardness peaks up in the weld strip in comparison to the background hardness of the base metal. Figure 6.7a also shows that the hardness of A5.28 is higher than A5.18 weld. The weld specimens were tested after stress-relief heat treatment. The microstructures of base metal A36 and the two welds are nearly the same, and correspond to those of any typical low carbon steels, with acicular ferrite and some pearlite, and with a fine distribution of some carbides. However, the grain size of A5.28 is smaller than that of base metal and A5.18 weld. This results in higher yield stresses and hardness values. Also, the weld metal A5.28 has higher Ni and Mo content compared to A5.18. Figure 6.7b shows the FCG rates for the base and the welds as reported by DeMarte. While both the welds have higher crack growth resistance than the base metal, Fig. 6.7b also shows that the resistance is higher for A5.18 than A5.28 in spite of the finer grain size, higher alloy content and the higher hardness of the latter. Finer grain size enhances the strength without compromising the ductility. However, their may be other microstrctiral factors that lead to higher hardness of A5.28 weld The results indicate that in addition to any residual stresses, the microstructures play an important role in deciding the crack growth rates. The crack growth trajectory maps could not be constructed since data for only one R-value are available.

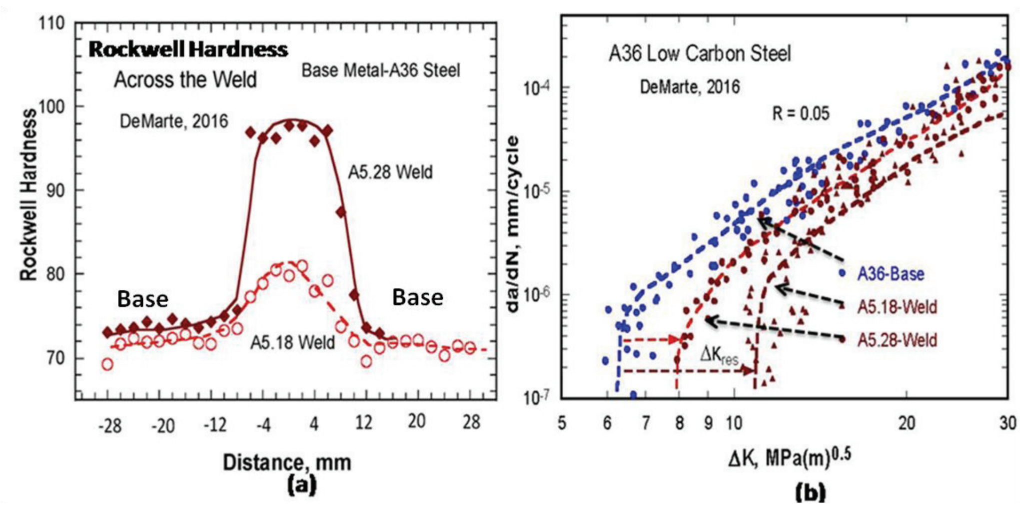

Figure 6.7 (a) Hardness of weld strip in comparison to base metal of A36 (b) crack growth rate at low R (=0.05) in the base steel (A36) and two weld materials A5.18 and A5.28 [227]

6.4.2 Aluminum alloys

6.4.2.1 5083 H32 Alloy

Figure 6.8a shows the FCG rates for the base and FSW weld metals of 5083 H32 Al-alloy as reported by John et al [161] at two R values, viz., 0.1 and 0.8. If the shift in the crack growth rates in the weld material is due to residual stresses, then Fig. 6.8a shows that the effect is more pronounced at low R values than at high R values, as discussed with reference to Fig. 6.8. In addition, it was also noted (Fig. 6.5) that the low R data generally fall on the vertical line of the L-shaped curve defining the K_{max}* value and the high R data fall on the horizontal line of the L-shaped curve defining ΔK*. The available data, even though limited to only two R values, have been used as the limiting values to plot the crack growth trajectory in both the base and weld metals, and this is shown in Fig. 6.9b. There is a significant shift in the crack growth trajectory of the weld metal in comparison with that of the base metal. The vectors connecting the points corresponding to the same crack growth rates for base and weld metals (for example, AA′ in Fig. 6.8b) measure the relative shifts of K_{max}* and ΔK^* components. The vector AA′ can be split into parallel (BA′) and perpendicular (AB) components to the pure fatigue line (the 45°-line). The vector BA′ designates the change in the ΔK*-component, and the vector AB designates the shift in the K_{max}*-component. The vectorial components seem to indicate that there is some effect on the ΔK component as well, and could be due to change in the microstructure than the residual stresses *per se*.

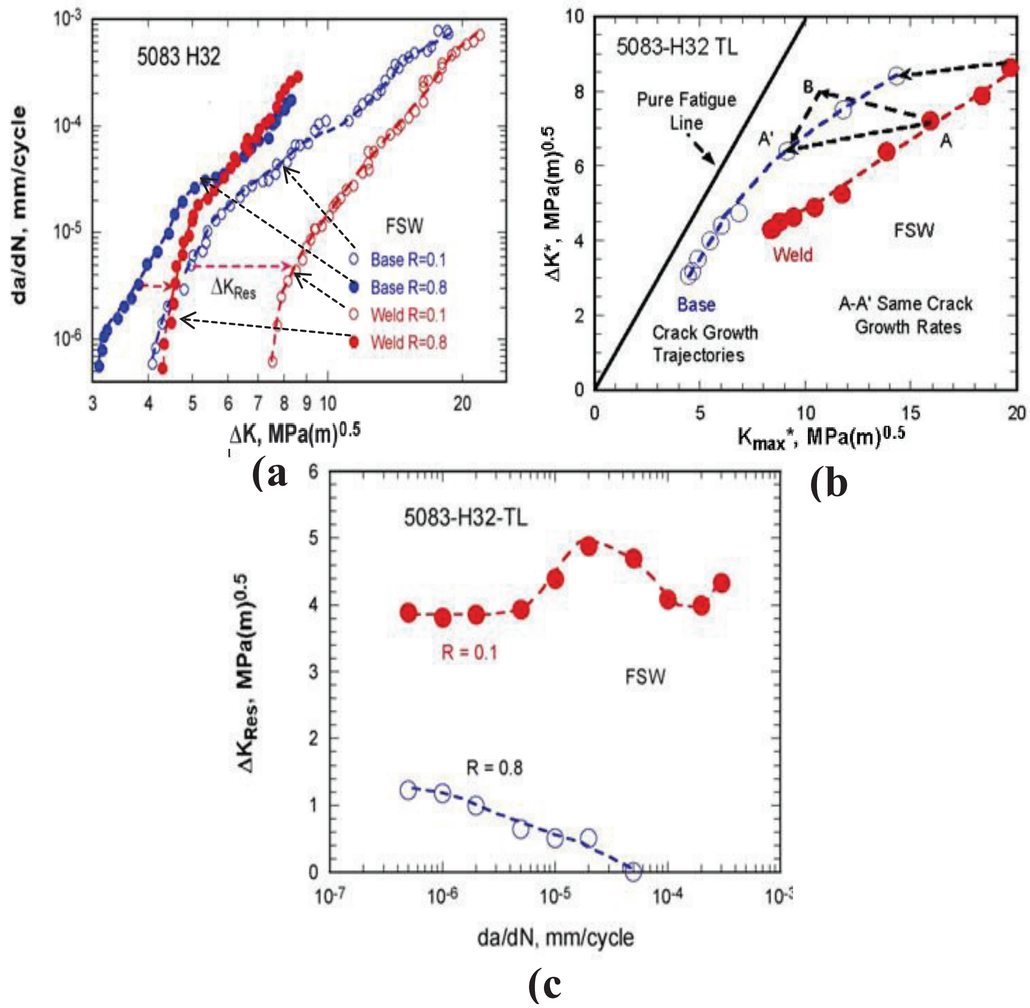

Figure 6.8 (a) FCG behaviour of 5083 H32 Al alloy at low and high R-values of base and FSW weld metals (b) Crack growth trajectories(c) ΔK_{res} contribution to the crack growth resistance [161]

Thus, the trajectory maps provide the crack growth behaviours of the welds in comparison with those of the base metals as cracks grow from the threshold to fast fracture. If the crack growth mechanisms change during crack growth, their effects will also be reflected in the trajectory map. The trajectory map also reflects the history effects since fatigue damage during prior cycles affects the current crack growth rates. Figure 6.8c shows the ΔK_{res} as a function of crack growth rate extracted from Fig. 6.8a. It is measured as the difference in the applied crack tip driving forces (Fig. 6.8a), that enforces the same crack growth rate in the base and weld metals. Figure 6.8c shows that the ΔK_{res} is small at high R and goes to zero with the increase in crack growth rate. At low R, it fluctuates about 4 MPa.m$^{0.5}$ as the crack grows from threshold to Paris regime, to overload fracture.

6.4.2.2 6061-T651 Alloy

The FCG rates in the base and weld metals of the 6061-T651 alloy from the literature [161, 228] are shown in Fig. 6.9a at R = 0.1 and 0.8. The difference between the base and weld metals is higher at R= 0.1 than at R= 0.8, though the difference is not clearly revealed by the log-log plots. However, in comparison with Fig. 6.9a, the behavior of this alloy appears to be different. In fact, if one examines the crack growth trajectory maps of the base and weld metals plotted in Fig. 6.9b, they appear to be the same within the experimental scatter. It may also be an indication that residual stresses are low for these welds and the shift of the trajectory map from the pure fatigue line is related more to the intrinsic material resistance due to microstructure or chemical composition.

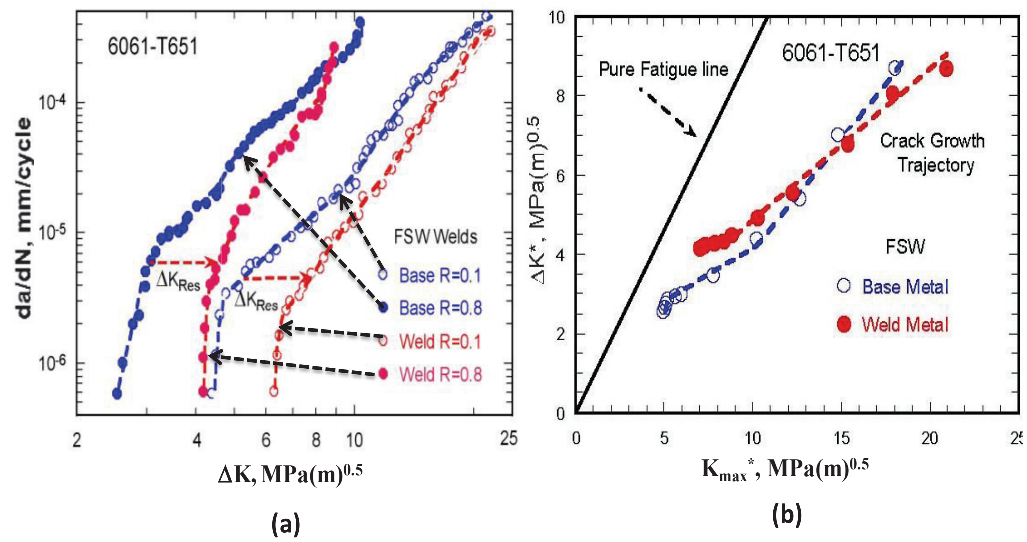

Figure 6.9 (a) Crack growth results of 6061-T651 Al alloy base and FSW metal at *R*-values of 0.1 and 0.8, (b) Crack growth trajectory

6.4.2.3 Al-Li Alloy 2195-T8

Figure 6.10a shows the crack growth rates in the base and weld metals of 2195-T8 Al-Li alloys by Ma et al.[229]. The authors have made FSW welds using different sizes of the specimen blanks keeping the thickness of the plate constant (8 mm). The figure shows that the crack growth rates vary with the size of the welds. This may be attributed to the variation in residual stresses with the size of the welds. It is also an indication that one has to study each weld separately since the residual stresses can vary from weld to weld. The ΔK_{res} as a function of crack growth rate also varies with the size of the welds as shown in Fig. 6.10b. While welding introduces residual stresses which influence the crack growth rate, the stresses depend on the welding process, the thickness of the weld, and any post-welding treatments. These, in turn, influence the ΔK_{th} and $K_{max,th}$. Therefore, to determine the ΔK_{th} and $K_{max,th}$ for meaningful safe life design, the FCG tests should be performed as a function of *R* are on both base and weld metals for structural applications.

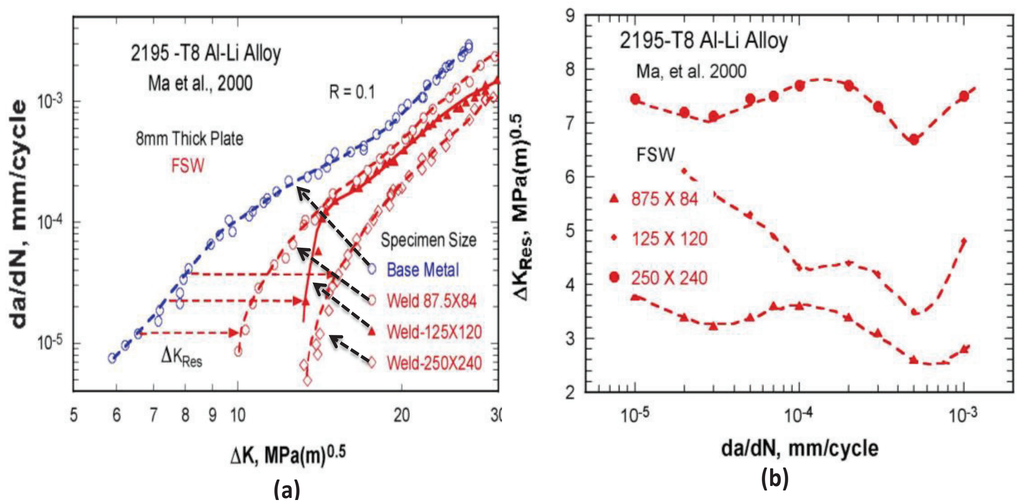

Figure 6.10 (a) FCG results at R= 0.1 for base and 8 mm thick FSW weld of Al-Li alloy with different weld sizes, (b) the variation of ΔK_{res} with crack growth rate and weld size [226]

6.4.3 25Cr2Ni2MoV steel

The work of Du et al., [230, 231] on FCG behaviour of 25Cr2Ni2MoV base and weld metals are discussed next. In addition to the effect of welding, they have also considered the effect of heat treatment on the crack growth rates. Following the procedure outlined above, the crack growth rate data of both the base and the weld materials are analyzed. The results are shown in Figs. 6.11-6.13. Figs. 6.11 a, b, and c present the analysis of the crack growth behavior of the base metal while Figs. 6.12a, b, and c present that of the weld metal. The crack growth trajectories of the two are shown in Fig. 6.13. The crack growth in the weld material shifts more towards the K_{max}-axis due to the presence of the residual stresses. The base metal also shows considerable shift from the 45^{o} line indicating that there are additional K_{max}-dependent processes occurring during fatigue. It could be an environmental contribution or any other K_{max}-dependent process arising due to microstructure or a combination of the two. This steel has high Cr content, in addition to Ni, Mo and V, which can form carbides that can affect the crack growth resistance. The analysis, however, shows that residual stresses arising from welding can contribute to the additional shift in trajectory map towards the K_{max}-axis. These results are thus consistent with the findings of the present study.

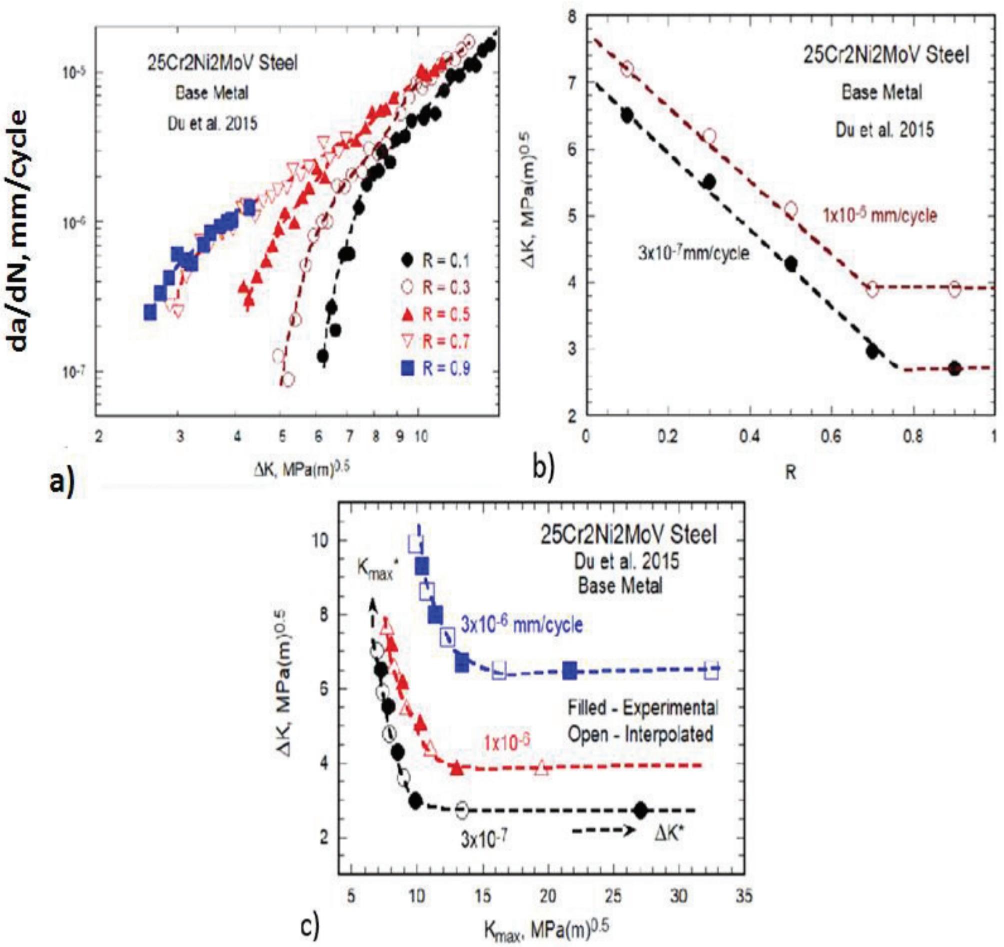

Figure 6.11 (a) Crack growth rate (b) ΔK-R, (c) ΔK-K_{max} of 25Cr2Ni2MoV steel base metal

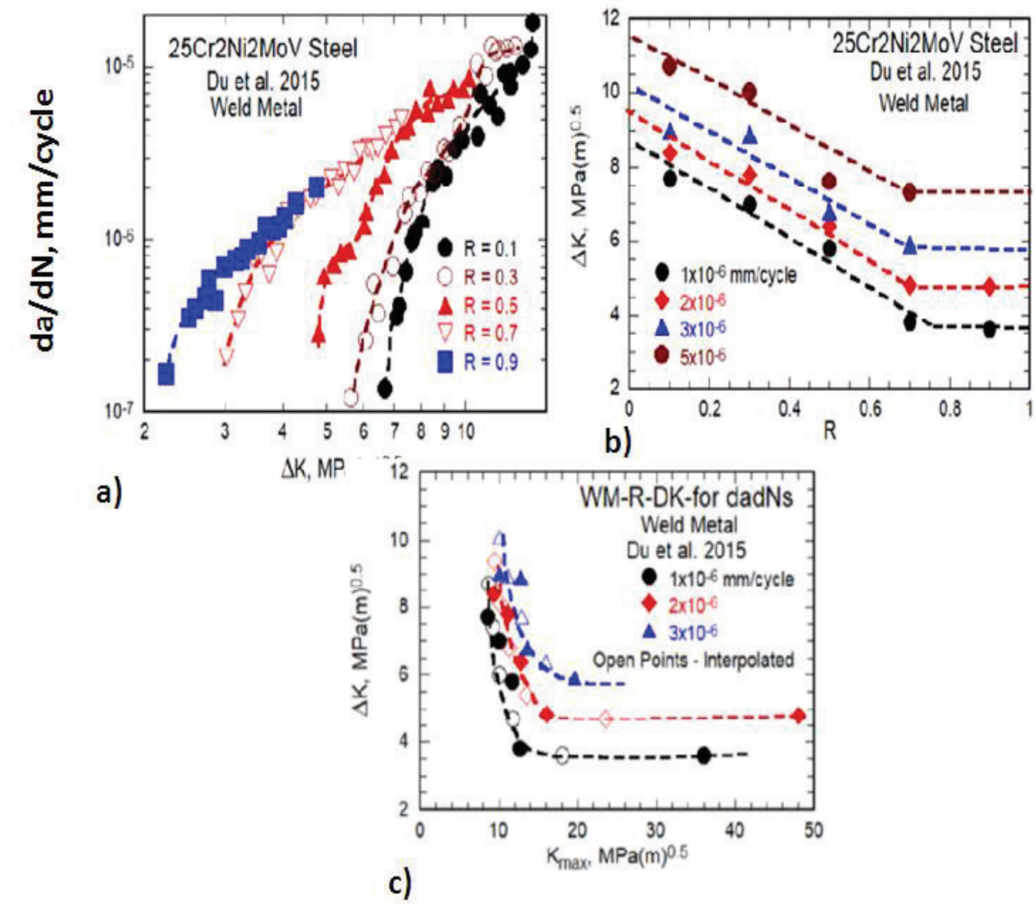

Figure 6.12 (a) Crack growth rate (b) ΔK-R, (c) ΔK-K_{max} of 25Cr2Ni2MoV steel weld metal [225, 231]

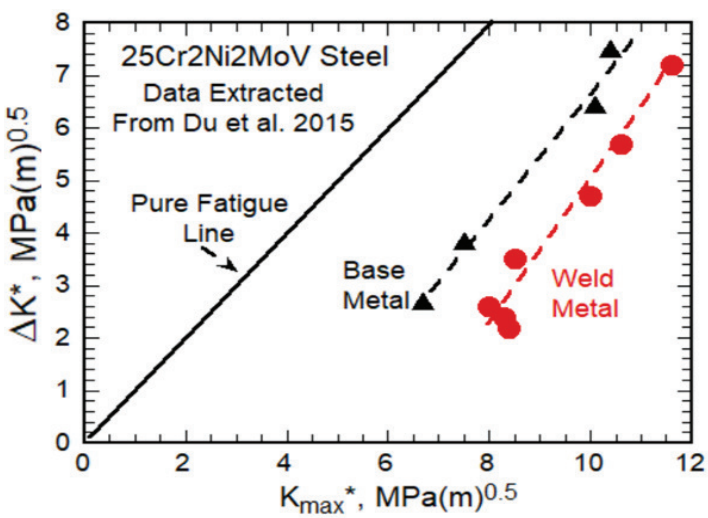

Figure 6.13 Crack growth trajectories of 25Cr2Ni2MoV steel extracted from Figs.6.12 and 6.13

6.5 Effect of cold work on the fatigue crack growth behaviour of SS316LN steel

In addition to welding, manufacturing of the components involves different metal forming operations, e.g., rolling of plates, bending of pipings, extrusion etc which introduce different extents of cold work in the material. As per the standard [90,91] design codes, in the case of pipings, the maximum cold work permitted by bending operation is 20%. Like welding, these operations also introduce residual stresses in the material. If the cold work level is 10% or less, no stress relieving heat treatment is recommended in the codes [90]. Hence, FCG studies were carried out at ambient temperature at various R values on the SS316L(N) (14N) cold worked to different extents (5, 10 and 15 %). The results are presented in Fig 6.14 a-c for 5, 10 and 15 % cold work condition respectively.

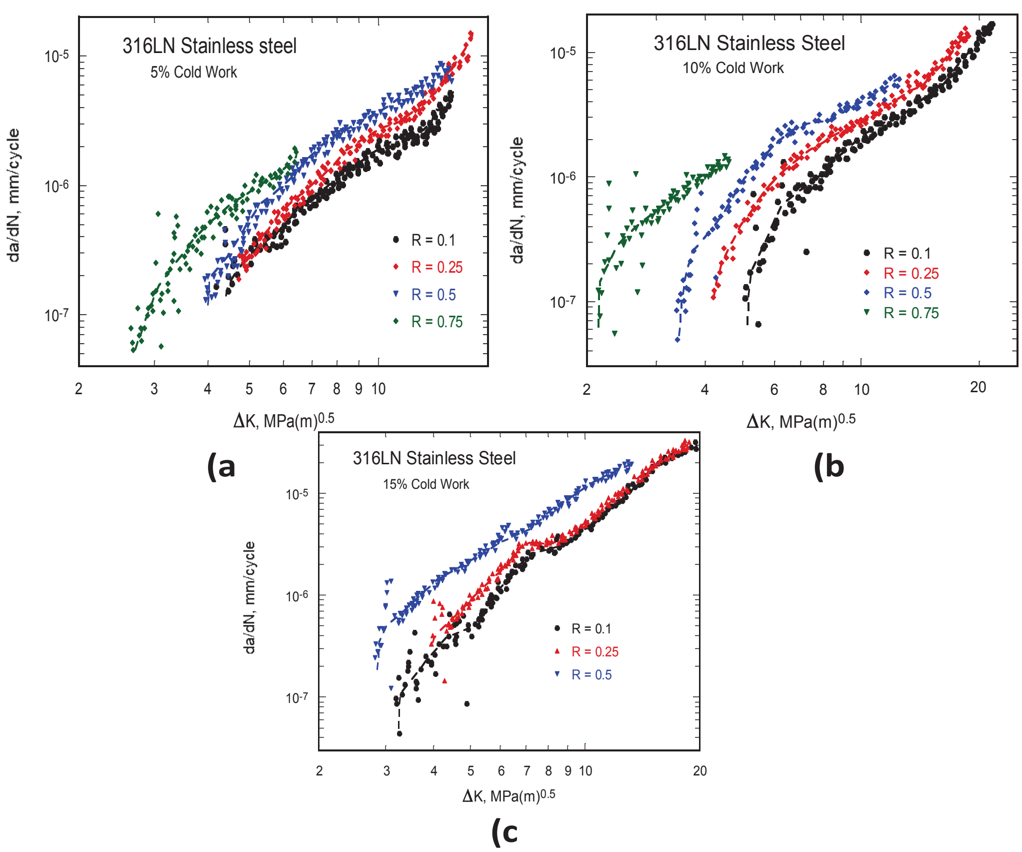

Figure 6.14 FCG results at room temperature for SS316L(N) (14N)(a) 5% (b) 10% and (c) 15% cold worked material at different load ratios

The unified approach is adopted for analyzing these results as in the case of solution annealed base metal (Chapter 5) and weld material in the previous sections in the present chapter. Initailly, the intermediate ΔK-R plots were obtained at different crack growth levels. From these plots, the additional L-shape curves are presented for 5%, 10% and 15 % cold worked materials in Fig 6.15 (a) through (c). Close examination of the L-shape curve for 5% cold work (Fig 6.15(a)) shows two L-shape curve at low crack growth rate indicating the onset of a different crack growth mechanism. This kind of behaviour may be attributed to the extent of tranformation toughening is different with crack growth rate. However, with increasing the crack growth rate it is vanishing. The crack growth trajectories have been constructed and presented in Fig 6.16 in comparison with that for the solution annealed material as procedure mentioned in the chapter 5.

It is clearly seen that the crack growth resistance of cold worked material is marginally better than the solution annealed condition. This can be attributed to (i) presence of deformation induced martensite due to the cold work and due to in situ deformation during FCG (ii) residual compressive stresses due to cold work. These FCG results reveal that the data for the solution annealed and 5% cold worked material are in the same scatter band. On the other hand, the data for 10 and 15% CW materials share a scatter band which lies to the right, though the data for 15%CW seems to be slightly further towards right, especially at high crack growth rates. However, at very high crack growth rates, there is a tendency for all the three to merge with the data for solution annealed material indicating a saturation of DIMT effect

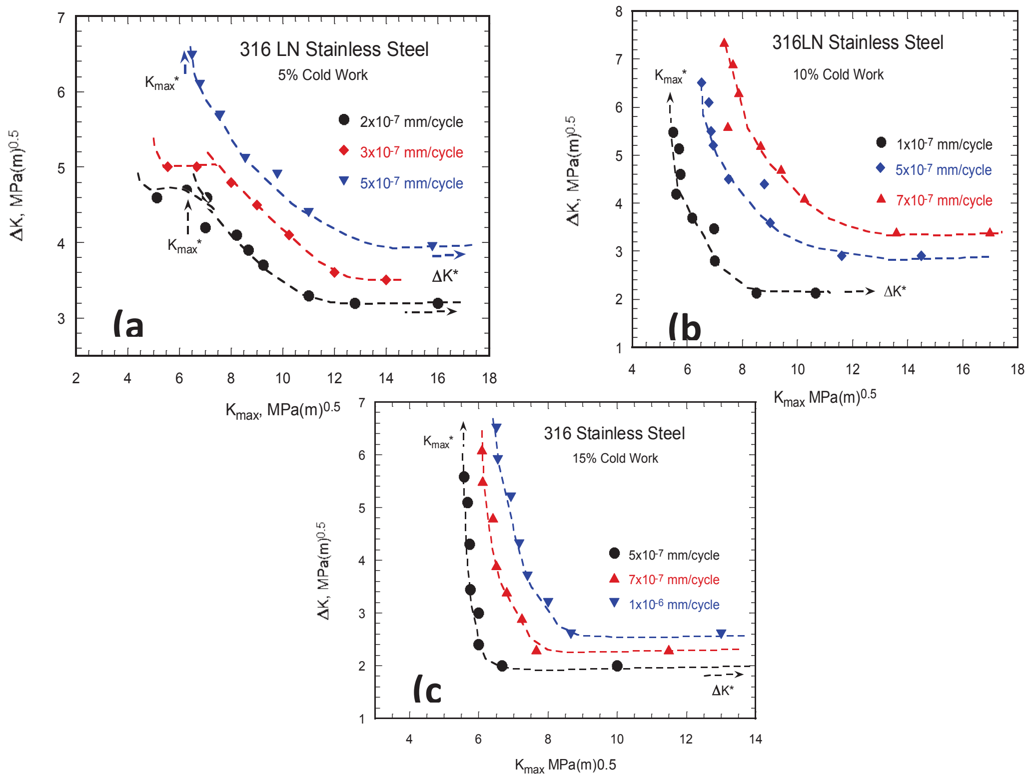

Figure 6.15 L-Shape curved SS316L(N) (14N) for (a) 5% (b) 10% and (c) 15% cold worked material at room temperature.

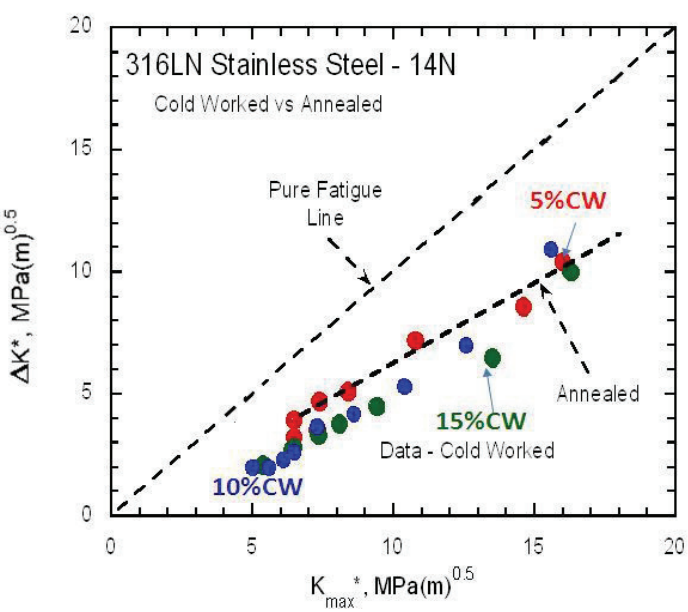

Figure 6.16 Crack growth trajectories of SS316LN (14N) for different cold worked conditions

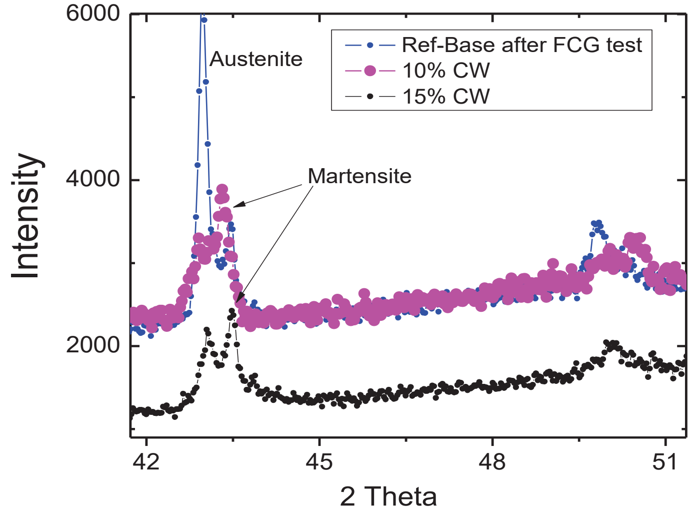

Figure 6.17 XRD results reveal the presence of deformation inducedmartensite

Presence of martensite is further confirmed with XRD-analysis presented in Fig 6.17. The martensite peak is stronger in the cold worked material, confirming that there is an additional contribution to DIMT from cold work. However, the presence or nature of residual stresses was not experimentally confirmed. Considering the presence of strong martensite peaks in the cold worked material, the difference between the trajectories for solution annealed and cold worked materials, may appear to be insignificant. It is also possible that the cold work introduces tensile residual stresses along the loading direction of the CT specimen, i.e., perpendicular to the rolling direction of the plate. The effect of these tensile residual stresses would be to offset the beneficial effects of DIMT to some extent. A quantitative study of the residual stresses in the cold worked material would prove to be useful to identify the magnitude of the beneficial effects of DIMT.

6.6 Conclusions

FCG behavior of SS316(N) weld metal has been evaluated at different load ratios at room temperature and is analyzed using the Unified Approach that takes the two-parametric nature of fatigue in to account. The results are compared with those of the 8N base metal. It is found that the FCG thresholds are much higher than those of the base metal and the FCG rates are lower, particularly at low R values. This enhanced resistance to crack growth arises from a) presence of residual compressive stresses, b) stress-induced martensitic transformation of austenite phase present near the crack tip region, and c) the higher alloy content and the presence of δ-ferrite. Crack growth trajectory map was developed that depicts the relative variation of the limiting values, ΔK^* and K_{max}^*, as a function of crack growth rate. It is compared with the previously determined trajectory map of the base metal. The crack growth trajectories of both the base and the weld metals deviated towards the K_{max}-axis from the pure-fatigue line. In the case of the base metal, the deviation was related to the stress-induced martensitic transformation of the retained austenite ahead of the crack tip. The trajectory map of the weld metal deviated more than that of the base metal. The larger deviation is attributed to the residual compressive stresses introduced during welding in addition to the presence of any transformation toughening. In this context, published crack growth data for other weld and base metals available in the literature are also analyzed using the Unified Approach, and are discussed along with the trends observed in the present study. It is shown that the results from the present study are consistent with those published in the literature. The results also indicate that the residual stresses can vary with the welding process, thickness of the weld, and the subsequent post-welding stress relief operations. In most of the cases, the weld behaves as good as or better than the base metal. Similar analysis of the FCG data for the cold worked material of 14N shows that the K_{max}-dependent phenomenon is only marginally enhanced in the cold worked material compared to the solution annealed material, in spite of the increase in the extent of DIMT. Further studies are required to estimate the residual stresses in cold worked material to ascertain if the beneficial effects of DIMT are partially offset by the presence of tensile residual stresses.

CHAPTER 7

MODIFIED KITAGAWA-TAKAHASHI DIAGRAM FOR SHORT CRACK GROWTH AND ENVIRONMENTAL EFFECTS

CHAPTER 7 : MODIFIED KITAGAWA-TAKAHASHI DIAGRAM FOR SHORT CRACK GROWTH AND ENVIRONMENTAL EFFECTS

7.0 Introduction

In this chapter, the modified Kitagawa-Takahashi (KT) diagram that takes in to account the two-load parameter requirement of fatigue, is used to describe the short crack behaviour and environmental effects in FCG of SS 316L(N). The FCG data of SS304 and SS316 in air and vacuum for long cracks available in the literature are examined to understand the influence of environment. Also, the FCG behaviours of SS 316LN (8N) steel with short and long cracks are examined using the data generated within the vacuum chamber of a scanning electron microscope (SEM) equipped with a mechanical stage. The *in-situ* observations during the crack growth are discussed. The differences in long and short crack growth behaviour are analysed using the modified KT diagram using the principles derived from the Unified Approach. The effect of environment is also discussed in the context of modified KT diagram.

7.1 Background

7.1.1 The Kitagawa-Takahashi Diagram

The Kitagawa-Takahashi (K-T) diagram (Fig.7.1) is a double logarithmic plot of the applied stress and crack length that connects the limiting S-N behaviour of a smooth specimen to the threshold behaviour of crack growth in a fracture mechanics specimen. The original KT diagram [232] uses the stress amplitude corresponding to the endurance limit ($\Delta\sigma_e$) for smooth specimen and ΔK_{th} for growth of existing long crack. For cracks of a given length experiencing a given stress range, it defines the area of non-propagating cracks and thus allows to predict the allowable stress range to ensure infinite life. It is used widely for fracture mechanics based design of components and safe-life or fail-safe concepts for fracture control. It is quite useful for design since it combines the endurance based and damage tolerant regimes into a single diagram.

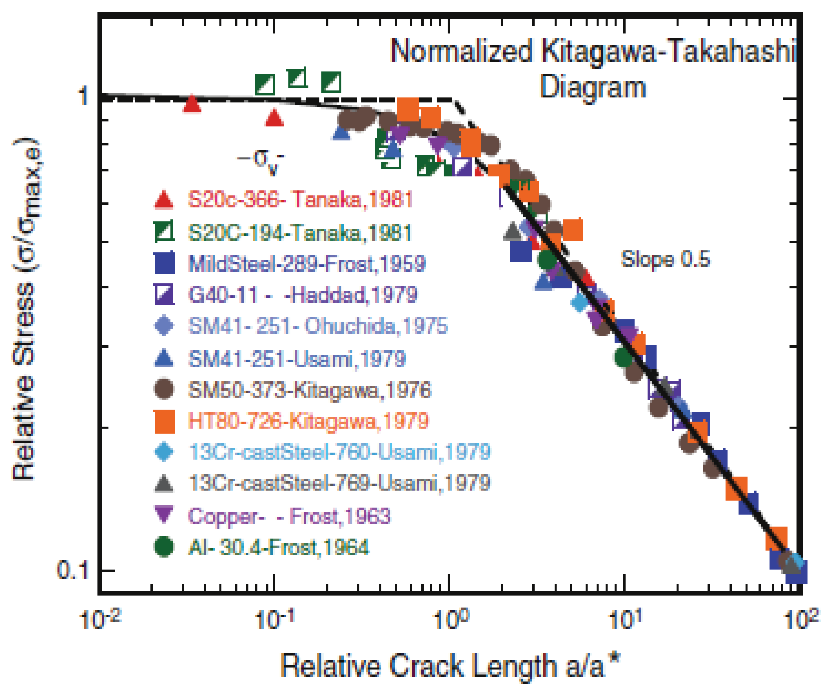

Figure 7.1 Kitagawa-Takahashi diagram [232] for different materials as presented in [234]

7.1.2 Short crack behaviour

The LEFM frame work assumes ΔK as the crack driving force and as discussed in the previous chapters, K_{max} too plays an important role. These two parameters alone cannot describe the anomaly in the short crack growth behaviour.

It is known that the fracture stress is expressed as inverse functions of the crack length as follows.

$$\sigma_f = \left(\frac{E\gamma}{a}\right)^{1/2} --- (1) \text{ or } \sigma_f = \left(\frac{E\gamma_{(e+p)}}{a}\right)^{1/2} --- (2)$$

where σ_f: fracture stress, E : Young's modulus, γ : Surface energy (elastic or plastic) and a : crack length. Therefore, the stress required for crack growth is inversely proportional to the square root of crack length, either on the basis of Griffith's equation or Orowan's equation [22, 23]. Hence the shorter the crack, the higher is the stress needed for its growth. However, literature data indicate that short cracks grow at applied ΔK levels lower than that required for long cracks [168]. After that several studies are available in literature on short crack growth [170-178, 180-184, 233] and in these studies short cracks are treated as different from long crack. Hence, similitude break down was proposed for short cracks [44, 49, 73, 168, 177]. However, crack initiation in specimens with no cracks (smooth specimens), experiencing globally elastic loading requires a large number of fatigue cycles (~10 million cycles or more), particularly near the endurance limit. Extensive fatigue damage analysis in the literature indicates that these large numbers of cycles contribute to the formation of intrusions and extrusions, persistent slip bands, dislocation pile-ups, and deformation bands. They cause the build-up of local internal stresses with steep gradients. Incipient cracking takes place under the influence of these internal stresses, and the remote applied stresses augment this. Fracture mechanics does not take these internal stresses explicitly into consideration in computing actual crack tip driving forces.

These internal stresses are difficult to determine experimentally. Nevertheless, they must exist and contribute to the crack tip driving forces. The behavior is somewhat similar to the crack initiation at sharp notches with stress gradients, which can be analyzed using elastic-plastic fracture mechanics methods. The Unified Approach recognizes this aspect and a modified Kitagawa diagram that connects the short crack growth behavior with that of long crack was developed by considering these internal stresses [234]. The requirement of the load parameter K_{max} in addition to ΔK for FCG as discussed in earlier chapters provides the framework for this. The modified Kitagawa diagram provides a simple methodology to compute the minimum internal stresses needed in addition to the applied stresses for the short cracks to grow. The approach is based on the assertion that a) the long crack growth thresholds are fundamental for a given material/environment system, and b) they are independent of crack length. Even the short cracks should meet the same criteria for growth, and there is no similitude breakdown when one considers the total crack tip driving force that includes applied and internal stresses.

Some studies attribute the short crack behaviour to environmental effects. Further, it is reported that the ΔK_{th} is lower in air or any damaging environment compared to that in vacuum [110]. This necessitates determining the ΔK_{th} in the actual environment for predicting the allowable stresses for infinite life. However, the environment is an extraneous factor that contributes to crack growth by providing an additional chemical driving force at the crack tip, and its effect should be to reduce the applied K_{max} required for the crack to grow, rather than the ΔK since the chemical forces at the crack tip due to environment are not cyclic in nature. The interpretation of lower ΔK_{th} in environment is a result of not considering the second load parameter of FCG, $K_{max,th}$.

The behaviour of short cracks in the nitrogen-bearing stainless steels are analyzed by constructing the modified Kitagawa-Takahashi diagram and computing the internal stresses involved assuming the validity of similitude. Also, the effect of environment on FCG is examined in the long crack regime, adopting the framework of modified Kitagawa-Takahashi diagram.

7.2 Growth behaviour of long fatigue cracks in air and vacuum

Before going into the short crack growth analysis, the long crack growth data of austenitic stainless steels (SS304 and SS316) in vacuum collected from the literature are examined in order to have some preliminary understanding of the environmental contribution to the crack growth resistance. Further, the crack growth resistances of SS316LN in vacuum and air environments are compared.

Figure 7.2 shows the FCG behavior of SS304 in air and vacuum, as reported in the literature [235]. There is a large difference in the ΔK values to cause the same crack growth rates in air and vacuum. This difference decreases with the increase in crack growth rates. It indicates that ambient air environment provides an additional crack tip driving force thereby decreasing the needed applied stress to cause crack growth. The difference between the ΔK values between vacuum and air for a given crack growth is, therefore, a measure of the mechanical equivalent of the chemical driving force that contributes to the crack growth. In addition, the larger ΔK values in vacuum could have a secondary contribution from enhanced crack growth resistance due to the higher levels of transformation toughening resulting from the deformation-induced martensite transformation (DIMT) discussed in chapter 5. The presumption here is that DIMT contribution is larger in vacuum than in air since the crack tip strains and plastic zone size are larger in vacuum than that in air due to larger ΔK value. The yield stresses are generally unaffected by the environment.

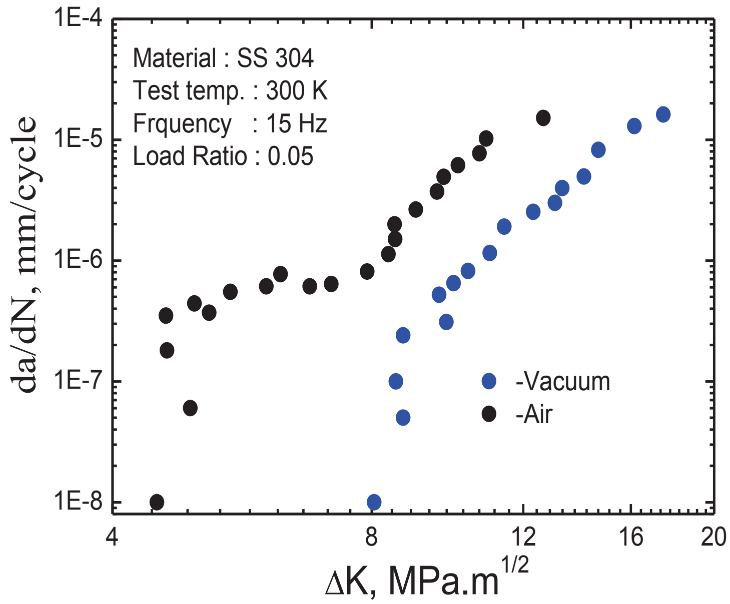

Figure 7.2 FCG results of SS304 in vacuum and air

The difference in ΔK values for vacuum and air environment (ΔK_{vac}–ΔK_{env}) as a function of crack growth rate is presented in Fig.7.3. As mentioned earlier, it represents the mechanical equivalent of the chemical crack tip driving force due to the environment aiding the crack growth. Figure 7.3 shows that the difference in the crack-tip driving force (ΔK_{vac}–ΔK_{env}) remains almost constant with increase in the crack growth rate. The dip observed in Fig. 7.3 is a reflection of some steady-state crack growth regime that can be seen around da/dN=5x10^{-6} mm/cycle, in Fig. 7.2. This seems to indicate the presence of some stage II steady-state (ΔK-independent) crack growth process such as that normally occurs under stress-corrosion cracking. More aggressive environments or lower frequencies perhaps could magnify this regime.

Another possible explanation for this is as follows. In vacuum, the applied $\Delta K \geq 8$ MPa.m$^{1/2}$. It is likely that above this, in both vacuum and air there is a strong influence of toughening due to DIMT in this material. However, in vacuum, absence of chemical crack tip driving forces lead to attainment of threshold at this value. In air on the other hand, the environmental effects lead to substantial crack propagation below this value, and at the same time the beneficial effect of DIMT vanishes due to reduced ΔK leading to crack growth rates higher than the trend line for higher ΔK.

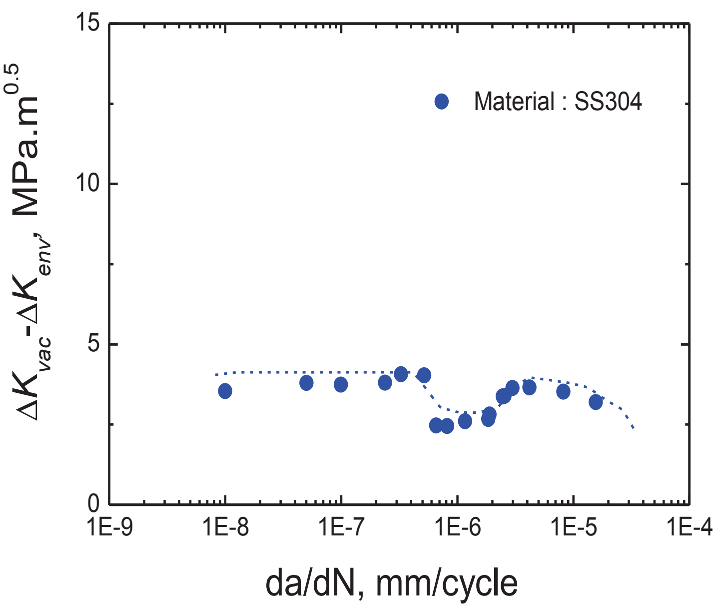

Figure 7.3 Environment contribution on FCG resistance of SS304. This includes any secondary contribution due to DIMT

Figure 7.4 shows the FCG results of SS316LN in comparison to SS316 in vacuum and air environments near room temperature 338 K [110]. The environmental contribution is more significant near the threshold regime, while at higher crack growth rates both the curves tend to merge indicating that the environmental contribution which is also time-dependent is more significant at low crack growth rates. Figure 7.5 shows the (ΔK_{vac}–ΔK_{env}) as a function of crack growth rate. The environmental contribution appears to reach a maximum in terms of crack growth rate. Since the contribution is also time-dependent, the reaction time at the crack tip decreases with increase in crack growth rates.

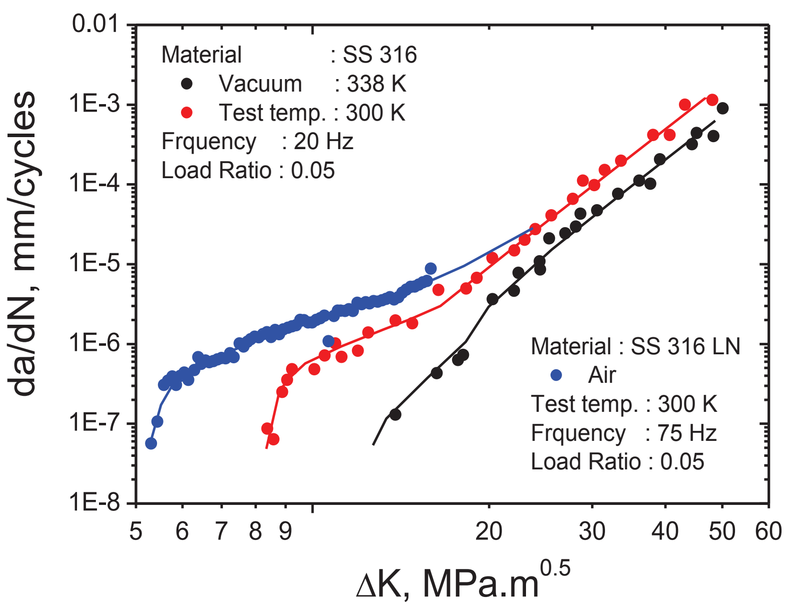

Figure 7.4 FCG results of SS316 in vacuum and air environment

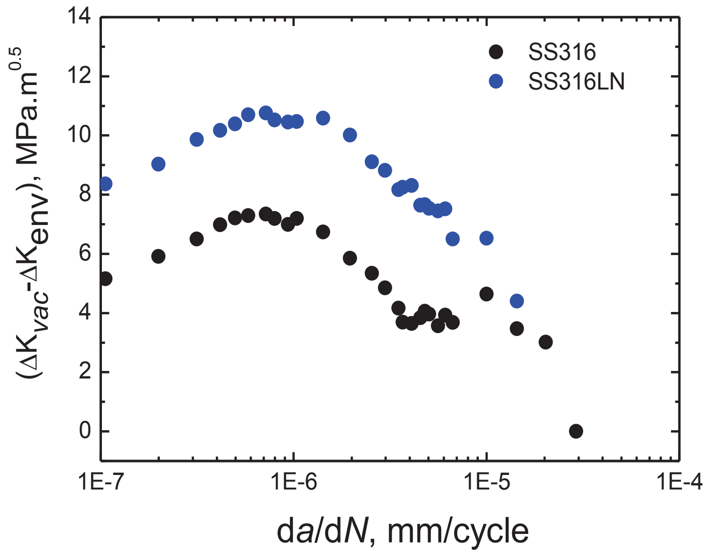

Figure 7.5 Environment contribution on FCG resistance of SS316LN. This includes any secondary contribution due to DIMT.

Figure 7.6 shows the comparison of the relative effects of environment on the FCG of SS304, SS316 and SS316LN materials. The decrease in the crack tip driving force with increase in the crack growth is quite significant for SS316LN when compared to SS304. It indicates that the alloy chemistry also plays an important role in the environmental contribution to the crack growth resistance. This could be in addition to any differences in contributions from the DIMT in the two steels. However, it can be noted that the difference in tensile properties of these materials are not much. From the above discussion, it is obvious that the environment plays a vital role on the long crack growth behaviour.

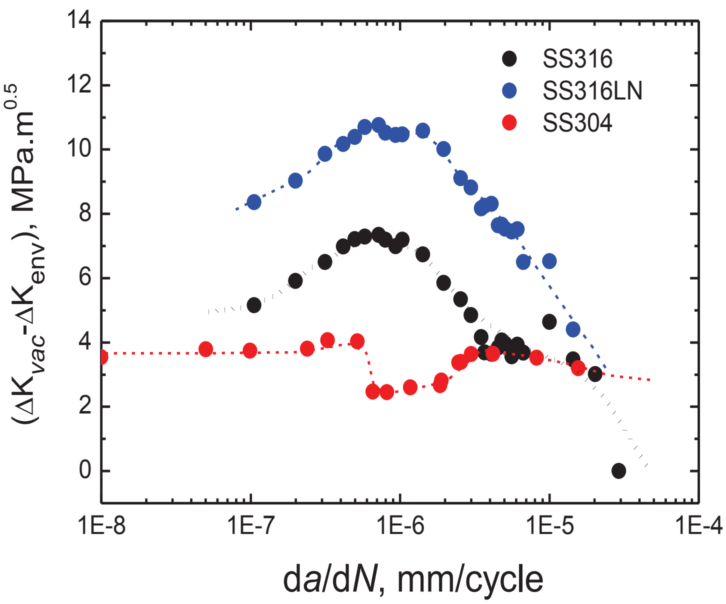

Figure 7.6 Comparison of the effects of environment on the crack growth resistance for SS304, SS316 and SS316LN

7.3 Short and Long fatigue crack growth measurement in vacuum chamber of SEM

The short and long crack growth behaviour of nitrogen alloyed austenitic stainless steel is studied in vacuum using in-situ measurements in Scanning Electron Microscope (SEM). Details about the experiments were presented in the Chapter 3. However, a brief summary of the experimental details is presented here. Both short and long crack growth of SS316LN under cyclic loading in vacuum has been evaluated in the Scanning Electron Microscope using small CT samples. The samples used for short crack growth study were 2 mm thick and 25 mm wide. Initial notch of depth 5mm and root radius 125 μm was made using EDM wire cutting. For the long crack growth study, 6mm thick sample was used. The present study focuses on the *insitu* deformation and damage development at the crack tip of SS316LN under cyclic loading. The short crack length was measured from the notch without pre-cracking. The notched CT specimen was loaded on to the mechanical stage as shown in Fig.3.10 in Chapter 3. The mechanical stage was loaded in the SEM chamber maintaining a constant vacuum of 10^{-7} mbar. The sample was cyclically loaded at a frequency 0.5 Hz to study the initiation of small crack from the notch and its subsequent growth during further cycling. For long crack growth study in vacuum, samples were loaded in to the SEM mechanical stage after fatigue pre-cracking to an initial crack length of ~ 1 to 1.5 mm in a servohydralic machine outside of the SEM. The fatigue crack propagation of both short and long cracks was monitored in situ on the SEM screen. Results were recorded using a video system and also with intermittent snap shots.

7.4 Fatigue crack growth analysis of short crack and long crack in vacuum

Figure 7.7 shows the crack length (a) data as a function of number of cycles (N) for both long and short cracks in SS 316L(N). The tests are done at constant load amplitude at an R value of 0.1. The peak load amplitude was 500 N for the short crack and 2500 N for long crack. Since the maximum crack growth monitored was only 0.3 mm, there was not much variation in ΔK or K_{max} during the test. The purpose was to assess the difference in the driving force between long and short cracks as a measure of that due to internal stresses generated in cycling before short cracks start growing. The corresponding crack growth rates as a function of the applied K_{max} are shown in Fig. 7.8. It clearly indicated the short cracks grow much faster than the long cracks, and the short crack growth thresholds in terms of the applied ΔK are below the long crack growth thresholds, even in vacuum. This trend is in agreement with the vast literature data in air [191]. Several studies [165-184] have attempted to address the question what contributes to the low applied *K* values required for short cracks in relation to that for long cracks to maintain the same crack growth rates, while on the basis of Griffiths or Orowan equation, the short cracks need higher stress to sustain their growth. A well-accepted cause of this difference appears to be the lack of crack closure for short crack when compared to the long cracks suggested by Suresh [168]. Consequently, they invoked the breakdown of the similitude concept to account for the anomalous short crack growth behaviour.

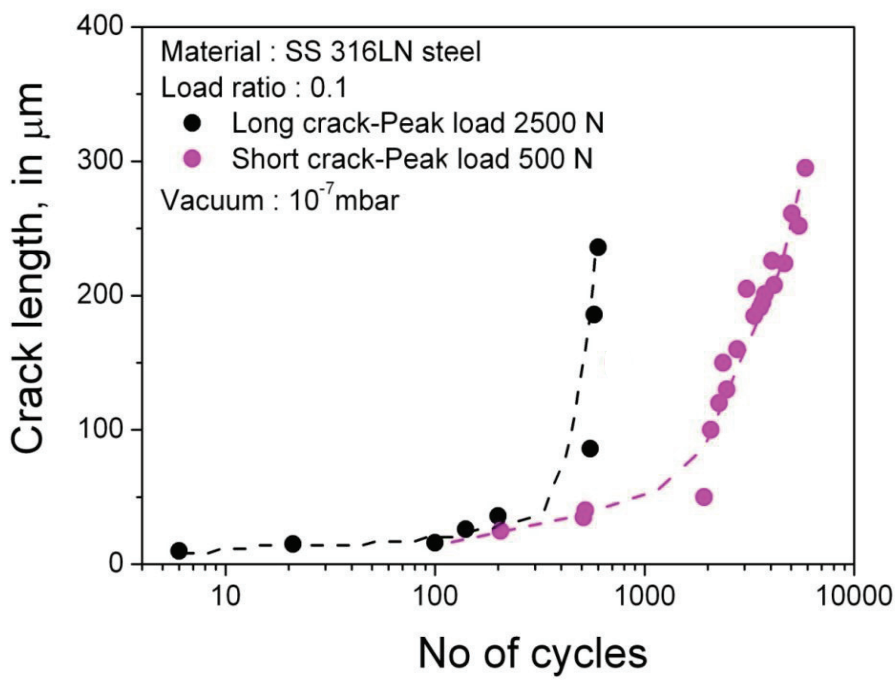

Figure 7.7 Crack growth as a function of number of cycles for short and long cracks in vacuum.

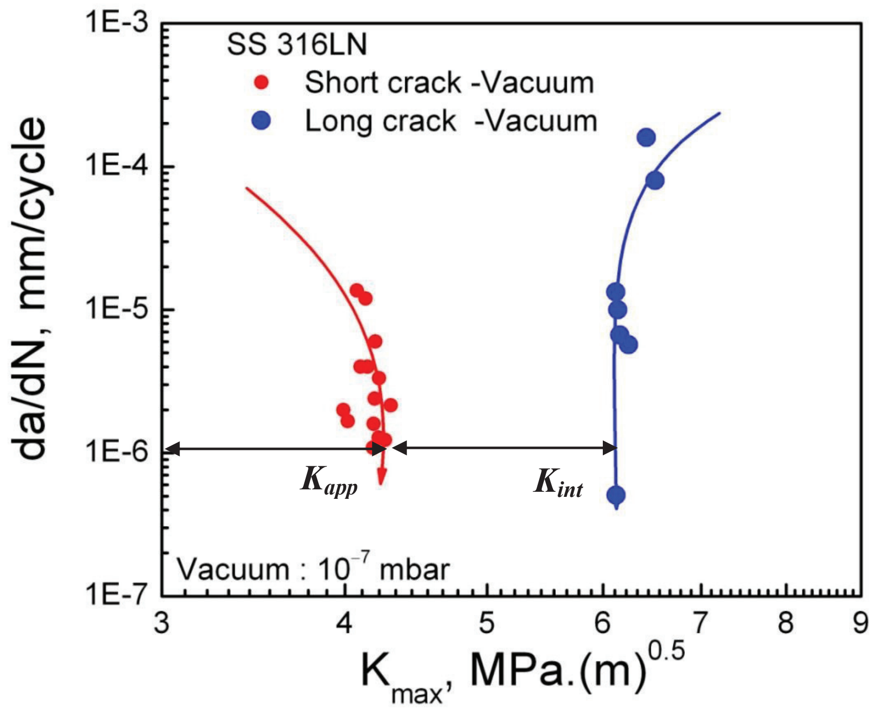

Figure 7.8 Crack growth rate as a K_{max} for the long and short crack in vacuum

It may be recalled that the thickness of specimens used for short crack and long crack studies were different; 2 mm for the former and 6 mm for the latter . Also, the crack tip root radii may influence the crack growth rates. It is required to discount these effects before going to further analysis of the data.

Fatigue crack growth rate data are not always geometry-independent in the strict sense since thickness effects sometimes occur. However, literature data on the influence of thickness on fatigue crack growth rate are mixed. Fatigue crack growth rates over a wide range of ΔK have been reported to either increase, decrease, or remain unaffected as specimen thickness is increased. Thickness effects can also interact with other variables such as environment and heat treatment. For example, materials may exhibit thickness effects over the terminal range of da/dN versus ΔK, which are associated with either nominal yielding or as K_{max} approaches the material fracture toughness. The potential influence of specimen thickness should be considered when generating data for research or design. To avoid nominal yielding, the ASTM recommendation (E 647, A1.2.2.1) is that for C(T) specimens thickness be within the range $W/20 \leq B \leq W/4$. In the present study on specimens with 25 mm width, the permitted thickness range is 1.25 - 6.25 mm. Also, in the present study, neither the K_{max} is approaching material fracture toughness.

Sadananda and Sarkar [234 of Fig 16] have estimated the K for short crack emanating from elastic-plastic stress field of holes of different radii. They have shown that the normalized K ahead of a crack for a given x/ρ (x is the distance from crack tip and ρ is the hole radius) increases with increasing hole size, radii 0.5 mm to 4 mm. For the lowest value of ρ in this study, i.e., 0.5 mm, the maximum in the normalized K is 1.5. In the present work, the short crack studies are with $\rho < 0.2$ mm. Long crack studies with fatigue pre-cracked specimen, the crack tip blunting leads to $\rho \sim 0.05$ mm. The difference in the stress profile at peak loading, i.e., K_{max}, may not be significantly different.

The growth behaviours of short cracks and long cracks are analysed using the unified approach based on the following concepts.

1. The unambiguous description of fatigue behaviour requires two load-parameters; the amplitude ΔK, and the peak K_{max} of the stress intensity factor.

2. The similitude concept, which states that the equal crack growth driving forces cause equal crack growth rates, is valid for all crack lengths.

3. Based on the Griffith's or Orowan's theory, the small cracks require high stresses to sustain their growth. [22].

4. Hence, internal stresses generated by fatigue cycling are involved in sustaining the growth of short cracks. These augment the applied stresses. Fig. 7.7 clearly shows that more number of fatigue cycles are involved during the growth of short cracks. (Notice the logarithmic scale on the X-axis). They help in generating the required internal stresses to sustain the growth of short cracks.

Figure 7.8 indicates that the short crack growth is faster than the long crack when crack growth rate is presented in terms of only the applied K_{max} or ΔK, which by itself does not include the internal stresses that are involved. The total crack tip driving force that is involved, K_{tot}, can be written as.

$$K_{tot.} = K_{app.} + K_{int.}$$

$$K_{tot.} - K_{app.} = K_{int}$$

Where $K_{tot,}$ K_{app} and K_{int} are total, applied, and internal stress intensity factors, respectively. The internal stresses can be positive or negative. The compressive or tensile overloads can, for example, induce tensile (positive) or compressive (negative) internal stresses that aid or obstruct the crack-tip driving forces. Residual stresses are only a sub-set of internal stresses.

It is important to recognize that the internal stresses are very difficult to compute or estimate except for simple cases like dislocation pile-ups or their distributions. Nevertheless, their presence and their contribution cannot be ignored. Incipient crack formation (short cracks) in a smooth specimen occurs only by the build-up of in situ generated local stress concentrations, which are sources of internal stresses. Here, the involved internal stresses are estimated using the long crack growth rate data as the reference [191], by invoking the principle of similitude that equal crack tip driving forces give equal crack growth rates as follows.

General representation of *K* for remotely applied load on the cracked body is

$K=\sigma\sqrt{\pi * a}$-----------(2)

The equation (2) is applicable for long and short cracks

$K_{LC} = \sigma\sqrt{\pi * a_{LC}}$------Long Crack (LC) ---------(3)

$K_{SC} = \sigma\sqrt{\pi * a_{SC}}$------ Short Crack (SC) ---------(4)

From (3) and (4), employing similitude concept.

$\Rightarrow K_{int} = K_{LC} - K_{SC}$-----(5)

$K_{int} = \sigma_{int}\sqrt{\pi * (a_{LC} - a_{SC})}$,

where the σ_{int} is the effective contribution of the internal stress to the remotely applied stress using the basis of similitude concept. Thus, the internal stresses are plotted as function of $\sqrt{a}$ in order to follow general trend. The internal stresses will be become nullified when short crack growth rate is merging with long crack growth rate from the Fig 7.8. The internal stress results presented in Figure 7.9 show that the computed internal stresses vary with the crack length. Their contribution decreases as the short cracks grow and move away from the stress concentrations.

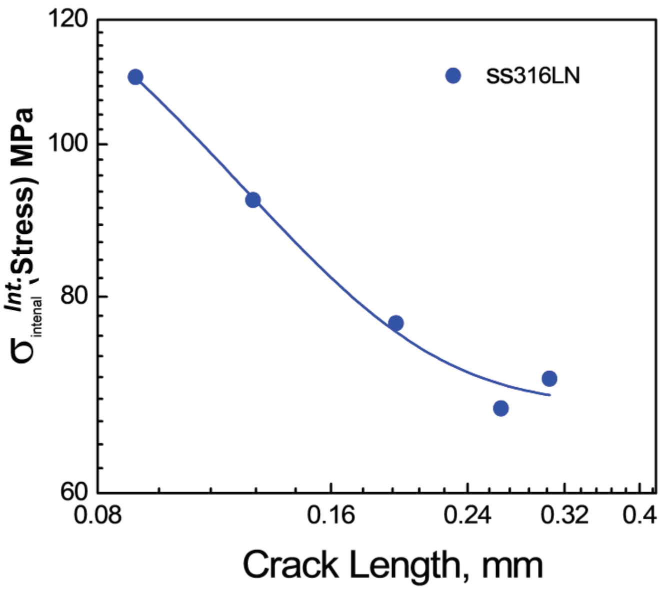

Figure 7.9 The variation in the internal stress profile as a function of crack length

Figure 7.10 shows the modified K-T diagram constructed by extending the applied stress σ vs crack length (a) line corresponding to ΔK_{th} to the short crack regime. In the original K-T diagram the threshold-line is bent to meet the endurance limit of a smooth specimen. On the other hand, the unified approach states that the internal stresses help the applied stresses for the short crack to grow and become long crack. Unified Approach considers [234] that the long crack thresholds ($K_{max,th}$ and ΔK_{th}) are fundamental material properties for a given material and environment, and they are independent of crack length and specimen geometry. Hence for cracks to initiate and grow at endurance limit stress for a smooth specimen, localized internal stresses must be generated by fatigue damage in terms of dislocation stress-fields. These internal stresses would aid in moving the local stress value from A to B (Fig. 7.10) in order to meet that corresponding to the ΔK_{th}-line where the incipient crack can initiate and grow. For its continuous growth, the gradient of the internal stresses must meet the minimum stress gradient as given by the $K_{max,th}$ or ΔK_{th}-line. Hence at the endurance limit, the local stress must increase from point A to B and the minimum gradient must be along the path B to C. In a way, the local internal stress magnitude and its gradient must follow the internal stress triangle indicated in the modified K-T diagram, Fig. 7.10, for a short crack to get initiated and grow. This also applies for a Griffith-crack to get initiated and grow.

The modified K-T diagram developed based on the unified principle can also capture the influence of environment. The line ED corresponds to the environment threshold. In the case of FCG in environment also, the threshold line will bend towards the endurance limit (The difference, if any, between the endurance limits in environment and vacuum is also due to the chemical driving forces.) Further internal stresses are required for the crack initiation in the AB line as can be seen in Fig.7.10. Once, the internal stresses build up to meet point B, crack nucleation starts and the stress gradient to drive further growth of the crack follows the line BC. Thus, the ADE represents the internal stress triangle, which is smaller than the ABC, which is for vacuum. The reduced triangle area can be seen in Fig.7.10 for air environment, which indicates the impact of environment on the threshold line. The difference between the two correspond to the mechanical equivalent of the chemical forces. Thus, the modified K-T diagram captures the intrinsic resistance of the material to FCG. Hence, it is a powerful tool in design to account for subcritical crack growth including for short cracks and in environments and in fracture analysis.

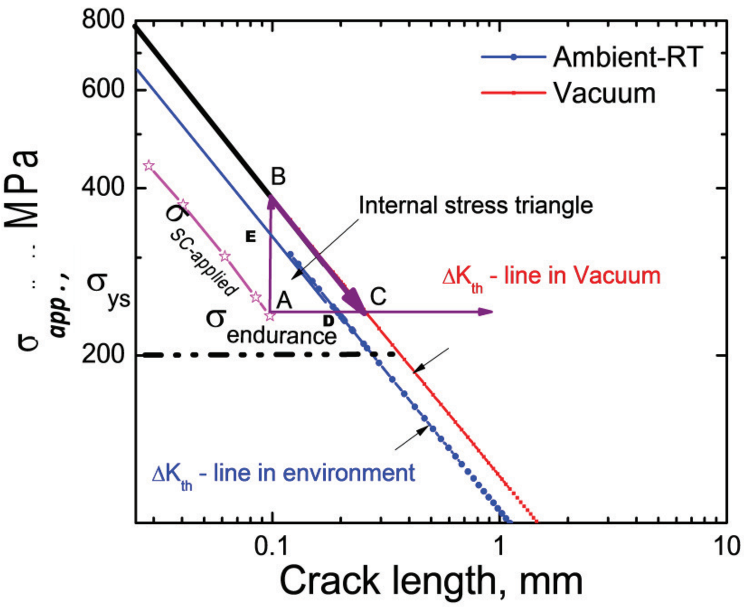

Figure 7.10 Modified Kitagawa-Takahashi diagram connects the short and long crack growth behaviour and the behavior of a smooth specimen.

7.5 Short crack initiation mechanism

Figure 7.11 (a) shows the initial notch made by EDM wire cut, from which the crack initiates under cyclic loading. During the first few cycles, slip gets activated near the notch and spreads around the tip. Further increase in the number of cycles leads to the generation of more number of slip bands and which impinge on the grain boundaries. Precipitates/inclusions or grain boundary triple points are the preferred sites for the short cracks to nucleate. In the present case, the preferred crack growth appears to be along low index slip planes such as (111) and [110] directions which are the most favorable in this material. In some locations in the interior of grains, the crack path appears to be more tortuous. Ahead of the crack tip, the martensite traces were found [Fig 7.12]. This deformation induced martensite could be the possible mechanism for creating tortuous short crack growth in these grains in addition to the preferred slip planes. Since the regime where the martensite forms, local enhancement of crack growth resistance leads to crack path deviation. The long crack growth also follow the same crystallographic planes as in the case of short cracks, however the slip density appears to be more at the tip of long crack. The crack path changes due to the orientation of the neighboring grains. These observations are in agreement with the previous reports for stainless steels [44, 236].

The data on applied stress for short crack also are included in Fig.7.10. These data fall within the internal stress triangle. Specifically, it is to be noted that it is not below the endurance limit, σ_{end}. If the applied stresses were lower than σ_{end}, adequate local stresses for crack growth will not be generated by cyclic plasticity. For applied stresses more than or equal to σ_{end}, the internal stresses developed by local plasticity augments the applied stresses to achieve stress levels required for crack growth. Accumulated cyclic strain contributes a cumulative damage that enhances the local internal stress, eventually meeting the minimum threshold criteria for its growth.

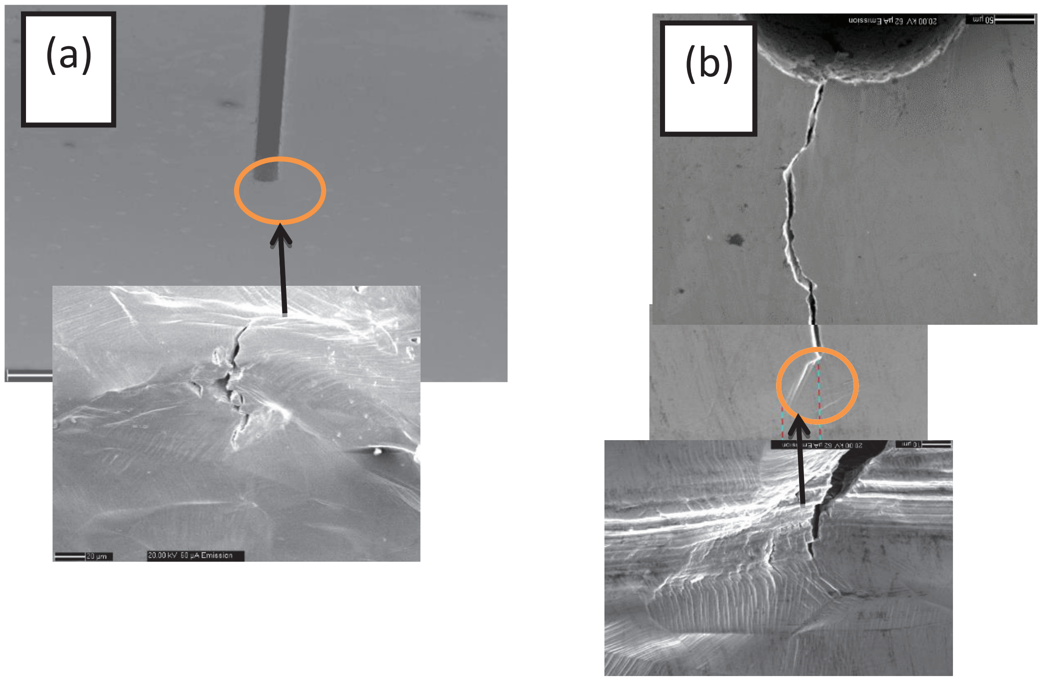

Figure 7.11 (a) Short crack nucleation & growth (b) Long crack growth after pre-cracking

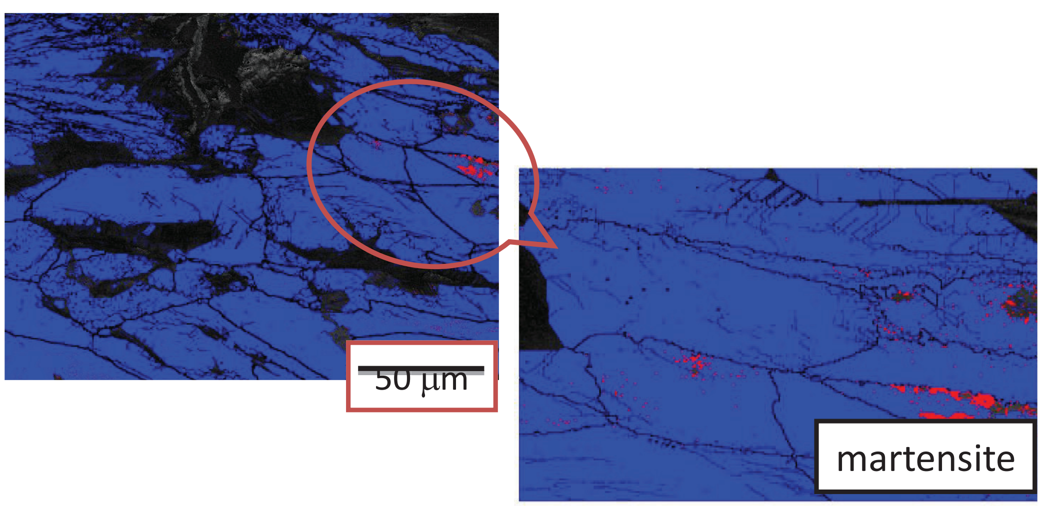

Figure 7.12 Formation of deformation-induced martensite ahead of short crack as marked

7.6 Conclusions

The differnce between the growth behaviours of long cracks and short cracks have often been attributed to environmental effects in this chapter, the long crack growth behaviour of austenitic stainless steels in air environment and vacuum are analysed and the impact of environment on the crack growth resistance has been examined. In addition, the short and long crack growth behaviour of SS316LN -8N in vacuum is analyzed using the fundamental concepts and applying the well-known Kitagawa-Takahashi diagram, which was suitably modified. The modified K-T diagram can account for the existence of in-situ generated internal stresses that augment applied stresses. The diagram defines the magnitude of the minimum internal stresses and their gradients needed for the initiation and growth of cracks under fatigue loading. It also unifies the growth of long and short cracks. From the point of the Unified Approach, the short cracks are not different from the long cracks, and the fatigue thresholds are independent of crack length. Most importantly, no similitude breakdown needs to be invoked to account for the apparent anomalous behaviour of short cracks, if internal stresses generated by the fatigue damage is included in addition to the applied stresses for computing the driving forces.

CHAPTER 8

SUMMARY AND SCOPE FOR FUTURE WORK

CHAPTER 8: SUMMARY AND SCOPE FOR FUTURE WORK

8.1 Summary

The summary of the work carried out on the "Fatigue Crack Growth Behaviour of Nitrogen Bearing Austenitic Stainless Steel and its Weld : Analysis using Unified Approach". The fatigue crack growth behavior SS316LN steel has been evaluated in both the Paris and threshold regimes for the temperature range 300 - 823 K. The crack growth behaviour after crack closure correction compared with the constant K_{max} test data at room temperature indicated the discrepancy in the crack closure theory. The improved FCG resistance in the intermediate temperatures is attributed to the dynamic strain ageing effects rather than the crack closure. Attempts to correlate the FCG data with normalized (using modulus and yield stress) driving forces, showed that the temperature dependence of modulus and yield stress can not completely account for the temperature dependence of FCG resistance. Moreover, an increase in crack growth thresholds was observed at high temperature 823 K, when compared to those obtained in the temperature range 623 - 723 K. The plateau (623-773 K) or increase (773-823 K) in the threshold with temperature and overlapping of FCG curves in the Paris regime at 673-773 K is due to DSA, which exerts beneficial influence on the intrinsic FCG resistance. Two activation energy values for DSA were estimated; (a) 90± 2 kJ/mol (623-723 K) which is corresponding to the activation energy for the carbon diffusion, and (b) 160±5 kJ/mol for nitrogen diffusion, indicating that the interaction of these interstitial solute elements with moving dislocations is responsible for the DSA in different temperature ranges in this steel. The reason for much larger increase of threshold at

823 K could not be unequivocally established, though the possibilities are DSA associated with substitutional solutes, crack tip blunting due to creep or oxidation effects leading to reduced local stress intensities rather than the crack closure effects.

The FCG crack growth analysis were carried out using the unified apparoch in order to complete description of the FCG behaviour. The effect of nitrogen concentration on the fatigue crack growth resistance of SS316L(N) at ambient conditions (laboratory air) was evaluated. The results indicate that a) the effect of nitrogen depends on the concentration, b) there is an optimum concentration where the resistance to the fatigue crack growth is maximum, and c) the enhanced resistance to crack growth can be attributed to the localized transformation toughening due to deformation induced martensite, in addition to the effects of N on the SFE and solid solution strengthening. The lower FCG resistance of 22N steel is due to limited DIMT at the crack tip.

The influence of load ratio *R* on the fatigue crack growth behaviour was assessed for the three nitrogen variants selected in this study. The results were analyzed using the unified approach involving ΔK and K_{max} parameters. Crack growth trajectory maps were constructed and compared with those determined using the literature data, where the transformation toughening has been adequately established. The results indicate the similarity in the crack growth trajectories for all the three variants, establishing that the increased crack growth resistance in the current nitrogenized alloys is due to transformation toughening. It is shown that the microstructural analysis on these three nitrogen alloys are consistent with the published data indicating that deformation induced martensitic transformation is occurring ahead of the crack tip contributing to the enhanced toughening. The extent of this transformation decreases with increase in nitrogen content. *The results from the present study indicate that the optimum nitrogen content to derive the maximum benefit should also consider,for relevant applications, its effect on the deformation induced martensite formation, in addition to the other well-known effects of N such as solid solution strengthening, reduced stacking fault energy, grain refinement and enhanced strain hardening.*

FCG behavior of SS316(N) weld metal has been evaluated at different load ratios at room temperature and is analyzed using the Unified Approach. It is found that the FCG thresholds are much higher for the weld metal than the base metal, and the FCG rates are lower, particularly at low R values. This enhanced resistance to crack growth arises from a) residual compressive stresses, b) stress-induced martensitic transformation of austenite phase present near the crack tip region c) the higher alloy content and d) the presence of δ-ferrite. Crack growth trajectory map was developed and compared with the previously determined trajectory map of the base metal. The crack growth trajectories of both the base and the weld metals deviated towards the K_{max}-axis from the pure-fatigue line. In the case of the base metal, the deviation was related to the stress-induced martensitic transformation of the retained austenite ahead of the crack tip. The trajectory map of the weld metal deviated more than that of the base metal. The larger deviation is attributed to the residual compressive stresses introduced during welding in addition to the presence of any transformation toughening. In this context, published crack growth data for other weld and base metals available in the literature are also analyzed using the

Unified Approach. It was found that the presented results are consistent with those published in the literature. The results also indicate that the residual stresses can vary with the welding process, thickness of the weld, and the subsequent post-welding stress relief operations. Similar analysis of the FCG data for the cold worked material shows that the K_{max}-dependent phenomenon/phenomena is marginally enhanced in the cold worked material compared to the solution annealed material, in spite of the increase in the extent of DIMT. Further studies are required to estimate the residual stresses in cold worked material to ascertain if the beneficial effects of DIMT are partially offset by the presence of residual stresses.

The long crack growth behaviour of austenitic stainless steels in air environment and vacuum are analysed and the impact of environment on the crack growth resistance has been examined. The crack growth resistance improved in vacuum and a possible secondary contribution that stems from the toughening due to the deformation induced martensite transformation cannot be ruled out. In addition, the short and long crack growth behaviour is analyzed using the fundamental concepts and applying the well-known Kitagawa-Takahashi diagram, which was suitably modified, particularly for the nitrogen alloyed stainless steel, tested in vacuum. The modified KT diagram can account for the existence of in-situ generated internal stresses that augment applied stresses. The diagram defines the magnitude of the minimum internal stresses and their gradients needed for the initiation and growth of cracks under fatigue loading. It also unifies the growth of long and short cracks. Based on this study, it can be pointed out that the Unified Approach states that the short cracks are not different from the long cracks. Most importantly no similitude breakdown needs to be invoked to account for the apparent anomalous behavior of short cracks. For short crack growth internal stresses generated by the fatigue damage has to be included in addition to the applied stresses. In addition, the short crack nucleation has been examined by Insitu SEM examination reveals that the crack nucleation is predominantly associated with MnS inclusions rather than the triple boundaries or grain boundaries in the present case. The formation of deformation induced matensite is confirmed with the *in situ* SEM-EBSD.

8.2 Future Work

In chapter 4, the reason for a large increase in threshold ΔK at 823 K could not be established; it could be either DSA associated with substitutional solutes, or crack tip blunting (due to creep/oxidation) leading to reduced local stress intensities. The loading frequency influences the creep/oxidation effects as well as DSA through the crack tip strain rate. Extensive FCG testing and data analysis are required at high temperature for a better understanding of the DSA effects. Further studies at temperatures above 823 K to examine the onset and disappearance of DSA effects would help understand these better. In chapter 5, the benefit of DIMT could not be quantitatively distinguished from the other advantages of presence of N, such as grain refinement and enhanced strain hardening. Additional controlled experiments in conditions outside the regime of DIMT, e.g., at higher temperatures on steels with different nitrogen contents, would throw more light on this. The influence of residual stresses generated in the materials during the manufacturing such as welding and cold work due to bending etc on the crack growth behaviour at different temperatures requires further studies. Estimates of the residual stresses in cold worked material and FCG tests at different conditions will throw more light on the relative contributions of DIMT and the presence of residual stresses. Modelling of the DIMT using artificial neural network will be useful in identifying the role of the alloying elements and also for the effect of stress/plastic strain in this phenomenon.

CHAPTER 8

SUMMARY AND SCOPE FOR FUTURE WORK

CHAPTER 8: SUMMARY AND SCOPE FOR FUTURE WORK

8.1 Summary

The summary of the work carried out on the "Fatigue Crack Growth Behaviour of Nitrogen Bearing Austenitic Stainless Steel and its Weld : Analysis using Unified Approach". The fatigue crack growth behavior SS316LN steel has been evaluated in both the Paris and threshold regimes for the temperature range 300 - 823 K. The crack growth behaviour after crack closure correction compared with the constant K_{max} test data at room temperature indicated the discrepancy in the crack closure theory. The improved FCG resistance in the intermediate temperatures is attributed to the dynamic strain ageing effects rather than the crack closure. Attempts to correlate the FCG data with normalized (using modulus and yield stress) driving forces, showed that the temperature dependence of modulus and yield stress can not completely account for the temperature dependence of FCG resistance. Moreover, an increase in crack growth thresholds was observed at high temperature 823 K, when compared to those obtained in the temperature range 623 - 723 K. The plateau (623-773 K) or increase (773-823 K) in the threshold with temperature and overlapping of FCG curves in the Paris regime at 673-773 K is due to DSA, which exerts beneficial influence on the intrinsic FCG resistance. Two activation energy values for DSA were estimated; (a) 90± 2 kJ/mol (623-723 K) which is corresponding to the activation energy for the carbon diffusion, and (b) 160±5 kJ/mol for nitrogen diffusion, indicating that the interaction of these interstitial solute elements with moving dislocations is responsible for the DSA in different temperature ranges in this steel. The reason for much larger increase of threshold at

823 K could not be unequivocally established, though the possibilities are DSA associated with substitutional solutes, crack tip blunting due to creep or oxidation effects leading to reduced local stress intensities rather than the crack closure effects.

The FCG crack growth analysis were carried out using the unified apparoch in order to complete description of the FCG behaviour. The effect of nitrogen concentration on the fatigue crack growth resistance of SS316L(N) at ambient conditions (laboratory air) was evaluated. The results indicate that a) the effect of nitrogen depends on the concentration, b) there is an optimum concentration where the resistance to the fatigue crack growth is maximum, and c) the enhanced resistance to crack growth can be attributed to the localized transformation toughening due to deformation induced martensite, in addition to the effects of N on the SFE and solid solution strengthening. The lower FCG resistance of 22N steel is due to limited DIMT at the crack tip.

The influence of load ratio R on the fatigue crack growth behaviour was assessed for the three nitrogen variants selected in this study. The results were analyzed using the unified approach involving ΔK and K_{max} parameters. Crack growth trajectory maps were constructed and compared with those determined using the literature data, where the transformation toughening has been adequately established. The results indicate the similarity in the crack growth trajectories for all the three variants, establishing that the increased crack growth resistance in the current nitrogenized alloys is due to transformation toughening. It is shown that the microstructural analysis on these three nitrogen alloys are consistent with the published data indicating that deformation induced martensitic transformation is occurring ahead of the crack tip contributing to the enhanced toughening. The extent of this transformation decreases with increase in nitrogen content. *The results from the present study indicate that the optimum nitrogen content to derive the maximum benefit should also consider,for relevant applications, its effect on the deformation induced martensite formation, in addition to the other well-known effects of N such as solid solution strengthening, reduced stacking fault energy, grain refinement and enhanced strain hardening.*

FCG behavior of SS316(N) weld metal has been evaluated at different load ratios at room temperature and is analyzed using the Unified Approach. It is found that the FCG thresholds are much higher for the weld metal than the base metal, and the FCG rates are lower, particularly at low R values. This enhanced resistance to crack growth arises from a) residual compressive stresses, b) stress-induced martensitic transformation of austenite phase present near the crack tip region c) the higher alloy content and d) the presence of δ-ferrite. Crack growth trajectory map was developed and compared with the previously determined trajectory map of the base metal. The crack growth trajectories of both the base and the weld metals deviated towards the K_{max}-axis from the pure-fatigue line. In the case of the base metal, the deviation was related to the stress-induced martensitic transformation of the retained austenite ahead of the crack tip. The trajectory map of the weld metal deviated more than that of the base metal. The larger deviation is attributed to the residual compressive stresses introduced during welding in addition to the presence of any transformation toughening. In this context, published crack growth data for other weld and base metals available in the literature are also analyzed using the

Unified Approach. It was found that the presented results are consistent with those published in the literature. The results also indicate that the residual stresses can vary with the welding process, thickness of the weld, and the subsequent post-welding stress relief operations. Similar analysis of the FCG data for the cold worked material shows that the K_{max}-dependent phenomenon/phenomena is marginally enhanced in the cold worked material compared to the solution annealed material, in spite of the increase in the extent of DIMT. Further studies are required to estimate the residual stresses in cold worked material to ascertain if the beneficial effects of DIMT are partially offset by the presence of residual stresses.

The long crack growth behaviour of austenitic stainless steels in air environment and vacuum are analysed and the impact of environment on the crack growth resistance has been examined. The crack growth resistance improved in vacuum and a possible secondary contribution that stems from the toughening due to the deformation induced martensite transformation cannot be ruled out. In addition, the short and long crack growth behaviour is analyzed using the fundamental concepts and applying the well-known Kitagawa-Takahashi diagram, which was suitably modified, particularly for the nitrogen alloyed stainless steel, tested in vacuum. The modified KT diagram can account for the existence of in-situ generated internal stresses that augment applied stresses. The diagram defines the magnitude of the minimum internal stresses and their gradients needed for the initiation and growth of cracks under fatigue loading. It also unifies the growth of long and short cracks. Based on this study, it can be pointed out that the Unified Approach states that the short cracks are not different from the long cracks. Most importantly no similitude breakdown needs to be invoked to account for the apparent anomalous behavior of short cracks. For short crack growth internal stresses generated by the fatigue damage has to be included in addition to the applied stresses. In addition, the short crack nucleation has been examined by Insitu SEM examination reveals that the crack nucleation is predominantly associated with MnS inclusions rather than the triple boundaries or grain boundaries in the present case. The formation of deformation induced matensite is confirmed with the *in situ* SEM-EBSD.

8.2 Future Work

In chapter 4, the reason for a large increase in threshold ΔK at 823 K could not be established; it could be either DSA associated with substitutional solutes, or crack tip blunting (due to creep/oxidation) leading to reduced local stress intensities. The loading frequency influences the creep/oxidation effects as well as DSA through the crack tip strain rate. Extensive FCG testing and data analysis are required at high temperature for a better understanding of the DSA effects. Further studies at temperatures above 823 K to examine the onset and disappearance of DSA effects would help understand these better. In chapter 5, the benefit of DIMT could not be quantitatively distinguished from the other advantages of presence of N, such as grain refinement and enhanced strain hardening. Additional controlled experiments in conditions outside the regime of DIMT, e.g., at higher temperatures on steels with different nitrogen contents, would throw more light on this. The influence of residual stresses generated in the materials during the manufacturing such as welding and cold work due to bending etc on the crack growth behaviour at different temperatures requires further studies. Estimates of the residual stresses in cold worked material and FCG tests at different conditions will throw more light on the relative contributions of DIMT and the presence of residual stresses. Modelling of the DIMT using artificial neural network will be useful in identifying the role of the alloying elements and also for the effect of stress/plastic strain in this phenomenon.

SUMMARY

Fatigue crack growth (FCG) properties of SS 316L(N), a major structural material for nuclear, chemical, automobile and cryogenic industries are required for damage tolerant design and integrity assessment of components subjected to cyclic loading during service. Extensive studies in literature show that these properties are influenced by test conditions (such as temperature, load ratio, frequency, environment etc) and material conditions (such as cold work and residual stresses in forming and welding, and ageing in service). Also, it is observed that growth of short cracks cannot be predicted using data obtained from long cracks. ***There are two fundamental issues yet to be resolved (1) effect of load ratio on fatigue crack growth and (2) the reason for higher crack growth rate for short cracks when compared to long crack. Attempts have been made in this thesis to address these two fundamental issues through characterizing the FCG behaviour of SS316LN base, weld and cold worked material.*** In the process, effect of nitrogen content, test temperature and frequency on the FCG behaviour has been examined.

FCG behavior of SS316L as a function of nitrogen has been evaluated incorporating the crack closure effects at ambient and elevated temperatures. The results obtained from constant K_{max} test, i.e., in closure free condition differ from those incorporating the crack closure effects. The improved FCG resistance in the intermediate temperatures manifested as a plateau or increase in the effective threshold with temperature and overlapping of FCG curves in the range 623 - 773 K is attributed to dynamic strain ageing (DSA). The activation energy values 90± 2 kJ/mol (623-723 K) which is corresponding to the activation energy for the carbon diffusion, and 160±5 kJ/mol (773-823 K) for nitrogen diffusion determined from the temperature-dependence of FCG properties indicate that the diffusion of interstitial solute elements is responsible for the DSA. The dormancy of crack at low frequency and at high temperature is associated with blunting of crack tip due to creep and/or oxidation and not because of crack closure.

Further analyses were carried out using the Unified Approach to provide a physically more meaningful and self-consistent approach to address a) the load ratio effects, b) the short crack problem and c) role of residual stresses due to welding and cold working. The role of nitrogen in FCG behaviour has been examined considering three concentrations in this study. FCG rates as a function of R-ratio were determined. The results were analyzed using the two-parametric approach involving ΔK and K_{max} parameters. Crack growth trajectory maps were constructed, and the effect of nitrogen on the crack growth trajectory has been established in this study. It is shown that deformation-induced martensitic transformation (DIMT) is the K_{max} dependent process that mainly causes the deviation of the crack growth trajectory from the pure fatigue line (45^{o} line). The increased crack growth resistance in these alloys is due to transformation toughening. The presence of DIMT was confirmed by Magnetic Atomic Force Microscope (MAFM). The contribution from the compressive residual stresses in welds is demonstrated to be more dominant at low R-values than at high R-values. It is shown that the Unified Approach provides a self-consistent analysis of the role of residual stresses introduced during welding. The results of cold worked material show that the increase in the cold work improved the FCG resistance though deformation induced martensite transformation up to 10 % cold work, beyond which there is no further improvement.

On the basis of Griffith's equation or Orowan equation, the shorter the crack, the higher are the stresses needed for its growth. The short crack growth data in literature, however, appears to grow at smaller ΔK than that found for long cracks. Hence, similitude break down was proposed for short cracks. Extensive literature on fatigue damage analysis in the endurance limit indicate that the large numbers of cycles at these levels lead to formation of intrusions and extrusions, dislocation slip bands, dislocation pile-ups, and deformation bands which contribute to local internal stresses with stress-gradients. The incipient cracks form in the presence of these internal stresses which are augmented by the remote applied stresses. Fracture mechanics does not take these internal stresses explicitly into consideration in computing actual crack tip driving forces. Recognising this, a modified Kitagawa diagram was developed that connects the short crack growth behavior with that of long crack growth by considering these internal stresses. The Unified Approach provides a simple methodology to compute the required minimum internal stresses needed in addition to the applied stresses for the short cracks to grow. This approach is adopted to describe the differences in growth behaviour of short cracks and long cracks in SS316L(N) to show that there is no need to invoke similitude breakdown if one considers the total crack tip driving force that includes applied and internal stresses. The modified Kitagawa-Takahashi diagram was also used to evaluate the contribution of environment-induced chemical driving forces to the crack tip stress fields.

DECLARATION

I hereby declare that the investigation presented in the thesis has been carried out by me. The work is original and has not been submitted earlier as a whole or in part for a degree / diploma at this or any other Institution / University.

M. Nani Babu

(Matcha Nani Babu)